CHALMERS
UNIVERSITY OF TECHNOLOGY

Synthetic synchrotron diagnostics for runaways in tokamaks

Master's thesis in Physics and Astronomy

MATHIAS HOPPE

Department of Physics
CHALMERS UNIVERSITY OF TECHNOLOGY
Göteborg, Sweden 2017

Synthetic synchrotron diagnostics for runaways in tokamaks

MATHIAS HOPPE

CHALMERS
UNIVERSITY OF TECHNOLOGY

Department of Physics
Division of Subatomic and Plasma Physics
Plasma Theory
Chalmers University of Technology
Gothenburg, Sweden 2017

Synthetic synchrotron diagnostics for runaways in tokamaks
MATHIAS HOPPE

Supervisor: Ola Embréus, Department of Physics
Examiner: Tünde Fülöp, Department of Physics

Department of Physics
Division of Subatomic and Plasma Physics
Plasma Theory
Chalmers University of Technology
SE-412 96 Gothenburg
Telephone +46 31 772 1000

Cover: Synthetic synchrotron image from electrons initiated at twelve distinct radii.

Typeset in LaTeX
Gothenburg, Sweden 2017

Synthetic synchrotron diagnostics for runaways in tokamaks
MATHIAS HOPPE
Department of Physics
Chalmers University of Technology

Abstract

In tokamaks, highly relativistic electrons known as runaway electrons may be created, for example during disruptions when instabilities rapidly grow and cause operation to abruptly terminate. If control of the runaway beam is lost, the electrons can collide with the device wall and inflict severe damage. Therefore, it is of great importance to understand the processes that give rise to and govern the behaviour of these particles. One of the best ways to learn about the phase-space distribution of runaway electrons in experiments is to measure the synchrotron radiation emitted by them, often in the visible or infrared wavelength ranges, by making camera images or measuring the spectrum. Synchrotron radiation is emitted almost entirely in the forward direction of the electron, contrary to how light is usually emitted by most other light sources, and because of this electrons must be moving towards the observer in order to be seen. As a result, most electrons are invisible to the observer most of the time, and the synchrotron image does not reveal the full runaway beam, rather showing an abstract spot of light that can take on many different shapes. The sharp beaming in the forward direction of synchrotron radiation however puts an extra constraint on the image which allows the full velocity vector of the runaways to be inferred from the image.

In this thesis the numerical tool SOFT (for *Synchrotron-detecting Orbit Following Toolkit*), along with the theory on which it builds, is presented. With SOFT, synchrotron images from runaway populations that are arbitrarily distributed in phase-space can be simulated, taking various kinds of geometric effects (magnetic field geometry, camera placement, viewing direction etc.) into account. The effects on the image due to isolated variations in energy, pitch angle, minor radius and camera location are investigated and analysed. Synchrotron images simulated with analytical avalanche distributions of runaways are interpreted in relation to, and compared with, synchrotron images from mono-energetic runaway populations. All parameters are found to have distinct effects on the synchrotron spot, and it is shown that the synchrotron images due to full distributions of runaway electrons can partly be understood as dominated by particles of a particular energy and pitch angle.

Keywords: fusion, runaway, synchrotron, guiding-center, SOFT

Acknowledgements

First of all, I would like to direct my warmest gratitudes to my supervisor and personal doomsday prophet Ola, without whom this thesis would rest on a far less rigorous basis and be much more limited in scope. Aside from being the singly most important influence on my personal development as a physicist over the past one and a half years, his remarkable physical intuition has saved me from numerous pitfalls and ensured that there's never a shortage of interesting physics problems to delve into.

I would also like to thank Tünde for introducing me to the field of magnetic fusion, and for giving me the opportunity to work with my very own project on this fascinating topic. The selfless care and support she gives her students and co-workers is, mildly put, impressive, and serves as one of the best examples of how academic supervision should be conducted.

Special thanks to Adam for always being available to help with my queries into everything from runaway electrons and synchrotron radiation to administrative issues, and to István for guiding me from the very beginning on my path through the maze of difficult concepts and strange technical terms that is magnetic fusion. Thanks also to them, and to Geri, for taking the time to proof-read this thesis and give their comments on its contents.

I am also grateful to Alex and Bob for putting in much hard work in order to provide me with high quality data from Alcator C-Mod, which gives the results of this thesis a direct connection to reality and has allowed SOFT to be verified against experiment.

Last but not least, I would like to thank the members of the Chalmers Plasma Theory group for creating a warm and welcoming work environment, making it a pleasure to work with plasma physics.

Mathias Hoppe, Gothenburg, May 2017

Contents

1
Introduction

One of the greatest challenges of our time is that posed by global warming, caused by the dramatically increased emission of greenhouse gases over the past century. The science on the subject is clear [1], and it is necessary to quickly transition towards renewable energy sources that are both free of greenhouse gases, long-term sustainable and economically viable. Currently, no such source of energy (that could be deployed on a large scale) exists [2], but much effort is put into developing suitable technologies. One of the most promising technologies under active development, matching all the aforementioned criteria, is that of controlled nuclear fusion [3, 4]. In its naturally occurring form, nuclear fusion has already been the singly most important source of energy to the Earth for billions of years, as it is by this mechanism that our Sun shines and provides the necessities for life. Recreating the conditions of the Sun here on Earth, with temperatures of several million kelvin and strong pressures, has proven extremely difficult, since the strong gravitational field confining the fusion fuel in the Sun is not available on Earth. Instead, alternative methods of confinement must be used, and of the currently investigated methods, magnetic confinement fusion is considered one of the most realistic options [5].

Magnetic confinement fusion is based on the behaviour of matter at the hundreds-of-millions kelvin temperatures necessary for fusion. At these high temperatures the matter is in the plasma state [4], typically called the "fourth state of matter", in addition to the solid, liquid and gaseous states. In the plasma state, electrons are no longer bound to the atomic nuclei, and so the plasma consists of free charged particles. Because of this, a plasma is susceptible to the influence of electric and magnetic fields, which for example allows it to be confined using a magnetic field. It also means that particles will rearrange in order to shield out any external electric fields, and plasmas are characterized by being able to shield out such fields over relatively short distances [6]. As an additional consequence of the charged particles moving freely, interactions between particles in a plasma are long-range and continuous, with the collective behaviour of the plasma being of greater importance than individual Coulomb interactions for the overall physics, unlike in other matter where particles typically interact through "hard" Coulomb collisions.

There are many ways to magnetically confine a plasma, but as a consequence of the so-called "Hairy-ball theorem" [7], the only magnetic field configuration able to avoid significant losses is the toroidal configuration. By placing magnetic field coils around the torus and running a current through them, a magnetic field directed everywhere in the toroidal direction (see Fig. 1.1) will appear. A charged particle moving through this magnetic field will be constrained by the Lorentz force to move along the magnetic field lines, but due to the curvature of the magnetic field the

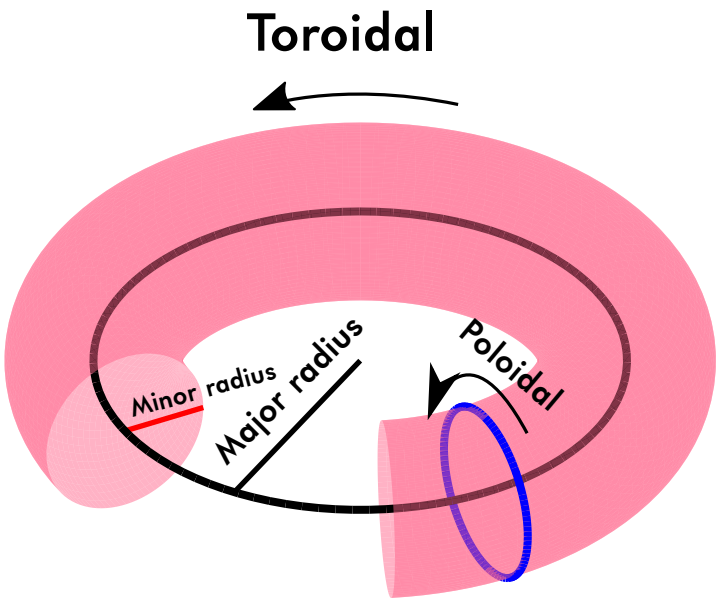

Figure 1.1: An illustration of toroidal coordinates, which are essential when working with tokamaks. Any point in a toroidal coordinate system is defined by the (fixed) major radius of its surrounding torus, as well as the minor radius, poloidal angle and toroidal angle.

particle will successively drift outwards, eventually hitting the wall. To prevent this, a magnetic field perpendicular to the toroidal magnetic field must be generated, directed in the poloidal direction (see Fig. 1.1). There are various ways to do this, but in the *tokamak* [8], the most common and successful type of toroidal magnetic confinement device investigated today, the poloidal magnetic field is generated by driving a current through the plasma itself. While this does give a magnetic field that successfully confines particles, it introduces a number of new problems which must be addressed.

A rather severe problem related to the toroidal current is the presence of so called *disruptions* [9]. During a disruption the temperature of the plasma rapidly drops, and the toroidal current decreases very quickly, which also induces a strong electric field in the machine that will accelerate charged particles. Here a peculiar feature of plasmas come into play, namely the fact that if a particle is fast enough the drag force acting on the particle will decrease the faster it moves, in sharp contrast to our everyday experience of how drag forces work*. A sufficiently fast particle will therefore be accelerated to even greater speeds, without experiencing any net decelerating force preventing it from reaching arbitrarily high speeds, thus giving rise to the phenomenon of *runaway particles*. Due to drifting of the particle orbits and an overall difficulty of controlling runaway beams, such particles are at great risk of causing severe damage to the device walls.

Of the various runaway species which may arise in a plasma [10–15], the runaway electrons are the most significant as their small mass allows them to appear in great

*Think for example of a bicyclist biking faster and faster, feeling a steadily increasing drag force due to air resistance, preventing her from reaching arbitrarily high speeds.

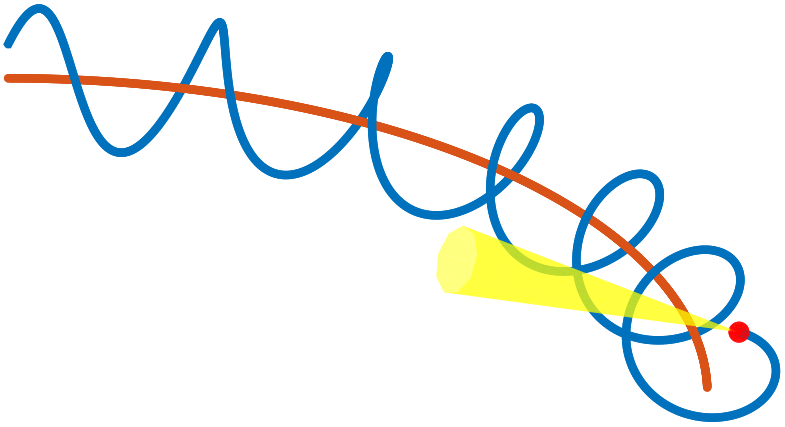

Figure 1.2: Runaway electrons emit synchrotron radiation, which is characterized by being emitted almost entirely in the particle's direction of motion.

numbers. In present devices, runaway electrons are mostly a nuisance, but in future, larger devices such as ITER [16, 17] they are expected to appear in much greater numbers due to the exponential scaling of the runaway population with plasma current [18], and thus be a severe threat to the device.

The main topic of this thesis is the radiation emitted by runaway electrons due to their gyro-motion around magnetic field lines, referred to as *synchrotron radiation*, which has been used as a means of experimentally studying runaways for nearly three decades [19]. As is well known from the theory of electric and magnetic fields, a charged particle in accelerated motion will emit electromagnetic radiation [20, 21], and when the particle in question is moving at speeds close to that of light (which runaway electrons do) the radiation becomes sharply peaked in the particle's direction of motion, as illustrated in Fig. 1.2. This beaming effect gives rise to counter-intuitive light spots being observed in tokamaks, that will be shown in the later parts of this thesis to reveal much about the particles generating it. In addition to synchrotron radiation, electrons will also emit a significant amount of so called *bremsstrahlung* [22], which is emitted as a consequence of the electron colliding with other particles [23]. While bremsstrahlung could in principle be treated using the methods developed in this thesis, such studies will be left out in favour of synchrotron radiation.

The beaming of synchrotron radiation in the forward direction also has the consequence that most of the runaway electrons are hidden from the observer most of the time, so that one can actually only see a small fraction of the runaway beam at any instant. While this may at first appear to be a great limitation, it instead turns out to be a great advantage of synchrotron radiation when diagnosing the plasma. If the runaway electrons would have emitted regular isotropic radiation, i.e. equally in all directions, one would be able to see the location of the runaway beam at all times at every toroidal location in the device, and by measuring the radiation intensity and spectrum one could estimate the energy of the constituent particles of the runaway beam. With synchrotron radiation however, which appears in much less intuitive shapes as we will see in this thesis, the energy can still be probed in the usual way, while the sharp forward peaking of the radiation in addition allows

us to determine their full velocity vector. Since the shape of the observed spot is strongly influenced by the particles' directions of motion, synchrotron radiation thus grants us the ability to probe the full phase-space distribution function of runaways, making synchrotron radiation a powerful tool in the study of runaway electrons.

The remainder of this thesis will treat the synchrotron radiation emitted by runaway electrons, and in particular the synchrotron images they give rise to. In Chapter 2, the underlying theory of particle and guiding-center motion, runaway electrons and their synchrotron radiation is explained. The theory is then used to motivate and introduce the numerical tool SOFT in Chapter 3, which simulates a synchrotron camera in a tokamak and utilizes a simplified model of synchrotron radiation which is also derived. Finally, in Chapter 4 the synchrotron images obtained from different runaway electron populations are analyzed and explained.

2

Runaways and their radiation

The main subject of this thesis is the synchrotron radiation emitted by runaway electrons found in tokamak plasmas, which is used to experimentally study various aspects of the runaway beams generated. In order to simulate the synchrotron radiation observed, one must have a basic understanding of both the kinetics of runaway electrons and the electromagnetic radiation emitted by charged particles in helical motion. In this chapter we will begin by studying particle motion in a magnetic field, which will turn out to be crucial to the synthetic synchrotron diagnostic introduced in Chapter 3, and leads to the natural introduction of a *guiding-center* for which the equations governing its motion are then derived. The concept of runaway electrons is then explained, and the key properties of runaway electrons are described. Finally, the formulas governing the electromagnetic radiation emitted by an electron in circular motion are derived, from which the formulas for the radiation emitted by an electron in helical motion can then be obtained. The main result of Section 2.3 are the formulas for the angular distribution and combined angular and spectral distribution of electromagnetic radiation emitted by an electron in helical motion. After deriving those formulas, the remainder of the chapter is dedicated to analyzing their asymptotic behaviour and validity in toroidal devices.

2.1 Electron motion

The equation of motion for an electron in electric and magnetic fields $\boldsymbol{E}$ and $\boldsymbol{B}$ is

$$\dot{\boldsymbol{p}} = -e\Big[\boldsymbol{E}(\boldsymbol{r},t) + \dot{\boldsymbol{r}} \times \boldsymbol{B}(\boldsymbol{r},t)\Big], \tag{2.1}$$

which is the celebrated Lorentz force law [20]. The first term on the right hand side (RHS) tells us that any electric field will act to accelerate the electron in the direction opposite of the field, while the second term gives rise to an acceleration which is perpendicular to both the electron's direction of motion and the direction of the magnetic field.

Let us for a moment neglect the electric field and assume that the magnetic field is constant in time and of the form $\boldsymbol{B} = B_0\hat{\boldsymbol{z}}$, where B_0 is a constant. The equations of motion (2.1) then reduce to

$$\ddot{\boldsymbol{r}} = \omega_B \dot{\boldsymbol{r}} \times \hat{\boldsymbol{z}}, \tag{2.2}$$

where we have introduced the cyclotron frequency $\omega_B = -eB_0/\gamma m$. Since $\hat{\boldsymbol{z}}$ is fixed and the electron's acceleration is always perpendicular to its direction of motion,

the electron will move in a helical orbit, as illustrated in Fig. 2.1. Any initial velocity component parallel to the magnetic field will be unaffected by the magnetic field and so will remain constant throughout the orbit of the electron, allowing the parametrization

$$\begin{cases} x(t) = x_0 - \frac{v_\perp}{\omega_B} \cos \omega_B t, \\ y(t) = y_0 - \frac{v_\perp}{\omega_B} \sin \omega_B t, \\ z(t) = z_0 + v_\parallel t. \end{cases} \tag{2.3}$$

Here we have introduced the electron's (initial) velocity components $v_\parallel$ and $v_\perp$ parallel and perpendicular to the magnetic field respectively, and the arbitrary translational constants x_0, y_0 and z_0. Sometimes it can be convenient to also talk about the particle's *pitch angle* θ_p, which is the angle the particle's velocity vector makes with the magnetic field, and in Chapter 4 it will be shown to have a significant impact on the synchrotron images.

The radius of the circular motion obtained from (2.3) is $\rho = v_\perp/\omega_B$, and the angular frequency with which the particle gyrates around the magnetic field is ω_B. These quantities motivate the introduction of the particle's *guiding-center*, which guides the helical trajectory of the particle through the magnetic field, and describes the average motion of the particle. Often when discussing particle orbits, it is this average motion that is of interest, and so one can talk about the generally quite smooth orbit of a particle's guiding-center rather than its full helical orbit. In Section 2.1.2, a transformation to a set of guiding-center coordinates separating the rapid gyro-motion from the average motion of the particle will be introduced, and the corresponding equations of motion will be shown.

An important concept when discussing charged particle motion in magnetic fields is that of *magnetic field lines*. Since the magnetic field is a vector quantity, it specifies a preferred direction in each point of space, and if we start in some point and move in the direction pointed out by the magnetic field, we will move along what is known as a magnetic field line. In a straight magnetic field, as considered in the discussion above, magnetic field lines are just straight lines. Since a charged particle is free to move along the parallel direction of the magnetic field, its guiding-center will approximately follow magnetic field lines.

As described in the introduction, only a toroidal magnetic field configuration is able to prevent significant end losses of particles, so the magnetic field confining the fusion plasma in a tokamak is mainly directed in the toroidal direction. It is generated by driving a current through a set of magnetic field coils that are wound around the torus, and from the theory of magnetostatics [24] we know that such a magnetic field behaves according to

$$\boldsymbol{B}(R) = \frac{B_0 R_0}{R} \hat{\boldsymbol{\phi}}, \tag{2.4}$$

where R is the distance from the point of symmetry to the point of interest, B_0 is the magnetic field strength on the magnetic axis, corresponding to $R = R_0$ and $\hat{\boldsymbol{\phi}}$ is a unit vector in the toroidal direction. As we will see in the next section, since the gradient of this magnetic field is not zero, this magnetic field gives rise to particle drifts that push particles against the outer wall of the device. To prevent this, a magnetic field is also applied in the poloidal direction in order to "twist" field lines.

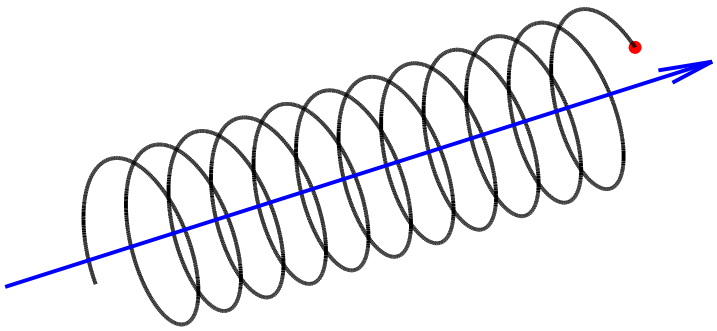

Figure 2.1: An electron in a straight magnetic field will follow a helical trajectory like the one shown above, circulating around a magnetic field line with frequency $\omega_B = eB_0/\gamma m$ and radius $\rho = v_\perp/\omega_B$.

This approach has proven highly successful and forms the basis for every magnetic fusion device currently in operation.

2.1.1 Orbit drifts

When the magnetic field is allowed to be inhomogeneous, the electron orbit will get perturbed, and the guiding-center of the orbit will appear to drift across magnetic field lines. We begin by adding a general force $\boldsymbol{F}$ acting on the particle to our equation of motion, with $\boldsymbol{B}$ still a uniform magnetic field:

$$\dot{\boldsymbol{p}} = -e\dot{\boldsymbol{r}} \times \boldsymbol{B}(\boldsymbol{r}, t) + \boldsymbol{F}. \tag{2.5}$$

Since the magnetic field $\boldsymbol{B}$ is still uniform here, the $\dot{\boldsymbol{r}} \times \boldsymbol{B}$ term only tells us about the helical motion and is of no further interest. By forming the vector cross product between $\boldsymbol{B}$ and both sides of Eq. (2.5), we get, after defining $B = |\boldsymbol{B}|$, the relation

$$\boldsymbol{v}_F = -\frac{\boldsymbol{F} \times \boldsymbol{B}}{eB^2}, \tag{2.6}$$

which is the velocity with which the electron *drifts* from a perfectly helical orbit due to a force $\boldsymbol{F}$. This general formula can be applied to any external force $\boldsymbol{F}$ and magnetic field $\boldsymbol{B}$. In particular we can apply it to an electric field $\boldsymbol{E}$, whose component $E_\parallel$ parallel to the magnetic field will simply give the particle an acceleration proportional to $E_\parallel$ in the parallel direction. We see however that the perpendicular component $E_\perp$ of $\boldsymbol{E}$ will give rise to an electric drift velocity of magnitude $E_\perp/B$ across the magnetic field lines.

As mentioned in the previous section, in a tokamak, magnetic field lines make circles, and so particle orbits should be similarly curved with some radius of curvature R_c. This however introduces a centrifugal force $\boldsymbol{F}_c = p_\parallel^2 \hat{\boldsymbol{r}}/\gamma m R_c$ which, as we know from (2.6), will give rise to a drift velocity [6]

$$\boldsymbol{v}_c = -\frac{\boldsymbol{F}_c \times \boldsymbol{B}}{eB^2} = -\frac{p_\parallel^2}{\gamma m e B^2} \boldsymbol{B} \times \nabla_\parallel \boldsymbol{b}, \tag{2.7}$$

where $\nabla_\parallel = \hat{\boldsymbol{b}} \cdot \nabla$, $\hat{\boldsymbol{b}} = \boldsymbol{B}/B$ and we used that $\hat{\boldsymbol{r}}/R_\mathrm{c} = -(\hat{\boldsymbol{b}} \cdot \nabla)\hat{\boldsymbol{b}}$.

If the strength of the magnetic field also varies in space (as we previously showed it does in a toroidal magnetic field), we can Taylor expand the magnetic field and put the higher order terms in $\boldsymbol{F}$. Typically, this is done in a small region of size $\rho = v_\perp/\omega_B$ around the guiding-center position, and after averaging the equation of motion over one gyro-period one obtains

$$\boldsymbol{v}_{\nabla B} = -\frac{p_\perp^2}{2\gamma m e B^2}(\hat{\boldsymbol{b}} \times \nabla B), \tag{2.8}$$

which is commonly referred to as the ∇B drift velocity. In a tokamak, both the curvature and ∇B drifts will be present, as well as the $\boldsymbol{E}\times\boldsymbol{B}$ drift when electric fields are taken into account, and the overall motion will be affected by a superposition of these.

2.1.2 Guiding-center coordinates

The average motion of the electron is well described by its so called guiding-center, as shown above. Often when studying particle orbits, it is not the rapid gyro-motion that is of interest, but rather this average guiding-center motion, and so it is convenient to make a change of coordinates in order to separate the gyro-motion from the rest. For this purpose a set of guiding-center coordinates are typically employed [25] which consists of the guiding-center position $\boldsymbol{X}$, the particle energy E, the magnetic moment $\mu = p_\perp^2/2mB$ and the gyro-phase ζ. The transformation to guiding-center coordinates relies on the adiabatic invariance of the magnetic moment μ, and in to first order in the guiding-center approximation the the magnetic moment is assumed constant.

The derivation of the guiding-center equations of motion for a relativistic particle is not very straightforward and contains a number of subtleties, so we choose to omit the full derivation in this text and instead refer the reader to [26]. The equations of motion for a relativistic particle are nonetheless very similar to those of a non-relativistic particle, and are

$$\dot{\mu} = 0, \tag{2.9}$$

$$\dot{\zeta} = \omega_B, \tag{2.10}$$

$$\dot{\boldsymbol{X}} = \frac{p_\parallel}{\gamma m}\hat{\boldsymbol{b}} - \frac{\hat{\boldsymbol{b}}}{\gamma m e B_\parallel^*} \times \left(\frac{p_\perp^2}{2B}\nabla B + p_\parallel^2 \nabla_\parallel \hat{\boldsymbol{b}}\right), \tag{2.11}$$

$$\dot{p}_\parallel = -\frac{\mu \boldsymbol{B}^*}{B_\parallel^*} \cdot \nabla B, \tag{2.12}$$

where $\boldsymbol{B}^* = \boldsymbol{B} - (p_\parallel/e)\nabla \times \hat{\boldsymbol{b}}$ is the effective magnetic field and $B_\parallel^* = \hat{\boldsymbol{b}} \cdot \boldsymbol{B}^*$. The first equation, Eq. (2.9), reveals that in the first-order guiding-center theory that this is, the magnetic moment is a constant. In reality μ is an adiabatic invariant that changes slowly over the course of the particle's orbit. The second equation, Eq. (2.10), relates the gyro angle ζ to the gyro frequency ω_B as expected by the definition of ζ.

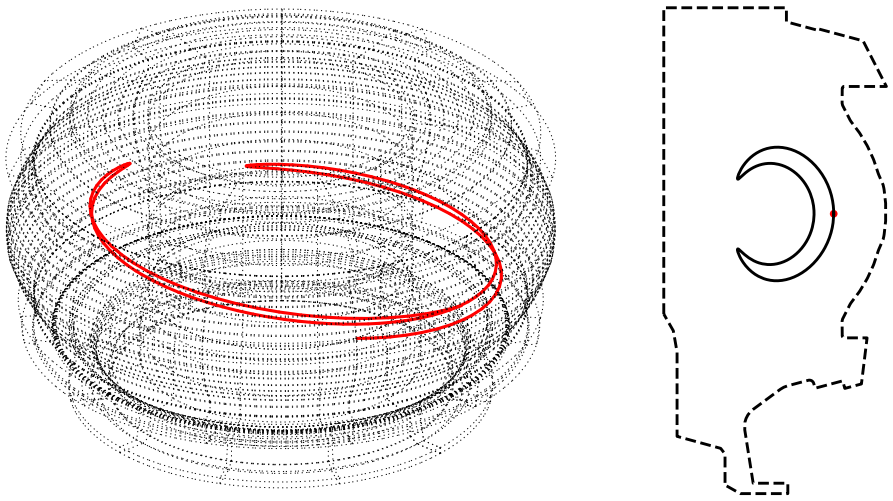

Figure 2.2: The banana orbit of a 10 MeV electron with $\cos\theta_\mathrm{p} = 0.5$ in the Alcator C-Mod tokamak [27]. In the left pane, the full 3D view of the orbit (solid red) is shown, with the dotted lines representing the extent of the vacuum vessel surrounding it. In the right pane the corresponding 2D poloidal projection of the orbit is shown, with the dashed line showing the wall cross section, the solid line being the orbit and the red dot marking the starting point of the electron.

The equation for $\dot{\boldsymbol{X}}$, Eq. (2.11), has an interesting form which allows us to identify the contributing terms as due to specific effects. The first term informs us that the guiding-center will move along the magnetic field lines, while the second and third terms can be identified as the ∇B and curvature drift terms respectively. Finally, Eq. (2.12) describes the change in the motion along magnetic field and as can be seen it vanishes in a homogeneous magnetic field. A typical magnetic field as used in magnetic fusion is however not homogeneous and leads the particle through regions where the magnetic field strength varies. According to Hamiltonian theory, if B is independent of time (which is true for the cases considered in this thesis), and if radiation losses as well effects of accelerating fields are assumed negligible, the energy (and thus also momentum) of the electron will be a constant of motion

$$p_0^2 = 2m\mu B + p_\parallel^2. \tag{2.13}$$

As the particle moves through regions of increasing B the μB term increases, forcing the parallel speed to decrease. For sufficiently small initial values of the ratio $p_\parallel/p$, the $p_\parallel$ term will vanish at some point along the orbit, forcing the particle to turn back and effectively causing it to bounce between two points in the magnetic field. Such a particle is referred to as a *trapped particle* and follows an orbit that has the shape of a banana in the poloidal plane, as shown in Fig. 2.2, thus giving rise to the term "banana orbit". The particles we will mostly be concerned with in this work are however characterized by $p_\parallel \gg p_\perp$, and are categorized as *passing particles*, following "passing orbits" which sweep over all poloidal angles, i.e. $p_\parallel$ doesn't change sign.

Numerical considerations

When tracing particle orbits numerically we are most often not interested in the gyro-motion of the particle and can therefore solve the guiding-center equations of motion (2.9)-(2.12), rather than the full equations of particle motion (2.1). Separation of the strongly oscillatory gyro-motion from the rather smooth guiding-center motion has positive effects on computational performance, allowing the use of longer timesteps, which also brings benefits such as more accurate energy conservation and shorter computation times.

The reasons for tracing the particle orbit in a synthetic synchrotron diagnostic will be made clear in Section 3.1, but already now we realize that the tool should solve for the guiding-center motion rather than the full particle motion, because of performance reasons. This however also requires that the quantity we are interested in, which in the case of a synthetic synchrotron diagnostic is the synchrotron radiation emitted, is expressed as a guiding-center quantity. Since the radiation is emitted by particles, the theory initially leads to an expression for the radiation emitted by individual particles. Luckily, the theory can be reformulated in terms of the guiding-center, which is done in the latter parts of Section 2.3.

2.2 Runaway electrons

As discussed in Section 2.1, an electric field acting in the direction parallel to the magnetic field will accelerate electrons in that direction. When an external electric field is applied, the plasma particles tend to rearrange so that the net electric field vanishes and the electric field is "shielded out". This, however, does not apply to induced electric fields, which may appear during various phases of operation, and when present will accelerate electrons along the toroidal direction. As we will see shortly, due to the friction force experienced by the electron decreasing with increased speed, this makes it possible for electrons to reach highly relativistic energies and "run away" from the thermal particles of the plasma [10, 11].

A key property of plasmas is the gradual and long-range interactions by which the constituent particles interact. In a gas, atoms appear to be uncharged (neutral) to their neighbours and no interaction occurs between them until they are very close to each other. The forces felt by atoms when interacting are therefore very strong so that collisions between atoms in a regular gas are often approximated as "hard-sphere" collisions. In a plasma however most atoms have been ionized meaning interactions are governed by long-range electromagnetic interactions which cause "soft" collisions that typically only affect the path and momentum of the particles slightly in each interaction. The effective friction force acting on a suprathermal electron due to collisions with other electrons can be shown to be [28]

$$F_{\mathrm{C},\parallel} = \frac{1}{v^2}\frac{n_{\mathrm{e}} e^4 \ln\Lambda}{4\pi\varepsilon_0^2 m}, \tag{2.14}$$

where n_{e} is the number density of electrons, $\ln\Lambda$ is the Coulomb logarithm and ε_0 is the vaccum permittivity. In Fig. 2.3 the friction force experienced by an electron in a plasma is plotted as a function of the speed of the particle, and it attains its

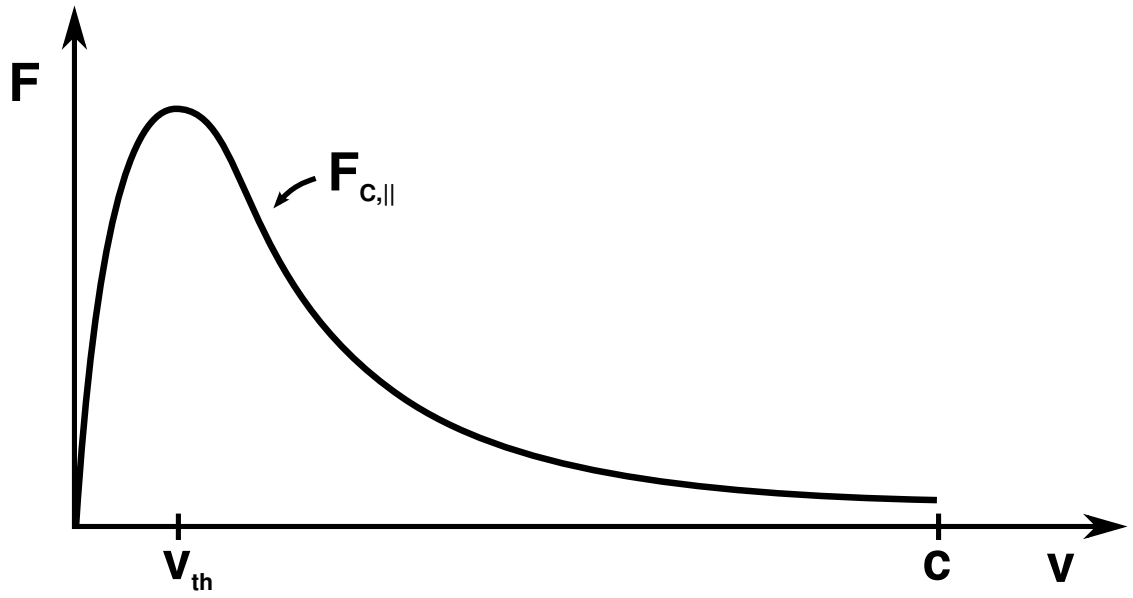

Figure 2.3: Schematic plot of the friction force experienced by an electron in a plasma, as a function of its speed. From [29], Reproduced with permission.

maximum value in $v = v_{\text{th}}$, the thermal speed of electrons in the plasma. It is interesting to note that for $v \gtrsim v_{\text{th}}$ the friction force decreases, which, as we will soon see, has important implications.

When an electric field with a component $E_\parallel$ parallel to the magnetic field is present, the electron will be accelerated in the parallel direction by a force of magnitude $-eE_\parallel$. This acceleration will be countered by the friction force (2.14), and by looking at Fig. 2.3 we see that if the speed of the electron is greater than v_{th} and $eE_\parallel > F_{\text{C},\parallel}$ the electron will be accelerated towards even greater speeds, while the friction force decreases. Thus, in the presence of a sufficiently strong electric field, parts of the electron population will be able to reach significant energies and will "run away" from the thermal population, and if control of the runaway beam is lost they may collide with the wall, potentially causing severe damage. It should be noted that there is in fact an upper limit to the runaway speed, since at highly relativistic energies radiation reaction forces due to the emission of synchrotron radiation and bremsstrahlung become important. These forces always increase with the electron speed, and so cause the friction force experienced by the electron to go up again once it becomes fast enough [22, 30, 31].

The production of runaway electrons requires a strong electric field to be sustained for a long period of time, something which is not common during typical fusion operation. In the tokamak family of devices however, so called disruptions can occur, at which point strong electric fields can be induced. In current experiments, runaways are generally not a big problem, but since the number of generated runaways are predicted to scale exponentially with the current it is expected that in future devices, including ITER, mitigating runaway electrons will be of great importance [18].

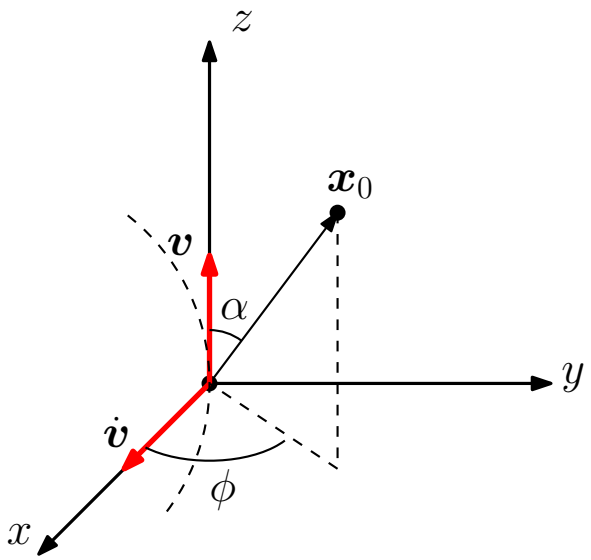

Figure 2.4: An electron in motion in a homogeneous magnetic field $\boldsymbol{B} = B_0\hat{\boldsymbol{z}}$, situated in origo at time $t = 0$.

2.3 Synchrotron radiation

Charged particles undergoing acceleration emit electromagnetic radiation [21], and when this radiation arises due to the electron being in circular motion it is referred to as *cyclotron radiation*. As was discussed in Sec. 2.1, electrons in tokamak magnetic fields will move in helical orbits around the tokamak, meaning they will emit cyclotron radiation both due to the rapid gyro-motion around magnetic field lines but also due to the larger circular motion around the tokamak. If the electron is relativistic, i.e. has an energy such that $\gamma \gg 1$, the emitted radiation has (as we will show in Section 2.3.2) a characteristic angular and spectral distribution and is referred to as *synchrotron radiation*. Within magnetic fusion, synchrotron radiation was first used in the early 1990's in the TEXTOR tokamak to diagnose runaway electrons [19] and has since become a standard diagnostic in many other devices.

In what follows, a number of formulas relating to the angular and spectral distributions of synchrotron radiation in circular and helical motion will be derived. The derivations follow the approach of Jackson [21] as far as possible, and combines them with other sources and original ideas where necessary.

2.3.1 Electron in circular motion

Consider an electron in arbitrary motion as shown in Fig. 2.4. Let $\boldsymbol{r}(t)$ denote the position of the electron at time t, $\boldsymbol{v}(t) = \dot{\boldsymbol{r}}(t)$, and let the coordinate system (x, y, z) be defined so that $\boldsymbol{r}(t = 0) = 0$. We introduce the angles α and φ by making the definitions

$$\begin{aligned} \boldsymbol{n} \cdot \boldsymbol{v} &= v \cos\alpha, \\ \boldsymbol{n} \cdot \dot{\boldsymbol{v}} &= \sin\alpha \cos\varphi, \end{aligned} \tag{2.15}$$

where $\boldsymbol{n}$ is a unit vector in the direction from the particle to the observer.

The electric and magnetic fields in the observation point $\boldsymbol{x}$ at observer time $t = 0$ due to the electron are given by the Liénard-Wiechert fields [21]

$$\boldsymbol{E}(\boldsymbol{r},t) = \frac{e}{4\pi\epsilon_0}\left[\frac{\boldsymbol{n}-\boldsymbol{\beta}}{\gamma^2\left(1-\boldsymbol{\beta}\cdot\boldsymbol{n}\right)^3 R^2}\right]_{\text{ret}} + \frac{e}{4\pi\epsilon_0 c}\left[\frac{\boldsymbol{n}\times\left\{(\boldsymbol{n}-\boldsymbol{\beta})\times\dot{\boldsymbol{\beta}}\right\}}{(1-\boldsymbol{\beta}\cdot\boldsymbol{n})^3 R}\right]_{\text{ret}}, \quad (2.16)$$

$$\boldsymbol{B}(\boldsymbol{r},t) = \frac{1}{c}\left[\boldsymbol{n}\times\boldsymbol{E}(\boldsymbol{r},t)\right]_{\text{ret}}. \quad (2.17)$$

Here, $R(t) = |\boldsymbol{x}-\boldsymbol{r}(t)|$, $\boldsymbol{n} = [\boldsymbol{x}-\boldsymbol{r}(t)]/R$ is the observation direction, $\boldsymbol{\beta} = \boldsymbol{v}/c$ is the normalized velocity of the electron and the subscript "ret" denotes that all quantities are to be evaluated at the retarded time $t' = t - R(t')/c$, when the electron emitted the radiation.

The two terms in (2.16) are referred to as the *velocity* and *acceleration* fields respectively, since the value of the first term is determined mainly by the electron's velocity, while the second term also depends on its acceleration. The velocity field falls of as R^{-2}, essentially like a static field, while the acceleration field goes as R^{-1} which is typical for a radiation field. Far away from the electron (where the observer is typically situated), the emitted radiation will thus almost entirely come from the acceleration field, allowing us to neglect the first term of (2.16) in the following analysis.

From the definition of the Poynting vector, which we will denote by $\boldsymbol{S}$, it follows together with Eqs. (2.16) and (2.17) that

$$\boldsymbol{S} = \frac{1}{\mu_0}\boldsymbol{E}\times\boldsymbol{B} \approx \frac{1}{\mu_0 c}|\boldsymbol{E}|^2\boldsymbol{n}. \quad (2.18)$$

The radial component of this vector, $\boldsymbol{S}\cdot\boldsymbol{n}$, can be interpreted as the energy per unit area per unit time reaching the observer. Inserting Eqs. (2.16) and (2.17) we obtain

$$\frac{\mathrm{d}\tilde{P}(t)}{\mathrm{d}\Omega} = \frac{e^2}{16\pi^2\epsilon_0 c}\frac{\left|\boldsymbol{n}\times\left\{(\boldsymbol{n}-\boldsymbol{\beta})\times\dot{\boldsymbol{\beta}}\right\}\right|^2}{(1-\boldsymbol{\beta}\cdot\boldsymbol{n})^6}, \quad (2.19)$$

which is the power received by the observer per unit solid angle. The reader should note that all quantities on the RHS in the above formula are to be evaluated at the retarded time $t' = t - R(t')/c$, and so (2.19) represents the power received at time t in the lab frame as emitted by the electron at time t'. During an infinitesimal time interval $\mathrm{d}t$ in the lab frame the electron has a time $\mathrm{d}t' = (1-\boldsymbol{\beta}\cdot\boldsymbol{n})^{-1}\mathrm{d}t$ to emit radiation, and so if we are interested in the total energy emitted during a finite interval of time we should integrate the quantity

$$\frac{\mathrm{d}P}{\mathrm{d}\Omega} \equiv \frac{\mathrm{d}\tilde{P}}{\mathrm{d}\Omega}\frac{\mathrm{d}t}{\mathrm{d}t'} = \frac{e^2}{16\pi^2\epsilon_0 c}\frac{\left|\boldsymbol{n}\times\left\{(\boldsymbol{n}-\boldsymbol{\beta})\times\dot{\boldsymbol{\beta}}\right\}\right|^2}{(1-\boldsymbol{\beta}\cdot\boldsymbol{n})^5}, \quad (2.20)$$

which we define as the power radiated into a solid angle $\mathrm{d}\Omega$ by an electron in circular motion.

Frequency distribution

If the various frequency components radiated by the electron are also of interest, such as when a camera with a limited wavelength range is used for observation, we can define the power more generally in terms of the quantity $\boldsymbol{A}(t) = [R\boldsymbol{E}]_{\text{ret}}$ as

$$\frac{\mathrm{d}P(t)}{\mathrm{d}\Omega} = |\boldsymbol{A}(t)|^2. \tag{2.21}$$

From Parseval's theorem it then follows that

$$\int_{-\infty}^{\infty} \frac{\mathrm{d}P}{\mathrm{d}\Omega}\mathrm{d}t = \int_{-\infty}^{\infty} |\boldsymbol{A}(t)|^2 \mathrm{d}t = \int_{-\infty}^{\infty} |\boldsymbol{A}(\omega)|^2 \mathrm{d}\omega, \tag{2.22}$$

where $\boldsymbol{A}(\omega)$ is the Fourier transform of $\boldsymbol{A}(t)$, which we define as

$$\boldsymbol{A}(\omega) = \frac{1}{\sqrt{2\pi}} \int_{-\infty}^{\infty} \boldsymbol{A}(t) e^{i\omega t} \mathrm{d}t. \tag{2.23}$$

Since $\boldsymbol{A}(\omega)$ is also real, the sign of the frequency ω doesn't matter, and we choose to integrate over only positive frequencies in order to obtain

$$\int_{-\infty}^{\infty} \frac{\mathrm{d}P}{\mathrm{d}\Omega}\mathrm{d}t = \int_{0}^{\infty} \left(|\boldsymbol{A}(\omega)|^2 + |\boldsymbol{A}(-\omega)|^2 \right) \mathrm{d}\omega = 2\int_{0}^{\infty} |\boldsymbol{A}(\omega)|^2 \mathrm{d}\omega. \tag{2.24}$$

This last equality motivates the introduction of the quantity

$$\frac{\mathrm{d}^2 I}{\mathrm{d}\omega \mathrm{d}\Omega} = 2|\boldsymbol{A}(\omega)|^2, \tag{2.25}$$

which we interpret as the energy radiated per unit solid angle per unit frequency interval.

By substituting the expression for $\boldsymbol{A}(t)$ and integrating over the electron's time t' instead of the observer time t, we can write the radiated energy as

$$\frac{\mathrm{d}^2 I}{\mathrm{d}\omega \mathrm{d}\Omega} = \frac{e^2}{16\pi^2 \epsilon_0 c} \left| \int_{-\infty}^{\infty} \frac{\boldsymbol{n} \times \left[(\boldsymbol{n} - \boldsymbol{\beta}) \times \dot{\boldsymbol{\beta}} \right]}{(1 - \boldsymbol{\beta} \cdot \boldsymbol{n})^2} e^{i\omega[t' + R(t')/c]} \mathrm{d}t' \right|^2. \tag{2.26}$$

If the observer is far away from the electron, we can assume that the distance $R(t') \approx |\boldsymbol{x}| - \boldsymbol{n} \cdot \boldsymbol{r}(t')$. Identifying the expression in front of the exponential as a perfect differential then allows us to integrate by parts and obtain the final expression

$$\frac{\mathrm{d}^2 I}{\mathrm{d}\omega \mathrm{d}\Omega} = \frac{e^2 \omega^2}{16\pi^2 \epsilon_0 c} \left| \int_{-\infty}^{\infty} \boldsymbol{n} \times (\boldsymbol{n} \times \boldsymbol{\beta}) e^{i\omega[t - \boldsymbol{n} \cdot \boldsymbol{r}(t)/c]} \mathrm{d}t \right|^2, \tag{2.27}$$

where the electron time t' was renamed t for notational convenience.

2.3.2 Angular distribution of synchrotron radiation

We can obtain the angular distribution of synchrotron radiation for an electron in instantaneous circular motion by evaluating the formula (2.20). From Fig. 2.4 we obtain expressions for $\boldsymbol{n}$, $\boldsymbol{\beta}$ and $\dot{\boldsymbol{\beta}}$ at $t = 0$ as

$$\begin{aligned} \boldsymbol{n} &= \hat{\boldsymbol{x}} \sin\alpha \cos\phi + \hat{\boldsymbol{y}} \sin\alpha \sin\phi + \hat{\boldsymbol{z}} \cos\alpha, \\ \boldsymbol{\beta} &= \beta \hat{\boldsymbol{z}}, \\ \dot{\boldsymbol{\beta}} &= \dot{\beta} \hat{\boldsymbol{x}} = \omega_B \beta \hat{\boldsymbol{x}}. \end{aligned} \tag{2.28}$$

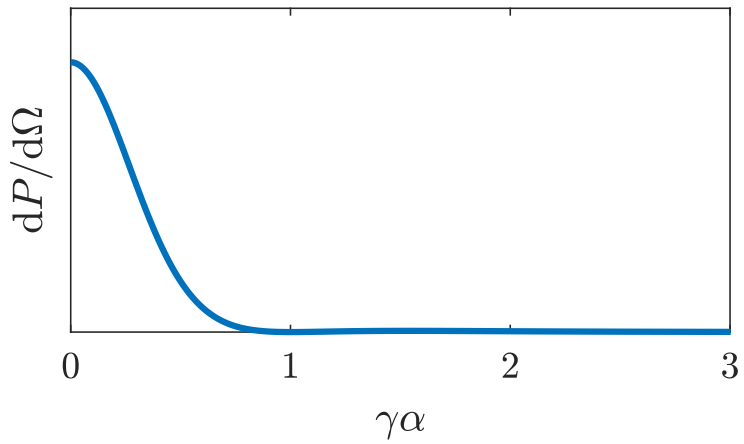

Figure 2.5: Angular distribution of radiation due to an electron in instantaneous circular motion. The observation angle is given in units of $1/\gamma$.

Inserting the above expressions into the formula for $\mathrm{d}P/\mathrm{d}\Omega$, Eq. (2.20), we obtain

$$\frac{\mathrm{d}P}{\mathrm{d}\Omega} = \frac{e^2\dot{\beta}^2}{16\pi^2\epsilon_0 c}\left[\frac{1}{(1-\beta\cos\alpha)^3} - \frac{\sin^2\alpha\cos^2\phi}{\gamma^2(1-\beta\cos\alpha)^5}\right], \tag{2.29}$$

which is the total power radiated by an electron in instantaneous circular motion. The distribution has a maximum in the forward direction of the particle $\alpha = 0$, and is large while $1-\beta\cos\alpha \approx (1/2)(1-\beta^2+\alpha^2)$ is small, suggesting the width of the emitted radiation is $\sim \sqrt{1-\beta^2} = 1/\gamma$. This feature is also illustrated in Fig. 2.5, where the angle α is given in units of $1/\gamma$.

Transforming to helical motion

From the theory of particle motion we know that a particle in a magnetic field will both undergo circular motion around the magnetic field lines, as well as motion along the magnetic field lines, following a helical path. Equation (2.29) applies to an electron in purely circular motion, but to obtain a similar formula for a particle in helical motion we can make a Lorentz boost in the parallel direction [32]. Let K denote the lab frame, and let K' be the inertial frame in which the electron undergoes purely circular motion, which is in relative motion to K with relative speed $v_\parallel$ along the magnetic field lines of a static homogeneous magnetic field. The two frames are then connected by the Lorentz factor $\gamma_\parallel = 1/\sqrt{1-\beta_\parallel^2}$ and the electron's Lorentz factor in K becomes $\gamma_K = \gamma_{K'}\gamma_\parallel$. Accordingly, the gyro frequency of the electron appears different in the two frames, with $\omega'_B/\gamma_\parallel = eB'/\gamma_{K'}\gamma_\parallel m = \omega_B$ in K, since the fact the Lorentz boost was done in the parallel direction causes $B' = B$.

The detector receives bursts of radiation each time the electron's velocity vector is directed towards it. In K' the period time of the electron is given by $\tau_{K'} = 2\pi/\omega'_B$, while in K the period time is $\tau_K = 2\pi/\omega_B$, meaning that the time between bursts of radiation received by the observer in K is shorter by a factor ω_B/ω'_B. Further, due to time-dilation, frequencies are Doppler-shifted by

$$\nu_K = \nu_{K'}\gamma_\parallel(1+\beta\cos\theta') \approx \nu_{K'}\gamma_\parallel, \tag{2.30}$$

where θ' is the angle between the radiation and the magnetic field in K'. Since most of the radiation is emitted within an interval of size $\sim 2\gamma^{-1}$ around the velocity vector, and since the electron moves in a circular orbit perpendicular to the magnetic field in K', $|\cos\theta'| \lesssim |\cos(\pi/2+\gamma^{-1})| \approx 0$. The angular frequency is therefore shifted according to (2.30), and the period time shifts accordingly, to become

$$\tau_K = (\omega_B/\omega'_B)\tau_{K'}/\gamma_\parallel = \tau_{K'}/\gamma_\parallel^2. \tag{2.31}$$

The power is thus scaled by a factor $\tau_{K'}/\tau_K$ and can be related to the power received from an electron in circular motion by

$$P_{\text{helical}} = \frac{\tau_{K'}}{\tau_K} P_{\text{circular}} = \gamma_\parallel^2 P_{\text{circular}}. \tag{2.32}$$

This relation allows us to transform any formula giving the power received from an electron in circular motion to a formula giving the power received from an electron in helical motion. Care must be taken however when using the above relation, since quantities depending on the direction between the velocity and the magnetic field must also be replaced appropriately. To transform Eq. (2.29) for example we must make sure to replace β in the expression for $\dot{\beta}$ with $\beta_\perp$, since the magnitude of the acceleration depends on the pitch angle.

In the remainder of this chapter we will study the power received by a detector from a single electron in helical motion. When the radiation observed stems from a stationary distribution of electrons however, as is the case in a synthetic synchrotron diagnostic, the power received should be re-scaled according to [33]

$$P_{\text{dist}} = \frac{P_{\text{part}}}{1 - \beta\cos\theta_{\text{p}}\cos\mu}, \tag{2.33}$$

because the particle appears to traverse a given volume element for a shorter time than the time it actually takes, where θ_{p} is the particle's pitch angle $\theta_{\text{p}} = \arccos v_\parallel/v$, μ is the angle between $\boldsymbol{n}$ and the guiding-center velocity vector, P_{dist} denotes the radiation emitted from a distribution of particles (per particle with the given pitch angle and energy), and P_{part} is the radiation emitted by an individual particle. The physical reason for this additional factor can be understood by noting that a stationary distribution of particles will always ensure that the number of particles within a small volume element remains constant, while a "distribution" consisting of only a single particle will only radiate within the volume element during a finite time.

Guiding-center angular distribution

As discussed in Section 2.1.2 it is computationally much more efficient to follow the guiding-center of an electron, rather than following the electron itself. We would therefore like a formula such as (2.29) describing the emission from the guiding-center instead. This can be derived in the following manner: due to the immense number of electrons in a plasma, many of them will share the same guiding-centers but will be located at different gyro-angles. The strong magnetic fields present in magnetic confinement fusion plasmas cause the gyration around field lines to

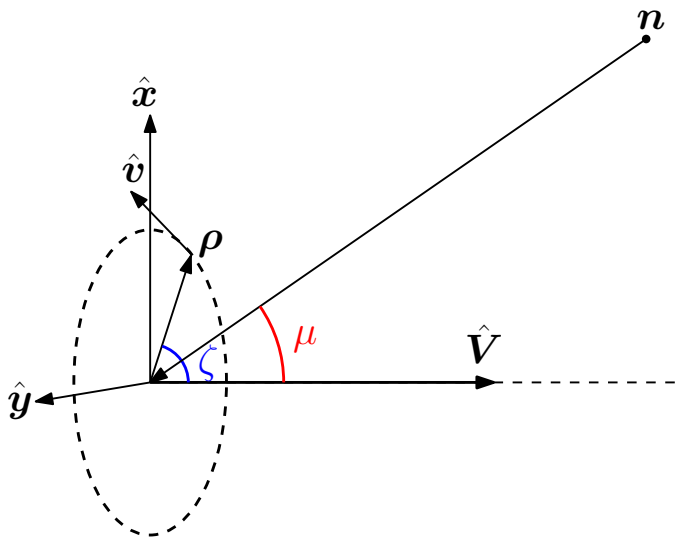

Figure 2.6: Illustration of how the guiding-center coordinates μ and ζ are defined in terms of the observation vector $\boldsymbol{n}$, the electron and guiding-center velocities $\boldsymbol{v}$ and $\boldsymbol{V}$.

typically be the fastest process in the plasma, and as a result the electrons will be uniformly distributed in gyro-angle. This uniform distribution of electrons in gyro-angle allows us to define the *gyro average* of some quantity $F(\zeta)$ as

$$\langle F \rangle = \frac{1}{2\pi} \int_0^{2\pi} F(\zeta) \mathrm{d}\zeta. \tag{2.34}$$

We next transform the coordinates α and ϕ of (2.29) to a set of "guiding-center" coordinates. As before we let ζ denote the gyro-angle and let μ be the angle between the observation vector $\boldsymbol{n}$ and the guiding-center velocity $\boldsymbol{V}$. With the help of Fig. 2.6 we write

$$\begin{aligned} \boldsymbol{v} &= v(\hat{\boldsymbol{x}} \sin\theta_\mathrm{p} \cos\zeta + \hat{\boldsymbol{y}} \sin\theta_\mathrm{p} \sin\zeta + \hat{\boldsymbol{z}} \cos\theta_\mathrm{p}), \\ \dot{\boldsymbol{v}} &= \dot{v}(-\hat{\boldsymbol{x}} \sin\theta_\mathrm{p} \sin\zeta + \hat{\boldsymbol{y}} \sin\theta_\mathrm{p} \cos\zeta), \\ \boldsymbol{V} &= V\hat{\boldsymbol{z}}, \quad \boldsymbol{n} = \hat{\boldsymbol{x}} \sin\mu + \hat{\boldsymbol{z}} \cos\mu. \end{aligned} \tag{2.35}$$

By definition of α and ϕ it follows that

$$\cos\alpha = \boldsymbol{v} \cdot \boldsymbol{n}/v = \cos\mu\cos\theta_\mathrm{p} + \sin\mu\sin\theta_\mathrm{p}\cos\zeta, \tag{2.36}$$

$$\cos\phi = \dot{\boldsymbol{v}} \cdot \boldsymbol{n}/\dot{v}\sin\alpha = -\sin\mu\sin\zeta/\sin\alpha, \tag{2.37}$$

and inserting these expressions into the helical version of (2.29) we obtain the power received per unit solid angle in the new set of guiding-center coordinates:

$$\frac{\mathrm{d}P}{\mathrm{d}\Omega} = \frac{e^2\omega_B^2\beta_\perp^2\gamma_\parallel^2}{16\pi^2\epsilon_0 c} \frac{1}{\kappa^3(1-\eta\cos\zeta)^3} \left[1 - \left(\frac{\sin\mu}{\gamma\kappa}\right)^2 \frac{\sin^2\zeta}{(1-\eta\cos\zeta)^2}\right]. \tag{2.38}$$

To simplify the expression the following quantities have been introduced:

$$\begin{aligned} \kappa &= 1 - \beta\cos\mu\cos\theta_\mathrm{p}, \\ \eta &= \kappa^{-1}\beta\sin\mu\sin\theta_\mathrm{p}, \end{aligned}$$

Since the gyro-phase angle ζ now appears explicitly in (2.38), and since all other angles are independent of ζ, we can carry out a gyro-average of the formula. Utilizing the standard integral

$$\frac{1}{2\pi}\int_0^{2\pi}\frac{\cos^m x}{(1-y\cos x)^{n+1}}\mathrm{d}x = \frac{z}{y^m}\sum_{k=0}^{m}(-1)^k\binom{m}{k}z^{n-k}P_{n-k}(z), \tag{2.39}$$

where $z=(1-y^2)^{-1/2}$ and $P_n(z)$ is the Legendre polynomial of degree n, we obtain the final gyro-averaged power per unit solid angle

$$\begin{aligned}\left\langle\frac{\mathrm{d}P}{\mathrm{d}\Omega}\right\rangle &\equiv \frac{1}{2\pi}\int_0^{2\pi}\frac{\mathrm{d}P}{\mathrm{d}\Omega}\mathrm{d}\zeta = \\ &= \frac{e^2\omega_B^2\beta_\perp^2\gamma_\parallel^2}{16\pi^2\epsilon_0 c\kappa^3}\left[p_1(\mu)-\left(\frac{\sin\mu}{\gamma\kappa}\right)^2 p_2(\mu)\right],\end{aligned} \tag{2.40}$$

where

$$\xi=(1-\eta^2)^{-1/2}, \qquad p_1(\mu)=\frac{\xi^3}{2}\left(3\xi^2-1\right), \qquad p_2(\mu)=\frac{\xi^5}{8}\left(5\xi^2-1\right).$$

The gyro-averaged guiding-center angular distribution (2.40) shows a peak in the direction $\mu=\theta_\mathrm{p}$, just as expected due to the relation between the electron's and its guiding-center's velocity vectors. The width of the angular distribution is determined by ξ, which can be shown to equal

$$\xi=\frac{\kappa}{\sqrt{1-\beta\cos\psi}\sqrt{1-\beta\cos(\psi+2\theta_\mathrm{p})}}. \tag{2.41}$$

We see that this ratio will always be dominated by the factor $\sqrt{1-\beta\cos\psi}\approx\sqrt{(1/2)(\gamma^{-2}+\psi^2)}$, and so the angular spread of radiation is $\sim\gamma^{-1}$ as in the non-gyroaveraged case.

2.3.3 Angular and spectral distribution

In Section 2.3.1 we derived the general expression in Eq. (2.27) for the total radiated intensity in a frequency interval $\mathrm{d}\omega$ per unit solid angle, by an electron in arbitrary accelerated motion. By once again considering an electron in pure circular motion, and using guiding-center coordinates as in Fig. 2.6, we find that

$$\begin{aligned}\boldsymbol{n}\times(\boldsymbol{n}\times\boldsymbol{\beta}) &= \beta\left(\hat{\boldsymbol{z}}\sin\mu\cos\mu\cos\zeta-\hat{\boldsymbol{x}}\cos^2\mu\cos\zeta-\hat{\boldsymbol{y}}\sin\zeta\right)= \\ &= \beta\left(\boldsymbol{\epsilon}_\perp\cos\mu\cos\zeta-\boldsymbol{\epsilon}_\parallel\sin\zeta\right).\end{aligned}$$

The vectors $\boldsymbol{\epsilon}_\parallel=\hat{\boldsymbol{y}}$ and $\boldsymbol{\epsilon}_\perp=\hat{\boldsymbol{z}}\sin\zeta-\hat{\boldsymbol{x}}\cos\mu\cos\zeta$ are the polarization vectors, with $\boldsymbol{\epsilon}_\parallel$ corresponding to polarization in the orbit plane, and $\boldsymbol{\epsilon}_\perp$ to polarization orthogonal to $\boldsymbol{\epsilon}_\parallel$ and $\boldsymbol{n}$. Similarly we can write the exponent of Eq. (2.27) as

$$\omega\left(t-\frac{\boldsymbol{n}\cdot\boldsymbol{r}(t)}{c}\right)=\omega\left(t-\frac{v_\perp}{\omega_B c}\sin\mu\sin\zeta\right), \tag{2.42}$$

The gyro-phase angle ζ can be parametrized in time as $\zeta = \omega_B t$, and from studying the angular distribution of synchrotron radiation we know that most of the radiation will be emitted along the electron's velocity vector. Most of the radiation therefore reaches the detector when the angle between the observer and the electron's velocity vector is at a minimum, which is when $\zeta = 0$. A Taylor expansion of (2.42) then allows us to turn the exponent of Eq. (2.27) into

$$\begin{aligned} \omega\left(t - \frac{\boldsymbol{n}\cdot\boldsymbol{r}(t)}{c}\right) &\approx \omega\left[t\left(1-\beta\sin\mu\right) + \frac{\beta}{6}\omega_B^2 t^3 \sin\mu\right] = \\ &= \frac{3}{2}\tilde{\xi}\left(x + \frac{1}{3}x^3\right), \end{aligned} \tag{2.43}$$

where

$$x = \omega_B t\sqrt{\frac{(\beta/2)\sin\mu}{1-\beta\sin\mu}}, \qquad \tilde{\xi} = \frac{2\omega}{3\omega_B}\sqrt{\frac{(1-\beta\sin\mu)^3}{(\beta/2)\sin\mu}}. \tag{2.44}$$

The total intensity in a frequency interval $\mathrm{d}\omega$ per unit solid angle can then be written

$$\frac{\mathrm{d}^2 I}{\mathrm{d}\omega\mathrm{d}\Omega} = \frac{e^2\omega^2}{16\pi^2\epsilon_0 c}\left|\boldsymbol{\epsilon}_\perp A_\perp(\omega) - \boldsymbol{\epsilon}_\parallel A_\parallel(\omega)\right|^2, \tag{2.45}$$

with

$$\begin{aligned} A_\perp(\omega) &\approx \frac{\beta\cos\mu}{\omega_B}\sqrt{\frac{1-\beta\sin\mu}{(\beta/2)\sin\mu}}\int_{-\infty}^{\infty}\exp\left\{i\frac{3}{2}\tilde{\xi}\left[x+\frac{1}{3}x^3\right]\right\}\mathrm{d}x, \\ A_\parallel(\omega) &\approx \frac{\beta}{\omega_B}\left(\frac{1-\beta\sin\mu}{(\beta/2)\sin\mu}\right)\int_{-\infty}^{\infty} x\exp\left\{i\frac{3}{2}\tilde{\xi}\left[x+\frac{1}{3}x^3\right]\right\}\mathrm{d}x. \end{aligned} \tag{2.46}$$

These integrals can be identified as modified Bessel functions of fractional order $1/3$ and $2/3$ respectively, and substitution into (2.45) yields

$$\frac{\mathrm{d}^2 I}{\mathrm{d}\omega\mathrm{d}\Omega} = \frac{e^2\beta^2\omega^2}{12\pi^2\omega_B^2\epsilon_0 c}\left(\frac{1-\beta\sin\mu}{\beta\sin\mu}\right)^2\left[K_{2/3}^2(\tilde{\xi}) + \frac{(\beta/2)\sin\mu\cos^2\mu}{1-\beta\sin\mu}K_{1/3}^2(\tilde{\xi})\right]. \tag{2.47}$$

Due to the behaviour of the Bessel functions, this expression will be large for small $\tilde{\xi}$ and negligible beyond $\tilde{\xi} \approx 1/2$. Since $\tilde{\xi}$ depends on both the frequency ω and the observation angle μ, we see that (2.47) will be large for large μ, and tend to zero as $\mu \to 0$. As we increase the frequency, the interval of angles μ within which $\tilde{\xi} < 1/2$ and (2.47) is significant diminishes, and beyond some frequency $\tilde{\omega_\mathrm{c}}$ the argument $\tilde{\xi}$ will be large for all angles, making contributions from frequencies above $\tilde{\omega_\mathrm{c}}$ negligible. Setting $\tilde{\xi} = 1/2$, we get at $\mu = \pi/2$ that the critical frequency $\tilde{\omega_\mathrm{c}}$ of the emitted radiation can be expressed in terms of the gyro-frequency ω_B according to

$$\tilde{\omega_\mathrm{c}} = \frac{3\omega_B}{4}\sqrt{\frac{\beta/2}{(1-\beta)^3}} \approx \frac{3}{2}\gamma^3\omega_B. \tag{2.48}$$

The approximate expression for the critical frequency given here, which is in common use in the literature today, was first introduced by Schwinger [34] in his seminal 1949 paper on classical radiation from electrons. To obtain the expression, $\beta \approx 1$ was assumed. Despite trying to refrain from unnecessary approximations in this text,

the critical frequency will be an exception, since the approximate form in Eq. (2.48) allows informative re-writing of many of the expressions that follow.

To instead compute the power received in a frequency interval $\mathrm{d}\omega$ per unit solid angle from an electron in helical motion, we divide the intensity by the gyro-period of the helically moving electron $\tau = 2\pi/\omega_B\gamma_\parallel^2$, as described in Sec. 2.3.2. Effectively, we are Lorentz-boosting the expression (2.47), so the angle μ must be changed to $\mu + (\pi/2 - \theta_\mathrm{p})$, and for convenience we introduce the new angle $\psi \equiv \mu - \theta_\mathrm{p}$ between the observer and the direction of peak emission. Due to the Lorentz boost, we must also change the critical frequency $\tilde{\omega_\mathrm{c}}$ and $\tilde{\xi}$ to

$$\tilde{\omega_\mathrm{c}} \quad \longrightarrow \quad \omega_\mathrm{c} = \frac{\tilde{\omega_\mathrm{c}}}{\gamma_\parallel} \approx \frac{3\gamma^3\omega_B}{2\gamma_\parallel}, \tag{2.49}$$

$$\tilde{\xi} \quad \longrightarrow \quad \xi = \gamma_\parallel\tilde{\xi} = \gamma^3\frac{\omega}{\omega_\mathrm{c}}\sqrt{\frac{(1-\beta\cos\psi)^3}{(\beta/2)\cos\psi}}. \tag{2.50}$$

Finally, we can write the angular and spectral distribution of electromagnetic radiation for an electron in helical motion

$$\begin{aligned}\frac{\mathrm{d}^2P}{\mathrm{d}\omega\mathrm{d}\Omega} = \frac{3e^2\beta^2\gamma^6\omega_B}{32\pi^3\epsilon_0 c}\left(\frac{\omega}{\omega_\mathrm{c}}\right)^2\left(\frac{1-\beta\cos\psi}{\beta\cos\psi}\right)^2 \times \\ \times\left[K_{2/3}^2(\xi) + \frac{(\beta/2)\cos\psi\sin^2\psi}{1-\beta\cos\psi}K_{1/3}^2(\xi)\right].\end{aligned} \tag{2.51}$$

As with the pure angular distribution (2.40), the angular and spectral distribution (2.51) is strongly peaked in the direction $\mu = \theta_\mathrm{p}$, i.e. it emits a cone of radiation around the guiding-center of the electron. A gyro-average was implicitly carried out as part of evaluating the integrals (2.46), since they were integrated along the electron's circular gyro-orbit, and so Eq. (2.51) is truly the angular and spectral equivalent to the gyro-averaged angular distribution (2.40).

Asymptotic behaviour

Detailed insight can be gained about the angular and spectral distribution (2.51) by studying its asymptotic behaviour in various limits. We note that the overall behaviour of the distribution is determined by the Bessel functions, and thus by the behaviour of the parameter ξ given by Eq. (2.50), and in the two limits $\xi \to 0$ and $\xi \to \infty$, these go approximately as

$$\begin{aligned}K_\nu(\xi) &\approx \frac{\Gamma(\nu)}{2}\left(\frac{2}{\xi}\right)^\nu, \qquad \sqrt{\nu+1} \gg \xi, \\ K_\nu(\xi) &\approx \sqrt{\frac{\pi}{2\xi}}e^{-\xi}, \qquad\qquad\quad \xi \gg 1,\end{aligned} \tag{2.52}$$

where $\Gamma(x)$ is the gamma function. As $\xi \to 0$ the Bessel functions diverge, while in the other end, as $\xi \to \infty$, they vanish. Significant contributions to the angular and spectral distribution are therefore obtained when ξ is small, and so we should for a

moment confine attention to this parameter, which in the high energy limit ($\gamma \gg 1$) can be approximated as

$$\xi \approx \frac{\omega}{2\omega_c}\gamma^3\psi^3. \tag{2.53}$$

At a particular frequency $\omega \ll \omega_c$ we can determine the spread of the angular distribution by defining the critical angle ψ_c, at which the value of $\mathrm{d}^2P/\mathrm{d}\omega\mathrm{d}\Omega$ is negligible, to be the angle at which $\xi(\psi_c) = \xi(0) + 1 \approx 1$. Doing this we find

$$\psi_c = \frac{1}{\gamma}\left(\frac{2\omega_c}{\omega}\right)^{1/3}, \qquad \omega \ll \omega_c, \tag{2.54}$$

showing that at low frequencies, the width of the angular distribution increases and tends to flatten out the curve. We can also compare this width to the width of the full angular distribution (2.40), which was found to be $\psi_c = \gamma^{-1}$, and see that (2.54) is wider than this in the low frequency limit.

In the high frequency limit ($\omega \gg \omega_c$) we can asymptotically expand the Bessel functions, and utilizing $\gamma \gg 1$ as well as that the angular distribution is confined to a small region around $\psi = 0$, we get the approximate expression

$$\frac{\mathrm{d}^2P}{\mathrm{d}\omega\mathrm{d}\Omega} \approx \frac{3e^2\beta^2\gamma^2\omega_B}{64\pi^2\epsilon_0 c}\,\frac{1+2\gamma^2\psi^2}{\sqrt{1+\gamma^2\psi^2}}\,\frac{\omega}{\omega_c}e^{-2\xi}. \tag{2.55}$$

Defining the critical angle ψ_c to be the $1/e$-point of the distribution, we obtain

$$\psi_c \approx \frac{1}{\gamma}\sqrt{\frac{2\omega_c}{3\omega}}, \qquad \omega \gg \omega_c. \tag{2.56}$$

As in the low frequency limit, we see that in the high frequency limit, the width of angular distribution decreases as the frequency increases. Compared with the full angular distribution case, the width of the angular distribution in the high frequency limit is smaller than the width in the full angular distribution.

It can be interesting to get a sense of at what frequencies typical populations of runaway electrons are expected to emit most of their radiation. In the Alcator C-Mod tokamak [27], which has a major radius of $R_m = 68\,\mathrm{cm}$ and magnetic field strength varying between 3-8 T on the low- and high-field sides respectively, the most prominent runaway electrons* are observed to have energies around 30 MeV and pitch angles around 0.15 rad [35]. The formula (2.49) thus suggest that such electrons would emit at critical wavelength $\lambda_c \equiv 2\pi c/\omega_c$ between 1.7-4.6 µm, depending on which side of the tokamak they're observed. While most of the radiation from such a population of runaways will be emitted in the near-infrared region, the asymptotic expansion at high frequencies Eq. (2.52) suggests that a significant amount of radiation will be emitted in the visible range, allowing the use of regular visible light cameras for synchrotron measurements.

Assuming a visible-light camera is used for synchrotron measurements, formula (2.56) gives the angular spread of the radiation in that case. With the same Alcator C-Mod parameters as above, we find that the approximate lateral size of the radiation cone, where it intersects the detector, is given by the device major radius

*The runaway electrons dominating the synchrotron spectrum and images.

times the critical angle, $R_\mathrm{m}\psi_\mathrm{c} \approx 68/\gamma\sqrt{3} \approx 6.5\,\mathrm{mm}$, which can be compared to the camera aperture which is circular with a radius of 3 mm. In Chapter 3 a simplified model of synchrotron radiation will be introduced, and the accuracy of that model will be shown to depend on the parameter $R_\mathrm{m}\psi_\mathrm{c}$.

2.3.4 Synchrotron spectrum and total emitted power

The angular and spectral distribution (2.51) can be integrated over all observation angles to yield an expression for the synchrotron spectrum [36]

$$\frac{\mathrm{d}P}{\mathrm{d}\omega} = \frac{\sqrt{3}e^2\gamma\gamma_\parallel\omega_B}{8\pi^2\epsilon_0 c}\frac{\omega}{\omega_\mathrm{c}}\int_{\omega/\omega_\mathrm{c}}^{\infty} K_{5/3}(x)\mathrm{d}x. \tag{2.57}$$

The peak of the spectrum is located close to ω_c as given by Eq. (2.49), and to make the dependence on energy, pitch angle and magnetic field strength clearer, we write

$$\omega_\mathrm{c} \approx \frac{3e}{2m}\left(\frac{E}{mc^2}\right)^2 B\sin\theta_\mathrm{p}. \tag{2.58}$$

The location of the peak of the spectrum thus scales linearly with magnetic field and pitch angle (at small θ_p), while scaling quadratically with the particle's energy. In tokamak experiments such as DIII-D [37], EAST [38] and TEXTOR [19], the critical frequency ω_c of the synchrotron radiation detected from runaway electrons corresponds to near infrared frequencies, while in Alcator C-Mod [35], which has a strong magnetic field, ω_c is observed to be near, or even in, the visible light range.

Using the asymptotic expansions in Eq. (2.52), we expand the spectrum in the limits of low and high frequencies, and obtain

$$\begin{aligned}
\frac{\mathrm{d}P}{\mathrm{d}\omega} &\approx \frac{\sqrt{3}\Gamma(2/3)e^2\gamma\gamma_\parallel\omega_B}{2^{7/3}\pi^2\epsilon_0 c}\left(\frac{\omega}{\omega_\mathrm{c}}\right)^{1/3}, && \omega \ll \omega_\mathrm{c},\\
\frac{\mathrm{d}P}{\mathrm{d}\omega} &\approx \frac{\sqrt{3}e^2\gamma\gamma_\parallel\omega_B}{2^{7/2}\pi^{3/2}\epsilon_0 c}\left(\frac{\omega}{\omega_\mathrm{c}}\right)^{1/2} e^{-\omega/\omega_\mathrm{c}}, && \omega \gg \omega_\mathrm{c}.
\end{aligned} \tag{2.59}$$

In both limits the spectrum decreases, but at different rates, as illustrated in Fig. 2.7. At low frequencies, the decrease is quite slow and proportional to $\omega^{1/3}$, giving significant contributions even at frequencies well below ω_c. In the other limit however, the decrease is exponential, giving a steep decline in the spectrum at high frequencies. When observing synchrotron radiation from this end of the spectrum, even small variations in energy, pitch angle or magnetic field can have dramatic effects on the amount of radiation observed.

We can also integrate either of the angular and/or spectral distributions over all angles and/or frequencies to obtain the total received power

$$P = \frac{e^4B^2\gamma^2\gamma_\parallel^2}{6\pi\epsilon_0 m^2 c}\beta_\perp^2. \tag{2.60}$$

While (2.60) at first glance appears to depend on the pitch angle, the dependence in $\gamma_\parallel^2 \approx 1/\sin^2\theta_\mathrm{p}$ on the pitch angle essentially cancels that in $\beta_\perp^2 = \beta^2\sin^2\theta_\mathrm{p}$. The power received from an electron in helical motion is thus independent of its pitch angle, while the power emitted by the electron does show a pitch angle dependence due to the absence of the $\gamma_\parallel^2$ in the electron frame (as discussed in Sec. 2.3.2).

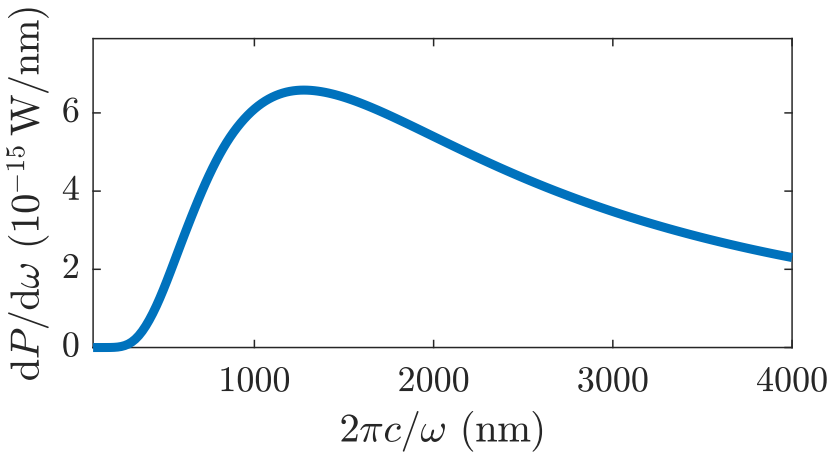

Figure 2.7: Example spectrum of the synchrotron radiation emitted by a 30 MeV runaway electron with pitch angle 0.13 rad in a homogeneous 5.25 T magnetic field.

2.3.5 Effect of cyclotron motion

The formulas derived in this chapter are valid in a homogeneous (referred to as "cylindrical" in the following) magnetic field. In tokamak plasmas however, the magnetic field is bent into a torus to prevent particle losses, and so the circulation around the tokamak will cause additional radiation to be emitted. Since runaway electrons are often characterized by $p_\parallel \gg p_\perp$, it is reasonable to imagine that this additional radiation could have a noticeable, or even substantial, effect on the emitted radiation. To address this question, in 1999 Pankratov derived an expression for the spectrum emitted by a runaway electron, taking both the gyro-motion, cyclotron motion and orbit drifts into account [39]. While the full expression obtained is computationally very heavy to evaluate, it is useful to evaluate in order to estimate the error made when neglecting the motion around the tokamak. It was shown that these effects are important when the quantity

$$\eta = \frac{\langle v_\perp \rangle}{v_{\mathrm{dr}}} = \frac{eBR_{\mathrm{m}}\langle v_\perp \rangle}{\gamma m \langle v_\parallel \rangle^2}, \tag{2.61}$$

is neither too small, nor too large, where $\langle \cdots \rangle$ denotes a gyro-average, v_{dr} is approximately the orbit drift speed and R_{m} is the tokamak major radius. The assumption that cyclotron motion is negligible is equivalent to $\eta \gg 1$, and so we should expect the formulas presented in this chapter to be valid if

$$587 \cdot \frac{B}{1\,\mathrm{Tesla}} \cdot \frac{R_{\mathrm{m}}}{1\,\mathrm{m}} \gtrsim \frac{\gamma}{\theta_{\mathrm{p}}}. \tag{2.62}$$

In Chapter 4 we will consider an Alcator C-Mod scenario, for which typical runaway parameters are $\gamma \sim 60$ and $\theta_{\mathrm{p}} \sim 0.15$. The major radius of the device is $R_{\mathrm{m}} = 68\,\mathrm{cm}$, and in the particular scenario considered in Chapter 4, $B_0 \approx 5.25\,\mathrm{T}$ (on the magnetic axis). These parameters give $\eta \approx 5$, which although not too large, should allow for the use of the cylindrical formulas.

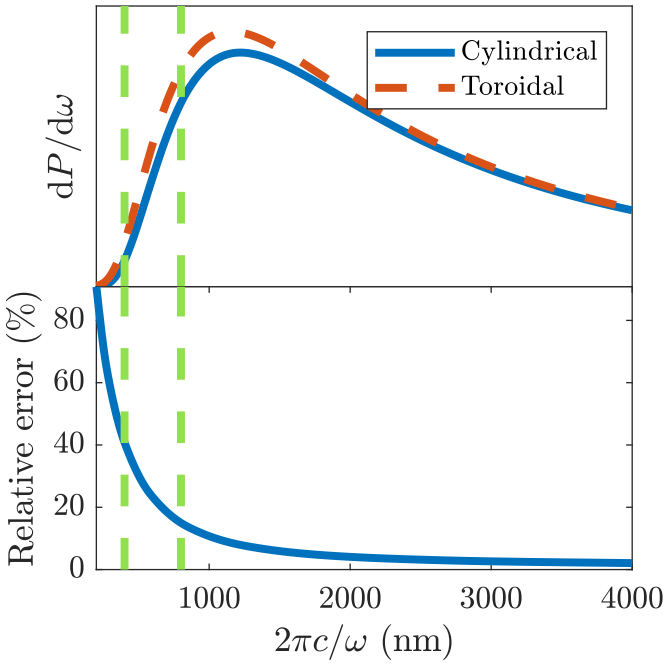

Figure 2.8: Plots of the synchrotron spectra (upper plot) in a cylindrical (solid) and toroidal (dashed) geometry with Alcator C-Mod-like parameters ($E = 30\,\mathrm{MeV}$, $\theta_\mathrm{p} = 0.13\,\mathrm{rad}$, $B = 5.25\,\mathrm{T}$), as well as the relative difference between the two curves (lower plot). The dotted green lines mark the visible range of the camera under consideration. The relative error made when using the cylindrical formula is between 15-40% in the visible range ($\lambda \in [400, 800]\,\mathrm{nm}$).

To further convince ourselves of the validity of the cylindrical formulas, we can compare the spectra given by the cylindrical and toroidal formulas for the Alcator C-Mod scenario. This is done in Fig. 2.8, where the spectra appear to show only a small difference near the critical frequency. In the visible range ($\lambda \in [400, 800]\,\mathrm{nm}$), which is used for synchrotron imaging in Alcator C-Mod, the relative error made when using the cylindrical formula is between 15-40%. The most important contributions to the image, however, originate from the long wavelength tail of the spectrum, which contributes in regions of high-magnetic field, and which shows a significantly smaller error of only a few percent. In Alcator C-Mod at least, the cylindrical formulas should therefore be valid when studying synchrotron spots.

3

A synthetic synchrotron diagnostic

In tokamak experiments, visible light and IR cameras are used to produce images of the synchrotron radiation appearing in the presence of runaway electrons. With the formulas derived in Section 2.3, it is possible to numerically compute the image that such a camera would see, given the phase-space distribution of runaway electrons. As a part of this project, the synthetic synchrotron diagnostic SOFT (for *Synchrotron-detecting Orbit Following Toolkit*) was developed, which utilizes the theory described in Chapter 2 and simulates a synchrotron camera in a tokamak. SOFT also implements a simpler, and more efficient scheme for producing the synchrotron image, which we refer to as the "cone model". In this chapter we will introduce the numerical tool SOFT and derive and motivate the use of the cone model of synchrotron radiation.

3.1 Fundamentals of synchrotron diagnostics

A sufficiently complete synthetic camera* must satisfy a number of more or less obvious conditions. First, it must behave like a camera, i.e. all detected radiation must come from within the camera's field-of-view, and must enter the camera aperture. Second, the orbit physics of particles must be modeled properly so that geometric effects are correctly taken into account. Third, the distribution of energies and pitch angles among electrons must be handled. Our approach here will be to derive a continuous description of the synchrotron image which can then be discretized and implemented. For a more complete treatment of this theory, see the SOFT documentation [40].

Constraining attention to radiation emitted in a small frequency interval $\mathrm{d}\omega$ onto a camera with aperture $\mathrm{d}A$ that is facing in the direction $\hat{\boldsymbol{n}}$, the quantity measured by a synchrotron camera is the power emitted in the wavelength range to which the camera is sensitive,reaching any given point $\boldsymbol{x}_0$ on the camera, along a line-of-sight in the direction $\boldsymbol{n}$. The power reaching the camera in a small frequency range $\mathrm{d}\omega$ within a region $\mathrm{d}A$ on the detector from a *particle*, is given by integrating the contributions along a given line-of-sight over all of phase-space:

$$\frac{\mathrm{d}^2 P_0(\boldsymbol{x}_0, \boldsymbol{n}, \omega, t)}{\mathrm{d}\omega \mathrm{d}A} = \int \mathrm{d}\boldsymbol{x}\mathrm{d}\boldsymbol{p}\, \frac{(\hat{\boldsymbol{n}} \cdot \boldsymbol{n})}{r^2} f(\boldsymbol{x}, \boldsymbol{p}, t - r/c)\delta\left(\frac{\boldsymbol{r}}{r} - \boldsymbol{n}\right) \frac{\mathrm{d}^2 P(\boldsymbol{x}, \boldsymbol{p}, \boldsymbol{x}_0, \omega)}{\mathrm{d}\omega \mathrm{d}\Omega}, \tag{3.1}$$

*While this section, and this thesis in general, only treats synthetic *synchrotron images*, the arguments given here are applicable to any form of radiation emitted by any charged particle in a tokamak plasma.

where $r = |\boldsymbol{r}| = |\boldsymbol{x} - \boldsymbol{x}_0|$ is the vector extending from the camera to the guiding-center, $f(\boldsymbol{x}, \boldsymbol{p}, t - r/c)$ is the number of particles in the point $\boldsymbol{x}$ with momentum $\boldsymbol{p}$ at time $t - r/c$, $\hat{\boldsymbol{n}}$ denotes the normal vector of the detector plane (i.e. the plane in which the camera aperture lies), and $\mathrm{d}^2P/\mathrm{d}\omega\mathrm{d}\Omega$ is the angular and spectral distribution of radiation received from the particle for the radiation type of interest. The purpose of the delta function is to ensure that only radiation directed along the given line-of-sight contributes to the total.

Since the electrons are confined by a magnetic field, their distribution in the poloidal plane can be determined solely from their equations of motion, when collisions, electric-field acceleration and radiation losses (which all happen on timescales that are much longer than the orbit transit time) are neglected. From Liouville's theorem [41] it then follows that if the density of particles in a particular point $(\boldsymbol{x}_1, \boldsymbol{p}_1)$ of phase-space is $f(\boldsymbol{x}_1, \boldsymbol{p}_1) \equiv f_1$, then the density of particles in any other point along the associated phase-space path is also f_1. In a toroidally symmetric magnetic field it is therefore sufficient to specify the distribution function on a straight line extending from the magnetic axis, and the typical line we choose is the one at $z = 0$ in the outwards radial direction (which is also the case for SOFT), in which case the distribution function is said to be given "in the outer midplane". Since the magnetic field varies over one poloidal orbit, it is important to be clear and consistent about where the distribution function is given.

To take the magnetic field geometry into account, we will want to trace all orbits in the device and obtain the distribution of particles in the poloidal plane. As mentioned in Sec. 2.1 however, it is numerically more efficient to follow the orbit of a particle's guiding-center instead of resolving the full particle orbit, and so we should consider making a change of coordinates. Choosing as our coordinates the guiding-center position $\boldsymbol{X}$, the gyro-phase ζ, and momentum $p_\parallel$ and $p_\perp$, we obtain an integral similar to (3.1), but with particle and guiding-center differentials related through [42]

$$\mathrm{d}\boldsymbol{x}\mathrm{d}\boldsymbol{p} \approx p_\perp \mathrm{d}\boldsymbol{X}\mathrm{d}\zeta\mathrm{d}p_\parallel\mathrm{d}p_\perp, \tag{3.2}$$

where the Larmor radius ρ was assumed to be much smaller than the typical length scales of the system. We make the same assumption for the vector $\boldsymbol{r} = \boldsymbol{x} - \boldsymbol{x}_0$, so that $\boldsymbol{r} \approx \boldsymbol{X} - \boldsymbol{x}_0$ and expression (3.1) in terms of the guiding-center quantities:

$$\begin{aligned} \frac{\mathrm{d}^2P_0(\boldsymbol{x}_0, \boldsymbol{n}, \omega, t)}{\mathrm{d}\omega\mathrm{d}A} &= \int \mathrm{d}\boldsymbol{X}\mathrm{d}p_\parallel\mathrm{d}p_\perp\, p_\perp \times \\ \times \frac{(\hat{\boldsymbol{n}}\cdot\boldsymbol{n})}{r^2}\delta\left(\frac{\boldsymbol{r}}{r} - \boldsymbol{n}\right) f_{\mathrm{gc}}(\boldsymbol{X}, p_\parallel, p_\perp, t - r/c) &\left\langle \frac{\mathrm{d}^2P(\boldsymbol{X}, p_\parallel, p_\perp, \boldsymbol{x}_0, \omega)}{\mathrm{d}\omega\mathrm{d}\Omega} \right\rangle. \end{aligned} \tag{3.3}$$

The notation $\langle \cdots \rangle$ here indicates a gyro-average, as introduced in Eq. (2.34). The electron distribution function has also been replaced with the electron guiding-center distribution function $f_{\mathrm{gc}}(\boldsymbol{X}, p_\parallel, p_\perp, t) = 2\pi f(\boldsymbol{X}, p_\parallel, p_\perp, t) \approx 2\pi f(\boldsymbol{x}, p_\parallel, p_\perp, t - r/c)$, where the gyrotropy [13] of f was used to remove the dependence on ζ and obtain a factor of 2π. Additionally, we assumed that the time of propagation of the emitted radiation, r/c, is much smaller than the time it takes for the distribution function to change, since this assumption is also necessary for the magnetic geometry to have an impact on the population.

In this guiding-center formulation of the problem, a more useful parametrization of the orbit can be introduced, which incorporates geometric effects of the magnetic field. The parametrization consists of the initial major radius ρ at which the electron begins its orbit, a parameter τ corresponding to the time at which the particle visits a given point along the orbit, and the toroidal angle ϕ. The transformation between these "trajectory" coordinates and the regular guiding-center coordinates is non-trivial and involves solving the guiding-center equations of motion, which is the reason for building the synthetic diagnostic SOFT around an orbit following code. The benefit of using these coordinates is however major, since Liouville's theorem causes the distribution function to be independent of the orbit time τ, in addition to the independence of the toroidal angle ϕ due to the axisymmetry of the tokamak.

As an intermediate step, we transform the Cartesian guiding-center coordinates (x, y, z) to the cylindrical guiding-center coordinates (R, ϕ, z). The differential element simply becomes $\mathrm{d}\boldsymbol{x} = R\mathrm{d}R\mathrm{d}\phi\mathrm{d}z$. Then a change of coordinates from the cylindrical guiding-center coordinates to the trajectory coordinates ρ, τ, ϕ leads to

$$\begin{aligned}\frac{\mathrm{d}^2 P_0(\boldsymbol{x}_0, \boldsymbol{n}, \omega, t)}{\mathrm{d}\omega \mathrm{d}A} &= \int \mathrm{d}\rho \mathrm{d}p_\parallel \mathrm{d}p_\perp \, p_\perp f_{\mathrm{gc}}(\rho, p_\parallel, p_\perp, t) \times \\ &\times \mathrm{d}\tau R(\rho, \tau) \mathrm{d}\phi \frac{\boldsymbol{n} \cdot \hat{\boldsymbol{n}}}{r^2} \left[J\delta\left(\frac{\boldsymbol{r}}{r} - \boldsymbol{n}\right) \frac{\mathrm{d}^2 P(\boldsymbol{X}, p_\parallel, p_\perp, \omega)}{\mathrm{d}\omega \mathrm{d}\Omega} \right],\end{aligned} \tag{3.4}$$

where the determinant J of the Jacobian matrix, connecting the cylindrical coordinates (R, z) and trajectory coordinates (ρ, τ), were introduced. As discussed above, because of Liouville's theorem the distribution function in this parametrization remains constant to changes in the parameters τ and ϕ, and so the distribution function specified in Eq. (3.4) is just the density of particles in the outer midplane.

To discretize Eq. (3.4) we let I_{ij} denote the power contained in pixel (i, j) of the synchrotron image. The power contributing to the pixel is a sum of all the power reaching any point of the detector along the line-of-sights corresponding to pixel (i, j) in the frequency range visible to the camera, so we must also integrate over the detector surface and the camera's spectral range. In the continuous description of the image we then have

$$\begin{aligned}I_{ij}(\boldsymbol{x}_0, t) &= \int p_\perp \mathrm{d}p_\parallel \mathrm{d}p_\perp \int \mathrm{d}\rho \mathrm{d}\tau \mathrm{d}\phi \int \mathrm{d}\omega \int \mathrm{d}A \times \\ &\times \frac{\boldsymbol{r} \cdot \hat{\boldsymbol{n}}}{r^3} \Theta_{ij}\left(\frac{\boldsymbol{r}}{r}\right) f_{\mathrm{gc}}(\rho, p_\perp, p_\parallel, t) \frac{\mathrm{d}^2 P(\boldsymbol{X}, p_\parallel, p_\perp, \omega)}{\mathrm{d}\omega \mathrm{d}\Omega},\end{aligned} \tag{3.5}$$

where $\Theta(\boldsymbol{r}/r)$ is a box function that is one if $\boldsymbol{r}/r$ is within the pixel with index (i, j) and zero otherwise, defined through

$$\frac{\boldsymbol{r} \cdot \hat{\boldsymbol{n}}}{r^3} \Theta_{ij}\left(\frac{\boldsymbol{r}}{r}\right) = \int_{\boldsymbol{N}_{ij}} \frac{\boldsymbol{n} \cdot \hat{\boldsymbol{n}}}{r^2} \delta\left(\frac{\boldsymbol{r}}{r} - \boldsymbol{n}\right) \mathrm{d}\boldsymbol{n}, \tag{3.6}$$

and $\boldsymbol{N}_{ij}$ is the set containing all lines-of-sights contributing to pixel (i, j).

Discretization of the integrals is carried out using a trapezoidal rule on a non-uniform grid [43], except for the integral over lines-of-sights $\boldsymbol{n}$, which due to the delta function can be handled in a different and more efficient manner. Instead of querying all possible lines-of-sight in order to find the one directed along $\boldsymbol{r}$, the

integration set $\boldsymbol{N}_{ij}$ containing $\boldsymbol{r}/r$ can be computed, which gives the indices of the pixel to which the particle will contribute. The integrals over ω and Ω are taken over the interval of observable frequencies and the solid angle taken up by the camera, respectively.

The integral over all particle orbits, parametrized by ρ, τ and ϕ, is carried out by solving the guiding-center equations of motion for each value of ρ and τ using a Runge-Kutta solver [44]. Since the tokamak is toroidally symmetric, the particle dynamics are independent of the toroidal angle at which we choose to solve the guiding-center equations of motion, and thus only depends on the particle's location in a poloidal plane. The integral over toroidal angle ϕ can thus be carried out for each value of ρ and τ without solving the equations again. If the assumption of toroidal symmetry becomes unjustified, due to for example significant magnetic ripple effects [45] or non-axisymmetric massive material injection during disruptions [46], the guiding-center equations of motion would also have to be solved in each initial toroidal point.

The independence of the distribution function on many of the quantities integrated over in (3.5) allows the expression to be separated into a geometric part and a runaway distribution part. The geometric part is given by

$$\hat{I}_{ij}(\rho, p_\parallel, p_\perp, \boldsymbol{x}_0) = \int \mathrm{d}\tau \mathrm{d}\phi \int_{\boldsymbol{N}_{ij}} \mathrm{d}\boldsymbol{n} \int \mathrm{d}\omega \int \frac{(\boldsymbol{n}\cdot\hat{\boldsymbol{n}})\mathrm{d}A}{r^2} \delta\left(\frac{\boldsymbol{r}}{r} - \boldsymbol{n}\right) \frac{\mathrm{d}^2 P(\boldsymbol{X}, p_\parallel, p_\perp, \omega)}{\mathrm{d}\omega \mathrm{d}\Omega}, \tag{3.7}$$

while the "distribution part" is simply the distribution function $f_{\mathrm{gc}}(\rho, p_\parallel, p_\perp, t)$. The quantity $\hat{I}_{ij}(\rho, p_\parallel, p_\perp, \boldsymbol{x}_0)$ can be seen as a Green's function that is independent of the runaway population in consideration, and that connects a runaway population to the synchrotron image it generates. By pre-computing $\hat{I}_{ij}(\rho, p_\parallel, p_\perp, \boldsymbol{x}_0)$, the image can quickly be computed for an arbitrary distribution function $f_{\mathrm{gc}}(\rho, p_\parallel, p_\perp, t)$ by carrying out the integral

$$I_{ij}(\boldsymbol{x}_0) = \int \mathrm{d}\rho \mathrm{d}p_\parallel \mathrm{d}p_\perp \, p_\perp f(\rho, p_\parallel, p_\perp) \hat{I}_{ij}(\rho, p_\parallel, p_\perp, \boldsymbol{x}_0), \tag{3.8}$$

which, in its discretized form, becomes a multiplication between two three-dimensional arrays.

3.2 Cone model of synchrotron radiation

In Section 2.3 it was shown that the guiding-center will emit synchrotron radiation in the shape of a cone with lateral width $\sim 1/\gamma$, and since a characteristic of runaway electrons is their highly relativistic energies, we expect the lateral width of the cone to be very thin at moderate distances from the emitter. The typical width of radiation reaching a synchrotron camera with aperture a in a device of major radius R_{m} can be estimated as $R_{\mathrm{m}}\psi_{\mathrm{c}}$, where ψ_{c} is the average critical angle, or angular spread, of the radiation observed by the camera. It is evident that if $R_{\mathrm{m}}\psi_{\mathrm{c}} \ll a$, the power emitted can be approximated as

$$\frac{\mathrm{d}P}{\mathrm{d}\omega \mathrm{d}\Omega} = \frac{1}{2\pi} \delta\left(\cos\mu - \cos\theta_{\mathrm{p}}\right) \frac{\mathrm{d}P}{\mathrm{d}\omega}, \tag{3.9}$$

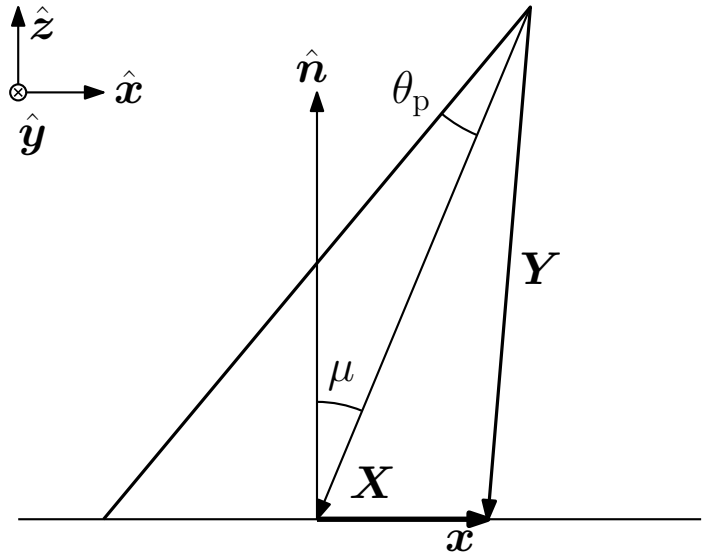

Figure 3.1: The radiation cone, with opening angle θ_{p} and axis along the vector $\boldsymbol{X}$ going from the guiding-center to the detector plane along the guiding-center velocity vector $\boldsymbol{V}$, is incident on the detector plane. The cone axis makes an angle μ with the detector plane normal $\boldsymbol{n}$. The vector $\boldsymbol{x}$ extends from the intersection point between $\boldsymbol{X}$ and the camera plane, and $\boldsymbol{Y} = \boldsymbol{X} + \boldsymbol{x}$ stretches from the guiding-center to the detector plane along the conic surface.

where $\mathrm{d}P/\mathrm{d}\omega$ is given by Eq. (2.57). Instead of directly integrating (3.9) over the detector surface, as one would typically do with an angular distribution of radiation, we can utilize the fact that (3.9) is a conic surface and consider the classical geometric problem of finding the intersection between a conic surface and a plane. The total power from a particle contributing to the image is then given by the length of the projected curve that overlaps the detector. The main motivation for introducing the cone model is that it should allow us to solve the integral over the detector surface analytically, thus avoiding a potentially heavy numeric integration.

The key assumption made in the cone model, that $R_{\mathrm{m}}\psi_{\mathrm{c}} \ll a$, turns out to not necessarily be as strict as it immediately appears. As we will see in Section 3.3, the synchrotron spots obtained from the cone model are in good agreement with the synchrotron spots obtained from the full angular distributions of radiation even though $R_{\mathrm{m}}\psi_{\mathrm{c}} \sim a$, and the cone model successfully captures key features of the images. For the cone model, the camera size can also be adjusted in order to approximately account for the finite size of the emitted cone and improve agreement with the full angular distribution model.

3.2.1 Intersection equation

Consider a conic surface incident on a plane as shown in Fig. 3.1, with the cone's axis making an angle μ with the normal $\boldsymbol{n}$ of the camera plane. It is evident that the vector $\boldsymbol{Y}$, defined as stretching from the guiding-center to the detector plane

along the conic surface, must satisfy the equation

$$\frac{\boldsymbol{X} \cdot \boldsymbol{Y}}{|\boldsymbol{X}||\boldsymbol{Y}|} = \cos\theta_{\mathrm{p}}. \tag{3.10}$$

Furthermore, we can write $\boldsymbol{Y} = \boldsymbol{x} + \boldsymbol{X}$, and by defining $\boldsymbol{x} = x\hat{\boldsymbol{x}} + y\hat{\boldsymbol{y}}$ and $\boldsymbol{X} = -X(\hat{\boldsymbol{x}}\sin\mu + \hat{\boldsymbol{z}}\cos\mu)$, Eq. (3.10) becomes

$$\frac{X - x\sin\mu}{\sqrt{X^2 + x^2 + y^2 - 2xX\sin\mu}} = \cos\theta_{\mathrm{p}}. \tag{3.11}$$

By squaring both sides and dividing by $\cos^2\theta_{\mathrm{p}}$ we obtain the intersection equation

$$\frac{(x - x_0)^2}{a^2} + \frac{y^2}{b^2} = 1, \tag{3.12}$$

with

$$\begin{aligned} a &= \frac{\cos\theta_{\mathrm{p}}\sin\theta_{\mathrm{p}}}{\cos^2\theta_{\mathrm{p}} - \sin^2\mu} X\cos\mu, \\ b &= \frac{\sin\theta_{\mathrm{p}}}{\sqrt{\cos^2\theta_{\mathrm{p}} - \sin^2\mu}} X\cos\mu, \\ x_0 &= \frac{-\sin^2\theta_{\mathrm{p}}}{\cos^2\theta_{\mathrm{p}} - \sin^2\mu} X\sin\mu. \end{aligned} \tag{3.13}$$

3.2.2 Solutions to the intersection equations

The intersection equation (3.12) is, for real a and b, known as the ellipse equation and describes an ellipse centered in the point $(x_0, 0)$ with semi-axes a and b. It is however evident from the definitions (3.13) that when $\cos\theta_{\mathrm{p}} < \sin\mu$ the coefficient b becomes imaginary, causing the relative sign between the two terms on the LHS of (3.12) to flip, thus instead describing a hyperbola. In the special case when $\cos\theta_{\mathrm{p}} = \sin\mu$ the intersection equation (3.12) can be shown to reduce to a simple parabolic equation.

We are interested in finding the points t_1, t_2, etc. at which the curve described by (3.12) intersects the detector, which is modeled as a square. To do this we first introduce a parametrization of the curve, and in the case when b is real it can be compactly written as

$$\begin{cases} x(t) = x_0 + a\cos t, \\ y(t) = b\sin t. \end{cases} \tag{3.14}$$

When b is imaginary we simply replace $\cos t \to \cosh t$, $\sin t \to \sinh t$ and redefine $b \equiv \operatorname{Im} b$ to obtain a hyperbolic parametrization instead. The parabolic case can be safely ignored since numerically we expect $\cos\theta_{\mathrm{p}}$ to never exactly equal $\sin\mu$. The coordinate system used in deriving (3.12) was such that $\boldsymbol{X}$ had no component along the $\hat{\boldsymbol{y}}$ axis, and so the detector could be rotated arbitrarily in the plane. In the following it will be more useful to have the detector aligned with our coordinate system axes, which requires us to rotate the parametrization (3.14) by the angle ξ

by which the detector and the projected curve differ. Similarly, origo was previously located in the point of intersection between $\boldsymbol{X}$ and the detector plane, but it will now prove more useful to move it to the center of the detector. By introducing x_{hit} and y_{hit} as the offsets between the new origo and the center of the projected curve, the full parametrization can be written

$$\begin{cases} x(t) &= -x_0 \cos\xi + x_{\text{hit}} + a\cos t\cos\xi + b\sin t\sin\xi, \\ y(t) &= x_0 \sin\xi + y_{\text{hit}} - a\cos t\sin\xi + b\sin t\cos\xi. \end{cases} \tag{3.15}$$

As before we can replace $\cos t \to \cosh t$, $\sin t \to \sinh t$ and $b \to \operatorname{Im} b$, if b is imaginary, to obtain a parametrization of a hyperbola instead. The equations we wish to solve then take the forms

$$\begin{aligned} x(t) \pm r_{\text{det}}/2 = 0, \quad |y(t)| < r_{\text{det}}/2, \\ y(t) \pm r_{\text{det}}/2 = 0, \quad |x(t)| < r_{\text{det}}/2, \end{aligned} \tag{3.16}$$

where r_{det} is the detector aperture. In the elliptic case, the solutions to Eqs. (3.16) are respectively

$$\begin{aligned} t_x &= 2\arctan\left(\frac{b\sin\xi \pm \sqrt{a^2\cos^2\xi + b^2\sin^2\xi - d_x^2}}{d_x + a\cos\xi}\right), \\ t_y &= 2\arctan\left(\frac{b\cos\xi \pm \sqrt{a^2\sin^2\xi + b^2\cos^2\xi - d_y^2}}{d_y - a\sin\xi}\right), \end{aligned} \tag{3.17}$$

where

$$\begin{aligned} d_x &= x - x_0\cos\xi + x_{\text{hit}}, \\ d_y &= y + x_0\sin\xi + y_{\text{hit}}. \end{aligned} \tag{3.18}$$

Similarly, in the case of a hyperbola, we obtain the solutions

$$\begin{aligned} t_x &= \log\left|\frac{d_x \mp \sqrt{d_x^2 + b^2\sin^2\xi - a^2\cos^2\xi}}{a\cos\xi + b\sin\xi}\right|, \\ t_y &= \log\left|\frac{d_y \mp \sqrt{d_y^2 + b^2\cos^2\xi - a^2\sin^2\xi}}{b\cos\xi - a\sin\xi}\right|. \end{aligned} \tag{3.19}$$

Obtaining the total amount of radiation reaching the detector is then just a matter of determining the length of the segments overlapping the detector, and adding the contributions together. Note that the radiation is only uniformly distributed in a cross section of the radiation cone, and in general not along the curve projected on the detector plane. The intersection points t_1, t_2, etc. must therefore be mapped to the unit cone on which the length of the intersecting line segments can be determined.

3.3 Synchrotron radiation model comparison

The result of running SOFT for a 30 MeV population of electrons with pitch angles $\theta_{\text{p}} = 0.13\,\text{rad}$, in the Alcator C-Mod magnetic equilibrium from shot 1140403026,

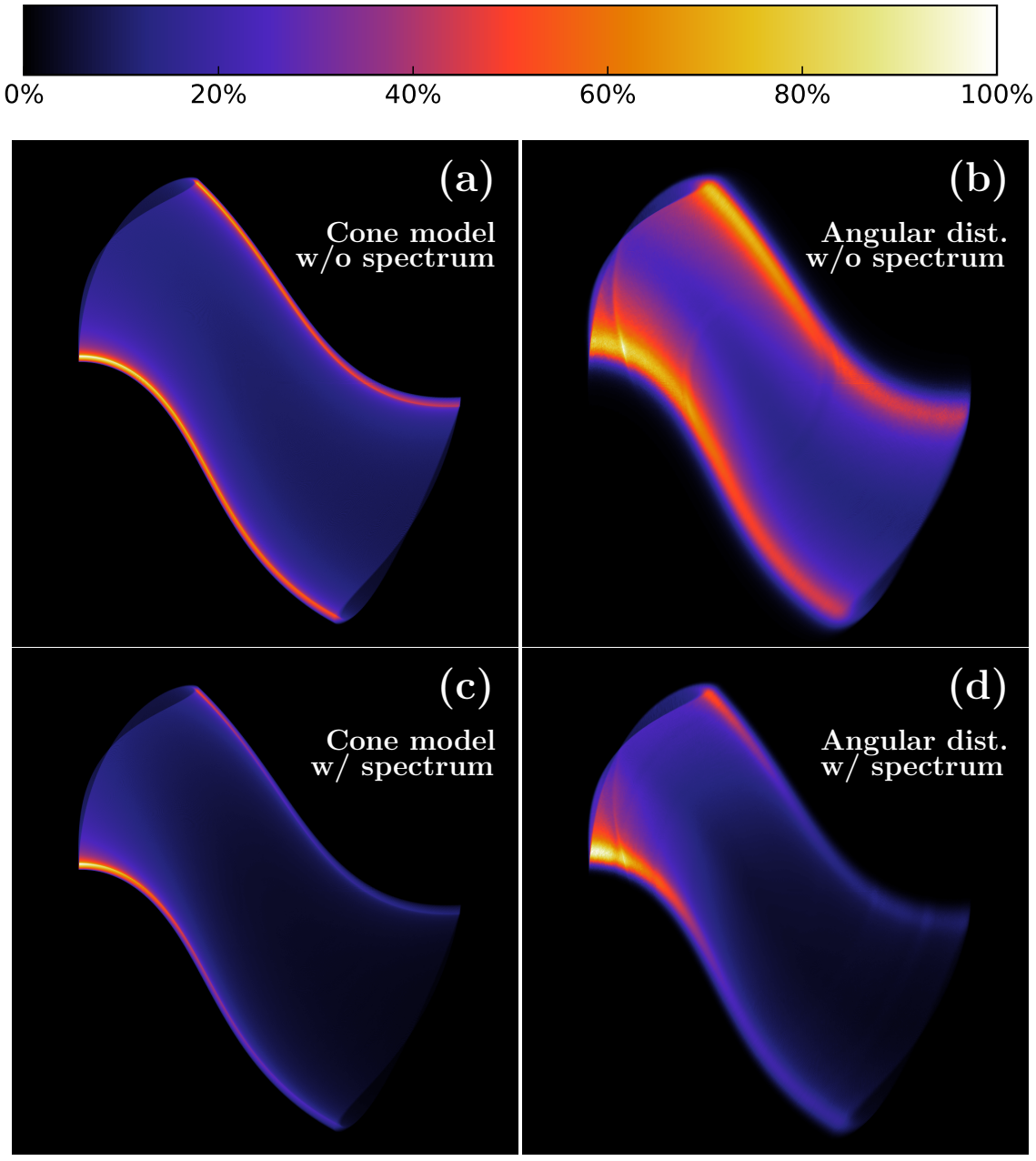

Figure 3.2: Comparison of the four synchrotron radiation models. The images were simulated with (a) the cone model without spectrum weighting, (b) the angular distribution Eq. (2.40), (c) the cone model with spectrum weighting, (d) the angular and spectral distribution Eq. (2.51). In (c) and (d), the wavelength interval considered was $\lambda \in [500, 1000]\,\mathrm{nm}$.

time $t \approx 0.742\,\mathrm{s}$, using each of the four models of synchrotron radiation (cone model with and without spectrum weighting, the angular distribution given by Eq. (2.40), and the angular and spectral distribution given by Eq. (2.51)) is shown in Fig. 3.2. The camera was located at $R = 106\,\mathrm{cm}$, $z = 0$ (midplane), looking tangentially at the plasma. The spot shapes obtained appear very similar in all four models, and the overall distribution of synchrotron radiation over the spot agrees well, particularly in the models (c) and (d) taking the limited spectral range into account. In the models taking the full angular distribution of radiation into account, (b) and (d), the upper and lower edges of the synchrotron spots show significantly broader bands of brightness than in the cone model. This effect can be traced to the finite cone width of the angular distribution models, and the cause of the slightly thinner bright edges in the angular and spectral distribution model were touched upon in Section 2.3.3. There it was found that at frequencies $\omega \gg \omega_\mathrm{c}$ the critical angle (or width of the distribution) was given by

$$\psi_\mathrm{c} = \frac{1}{\gamma}\sqrt{\frac{2\omega_\mathrm{c}}{3\omega}}, \tag{3.20}$$

which is less than the γ^{-1} width found when integrating over all frequencies. For the test case considered in Fig. 3.2, $\omega \approx 5\omega_\mathrm{c}$ which means we should expect the radiation cone to be thinner, and the cone model to be more accurate, when we take the limited wavelength range into account, just as Fig. 3.2 shows. In Alcator C-Mod, our estimate for the cone width when only studying radiation from a limited spectral interval gives $R_\mathrm{m}\psi_\mathrm{c} \sim 6.5\,\mathrm{mm}$. The aperture of the detector modelled has a diameter of $a \approx 6\,\mathrm{mm}$, so the side of the cone of radiation approximately covers the detector when directed towards it. While the cone model may not seem well justified in this case, Fig. 3.2 shows that it still captures much of the detail obtained in the full model.

3.3.1 Improving accuracy of the cone model

The finite width of the synchrotron cone can be modeled in a rather simple, but ad-hoc way, by making the detector size larger. The guiding-center will contribute radiation to the final image as long as its radiation hits the camera, and in a simplified picture this is the case only for as long as the cone with lateral width $2\psi_\mathrm{c}$ overlaps the detector. In the cone model, the lateral width is infinitesimal, while in the angular distribution model it is finite, and so in the angular distribution model the electron will be seen in a slightly wider region of space. The same effect can be obtained by making the detector aperture wider, and by assuming that the distance between the camera and the particle is approximately constant over the whole synchrotron spot, we can estimate the "effective" detector aperture that should be used together with the cone model to more accurately simulate the synchrotron radiation.

A cone of lateral width $2\psi_\mathrm{c}$ will be seen even a distance $r\sin\psi_\mathrm{c}$ outside of the detector. Accounting for this on both sides of the detector, and assuming ψ_c to be small, we obtain

$$a' = a + 2r\psi_\mathrm{c}, \tag{3.21}$$

where a is the aperture size used in the angular distribution model, and a' is the effective aperture size that should be used in the cone model. What ψ_c to use

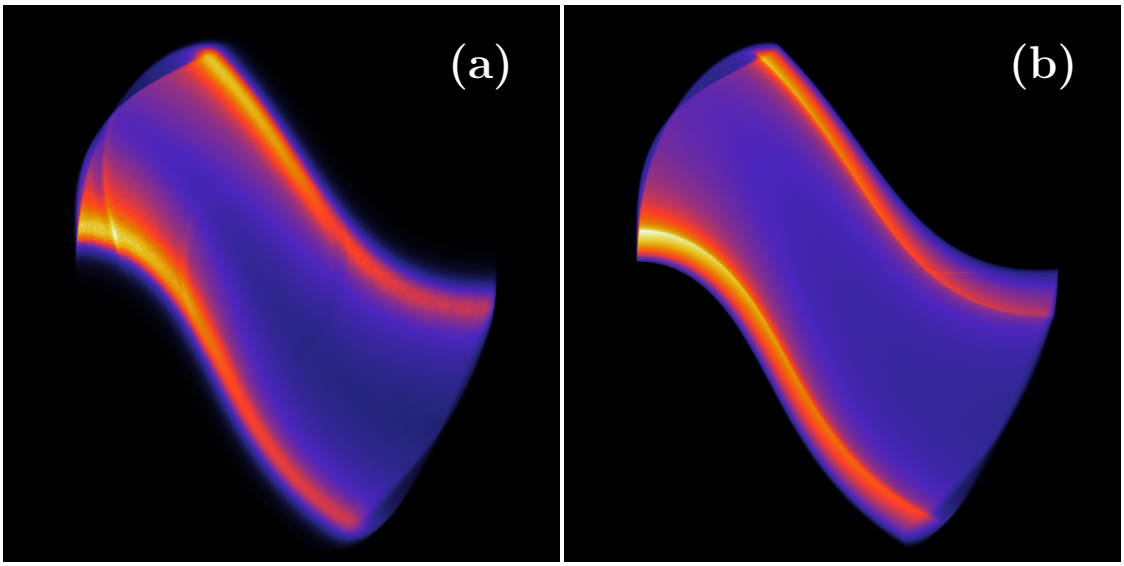

Figure 3.3: Example of how making the detector larger can compensate in the cone model for the infinitesimal width of the radiation cone. The figures show (a) the angular distribution model with camera aperture $a = 6\,\mathrm{mm}$, and (b) the cone model (without spectrum weighting) with aperture size $a' = a + 2r\gamma^{-1} \approx 27\,\mathrm{mm}$.

depends on the wavelength range under consideration. For $\omega \ll \omega_\mathrm{c}$, the critical angle (2.54) should be used, while for $\omega \gg \omega_\mathrm{c}$ the critical angle (2.56) should be used. When $\omega \approx \omega_\mathrm{c}$, or when the angular distribution in all wavelengths is considered, then γ^{-1} should be used as the critical angle. It is worth noting that these "required orderings" are not very strict, and that even relatively small differences between ω and ω_c would qualify for using the critical angle in either of the high- or low-frequency limits.

An example of this modification is shown in Fig. 3.3, where an image generated with the angular distribution model and camera aperture size $a = 6\,\mathrm{mm}$ is shown in (a), and an image generated with the cone model and camera aperture $a' = a + 2r\gamma^{-1} \approx 27\,\mathrm{mm}$ is shown in (b).

3.3.2 Numerical efficiency

Computationally, the cone model is much faster than the angular distribution models when $R_\mathrm{m}\psi_\mathrm{c} \ll a$, since use of the angular distribution models require the detailed numerical evaluation of a double integral over the detector surface, while the cone model replaces this integral with simple analytic expressions. Table 3.1 lists the order-of-magnitude run-times it took to generate each of the images in Fig. 3.2 on an Intel Core i5 CPU with 4 cores, each running at a clock speed of 3.2 GHz. In the angular distribution models, the detector surface was discretized on a 10-by-10 grid. All images were generated with all other parameters fixed (including resolution parameters). It is worth noting that while the difference is merely a factor of three in this case between the cone model and angular distribution, the efficiency of the cone model becomes more apparent as the size of phase-space increases, in which case computation times can differ by much larger factors.

Table 3.1: Order-of-magnitude comparisons of computation times for each of the synchrotron images in Fig. 3.2.

Model	**Computation time**
Cone model, without spectrum weighting	$\sim 10\,\mathrm{min}$
Cone model, with spectrum weighting	$\sim 10\,\mathrm{min}$
Angular distribution	$\sim 30\,\mathrm{min}$
Angular and spectral distribution	$\sim 100\,\mathrm{min}$

It is also worth noting that in the opposite limit $R_\mathrm{m}\psi_\mathrm{c} \gg a$, the intensity of radiation can be assumed constant over the surface of the detector, making the double integral trivial to evaluate. In this case, the full models can turn out to be faster than the cone model, since the angular distribution formulas are somewhat cheaper to evaluate once than determining the length of the overlapping ellipse segment in the cone model.

4

Synchrotron radiation images

All charged particles in a plasma will inevitably interact and allow the energy of the plasma to be distributed among its constituent particles, forming a continuous distribution in momentum space. From previous chapters we know that the synchrotron radiation emitted by an individual electron critically depends on the velocity of the electron, and in particular the electron's pitch angle. When the synchrotron image we see is the result of a continuous distribution of runaway electrons emitting into the camera, it is evident that the resulting image can be very complex, and that analytical methods are insufficient to reconstruct the image. However, the linearity of the image, i.e. the fact that an image due to a continuous distribution of runaways is a weighted sum of images of many individual electrons, allows some basic understanding of how certain properties of the runaway population affect the resulting image, and it is the aim of this chapter to give the reader this basic understanding. First, synchrotron radiation is compared to isotropically emitted radiation in order to adjust the reader to the peculiar nature of the former. The useful concept of a "surface-of-visibility" is introduced next along with its defining synchrotron spot equation, which will aid in the fundamental understanding of the synchrotron images presented later. To show how different properties of runaway electrons affect the observed synchrotron image, a number of parameter scans are then presented and interpreted. Finally, a scenario with a full momentum-space distribution function is presented and related to the parameter scans.

4.1 Interpretation of synchrotron images

As we saw in Section 2.3, the synchrotron radiation emitted by a runaway electron is narrowly peaked in the forward direction, in sharp contrast to how emission and reflection of light by all the objects we experience in everyday life works. While a beam of particles emitting isotropic radiation, as shown in Fig. 4.1a, is relatively easy to understand intuitively, the image obtained if the same beam of particles was to emit synchrotron radiation, which is shown in Fig. 4.1b, appears significantly more counter-intuitive and difficult to interpret. Aside from just being seen on one side of the tokamak, the synchrotron radiation is confined to a small spot, despite the fact that the particles are distributed in the beam. While in the case of isotropic radiation, all particles are visible to us (except for those blocked by walls), the case of synchrotron radiation puts a strict limit on in which points particles are actually able to emit towards the observer. With the help of the cone model presented in Sec. 3.2 we can put the above discussion in more mathematical terms and try to

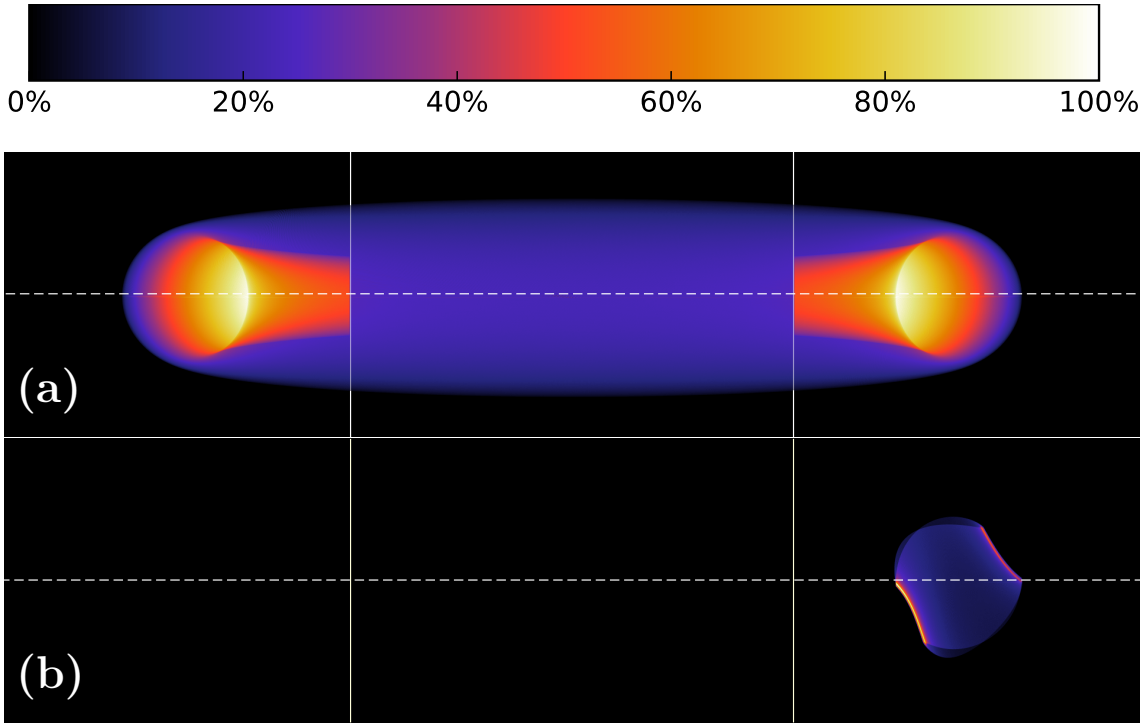

Figure 4.1: Example of particles emitting (a) isotropic radiation and (b) synchrotron radiation in a tokamak, seen from the midplane looking straight on to the midpole. The beam simulated was identical in the two cases, and the only difference was the way radiation was emitted. The solid white lines mark the edges of the midpole, and the dashed line marks the midplane.

understand what it is we actually see, as well as how we can make physically sensible interpretations of the synchrotron spot.

Consider for a moment a point camera, located at $\boldsymbol{R}_{\text{det}}$, and let $\hat{\boldsymbol{r}} = (\boldsymbol{x} - \boldsymbol{R}_{\text{det}})/|\boldsymbol{x} - \boldsymbol{R}_{\text{det}}|$ be the unit vector pointing from the camera in the direction of the arbitrary point $\boldsymbol{x}$. At the point $\boldsymbol{x}$, the magnetic field is directed along the unit vector $\hat{\boldsymbol{b}}(\boldsymbol{x})$, and since the electron's guiding-center approximately follows the magnetic field lines, its velocity vector is approximately directed along $\hat{\boldsymbol{b}}(\boldsymbol{x})$ as well. In the cone model, radiation will then only reach the detector when the guiding-center's velocity vector makes an angle θ_{p} with the vector $\hat{\boldsymbol{r}}$. The observed synchrotron spot must therefore satisfy the equation

$$\hat{\boldsymbol{b}}(\boldsymbol{x}) \cdot \hat{\boldsymbol{r}}(\boldsymbol{x}) = \cos\theta_{\text{p}}. \tag{4.1}$$

We expect Eq. (4.1) to usually be solved in two distinct points along a given line of sight $\hat{\boldsymbol{r}}$. The object observed in synchrotron measurements on runaway electrons can therefore be interpreted as "the surface on which such electrons are visible", which we will refer to as the *surface-of-visibility*. The importance of this realization must however not be overlooked, despite the apparent circular definition of the term, since this surface is very different from the usual "surface of visibility" we are familiar with. In our everyday world we are accustomed to looking at objects emitting (or reflecting) light in every direction, in stark contrast to the runaway electrons which only emit in their forward direction. Directly applying our intuition gained from everyday life is therefore not possible when analyzing synchrotron images and we need to be aware of what we are looking at. With this said, synchrotron images do have a lot to tell us (possibly even more than what we are used to, since the surface of visibility is also dependent on pitch angle) and if properly understood they could turn out to be powerful tools in diagnosing runaway electrons.

Further analysis of Eq. (4.1) reveals that when the camera is placed in the midplane of a typical tokamak, it describes a surface that can be described almost as a bent, hollow cylinder. As the camera sweeps vertically downwards from the midplane, the cylinder apparently opens up along its lower edge.

In Fig. 4.2, a top view of the tokamak can be seen, showing where in the device contributions to the synchrotron image come from. Contributions appear to arise from a narrow region in the xy-plane, extending almost orthogonally to the viewing direction of the camera. Note however, that because of the dependence in Eq. (4.1) on the camera location, a camera placed in the ceiling of the tokamak would not see the same surface-of-visibility as a camera located in the midplane.

4.2 Setup of a test case

There is a wide range of tokamaks under experimental operation today around the world, each with its own set of properties and characteristics, and a synchrotron image taken in one device will therefore, in general, appear very different from an image taken in another device. It is therefore impossible to create a benchmark scenario which is applicable to all existing machines, but if we choose the test-case parameters wisely we should at least be able to draw generally valid conclusions

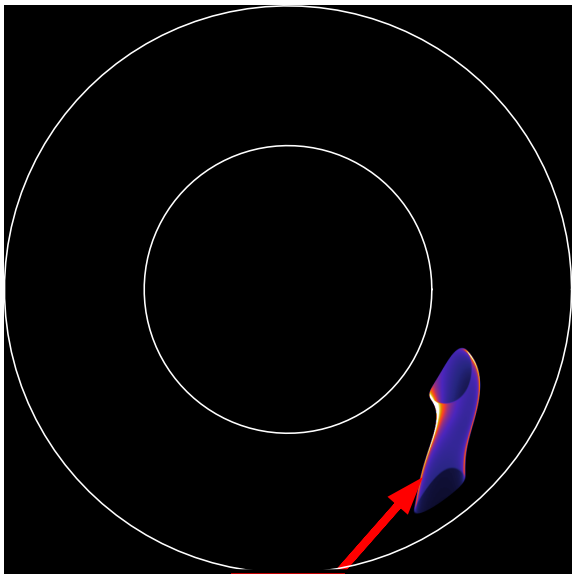

Figure 4.2: Topview of the tokamak, showing the extent of the *surface-of-visibility* in the xy-plane. The red arrow indicates the viewing direction of the camera. Note that this is a Cartesian plot, rather than a camera view, and that synchrotron contributions are line-integrated along the z-direction, rather than along the camera's line-of-sight as in the actual synchrotron images.

about the overall effect different parameters have on the observed synchrotron spot. For this purpose, we will in Section 4.3 confine attention to an Alcator C-Mod-like scenario for which experimental measurements are available. For computational efficiency, the cone model of synchrotron radiation will be used in all simulations.

In Fig. 4.3, poloidal projections of magnetic field lines of the magnetic equilibrium used are shown, and in Fig. 4.4 the placement and orientation of the camera in the horizontal plane is illustrated. The camera will be vertically aligned with the midplane since this is the only elevation at which we're guaranteed to be able to see particles at all radii (see Sec. 4.3.4). These specifications apply to all test cases, except of course for when the camera's vertical position is scanned in Section 4.3.4.

In Table 4.1, the fixed parameters used in all subsequent scans, unless otherwise specified, are shown. All parameters have been chosen to match approximately those estimated from experiments at the Alcator C-Mod tokamak. In the particular shot corresponding to the magnetic equilibrium used, synchrotron measurements were dominated by runaway electrons with energies of 30 MeV and pitch angles around 0.13 rad*. At those energies, the electrons emit mostly at wavelengths near $\lambda \approx 1.3\,\mu\text{m}$ (as shown in Fig. 4.5), but much radiation will also be emitted in the visible range. A simple visible-light camera can thus be used, which in the simulations is modeled by letting the camera be equally sensitive to all wavelengths between $\lambda = 500\,\text{nm}$ and $\lambda = 1000\,\text{nm}$. The magnetic field strength on-axis is

*This may seem to be in conflict with kinetic theory, which predicts that the runaway electron distribution is typically peaked at small values of θ_p. The observed peak is however the result of the total synchrotron emission scaling as $p_\perp^2$, so that the very numerous particles with small θ_p emit much less radiation than those with higher θ_p.

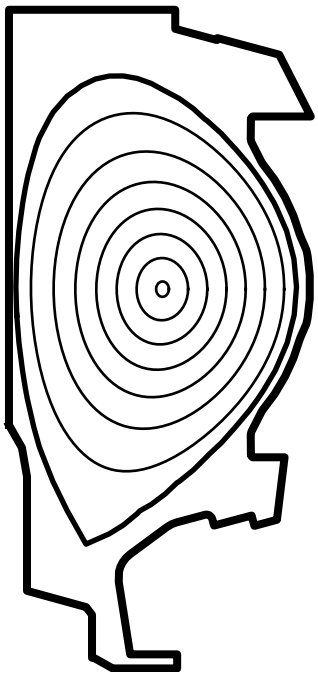

Figure 4.3: Alcator C-Mod-like magnetic equilibrium used in the simulations, with the outermost solid line representing the poloidal cross section of the tokamak wall. The inner solid lines mark the poloidal projections of different flux surfaces, and the point to which they converge is called the magnetic axis.

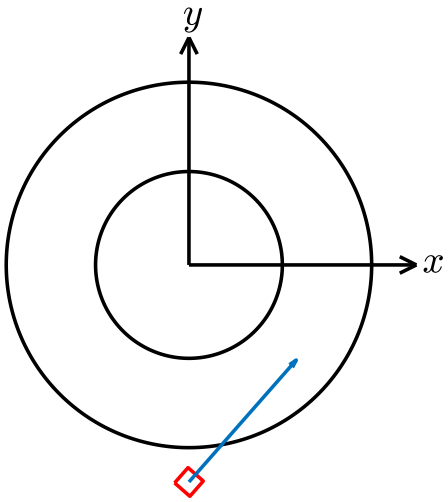

Figure 4.4: Tokamak top view, showing the camera configuration used for most simulations in Chapter 4. The camera is situated in $x = 0$, $y = -1.069\,\mathrm{m}$, viewing tangentially towards the plasma. Vertically, the camera is located in the midplane with no up-down tilt.

Table 4.1: Parameters used for the simulations in Chapter 4.

Parameter	Value
Camera spectral range	$\lambda \in [500, 1000]\,\mathrm{nm}$
Electron energy	$30\,\mathrm{MeV}$
Magnetic field strength (on axis)	$5.25\,\mathrm{T}$
Electron pitch angle	$0.13\,\mathrm{rad}$
Radial extent of runaway beam	$r \in [0, 16]\,\mathrm{cm}$

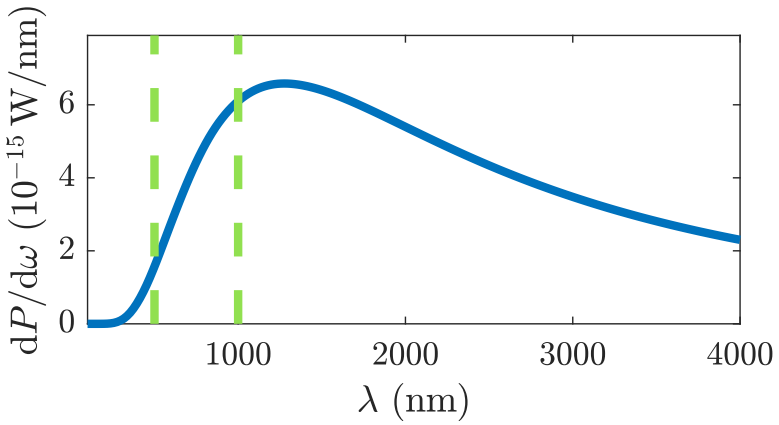

Figure 4.5: Spectrum emitted by a runaway electron with energy $E = 30\,\mathrm{MeV}$ and pitch angle $\theta_\mathrm{p} = 0.13\,\mathrm{rad}$ in a homogeneous magnetic field of strength $B = 5.25\,\mathrm{T}$. The green dashed lines indicate the camera's visible range.

$B_0 = 5.25\,\mathrm{T}$, and particles are placed from the magnetic axis ($r = 0$) and $14\,\mathrm{cm}$ outwards on the outboard side.

4.3 Variation of parameters

Probably the best way to get acquainted with an advanced simulation tool is to independently vary all input parameters in an attempt to discover their effect on the output. In this section, that approach will be taken in order to gain understanding for how different properties of the runaway population affect the observed synchrotron image. Since an actual synchrotron image is a weighted sum of such single-particle images, with the runaway distribution function acting as the weight, this approach should help in interpreting the more complicated synchrotron images obtained in experiments.

A synchrotron image taken in a particular tokamak can be considered as the output of a mathematical function taking five physical parameters as input. From the discussion in Section 3.1 we see that the only parameters not limited by the physics of the machine are

(i) Radial distribution of runaways.

(ii) Pitch angle distribution of runaways.

(iii) Energy distribution of runaways.

(iv) Vertical placement of camera.

(v) Proximity of camera to the runaway beam.

There are a few additional physical parameters which also have effects on the image, namely the magnetic equilibrium used, the size of the camera and the camera's field-of-view, all of which will not be studied specifically in this thesis. The dependence of the image on the magnetic equilibrium was studied extensively by Zhou *et al.* [47], and since our focus is towards the properties of the runaway electron population giving rise to the synchrotron spot, rather than the machine parameters, we will not study those effects and instead rely on their work when appropriate. The size of the camera affects the region within which electrons are visible and will cause a slightly more diffuse image, but for realistic camera apertures this effect is negligibly small. As for the camera field-of-view, this only affects which parts of space are included in the image, and it will not significantly affect the actual synchrotron spot except for the size it occupies in the image.

Throughout this chapter we will refer to so called *one-particle models*, which are useful for isolating features in the image. Essentially, this term refers to the shape of the momentum-space distribution of runaways, i.e. points (ii) and (iii) in the parameter list above, and indicates that both of them are simple delta functions. Effectively, this means that the runaway population exists in one point of momentum-space only, with all electrons possessing the same energy and pitch angle, and not that the image was the result of a single particle emitting synchrotron radiation as the name may seem to imply (the particles are still distributed in the poloidal, toroidal and gyro-angles).

All images in the following sections will be normalized to their own maximum values, in order to focus on relative intensity differences between different parts of the image, instead of absolute intensity differences between different images (which can vary significantly). The reason for this is to better understand where different features in a synchrotron image come from, since the number of particles of a particular momentum can drastically alter the absolute intensity difference between images.

Figure 4.6: Colorbar indicating the relative differences indicated by colors in all synthetic synchrotron images in this thesis.

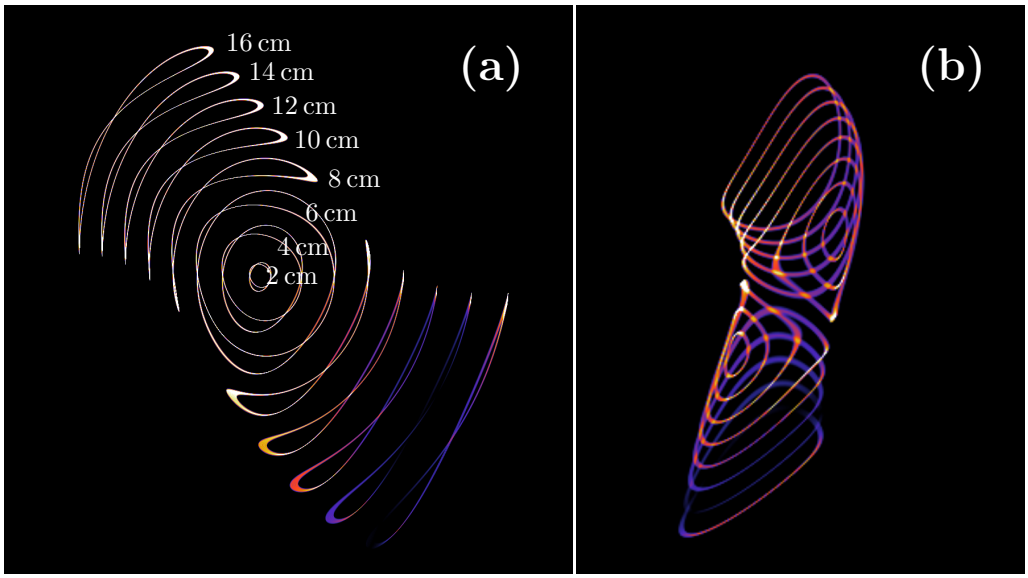

Figure 4.7: Contributions to the synchrotron image from individual radii. The left panel shows the synchrotron image and the right panel shows the corresponding topview map (cf. Fig. 4.2).

4.3.1 Radial distribution of particles

In the simulations giving the images of Fig. 4.7, electrons were initialized at eight distinct radii in order to discern what effect the initial radial coordinate of the particle has on the image. The innermost electron was dropped at major radius $R = 70\,\mathrm{cm}$, while the outermost electron was dropped at $R = 84\,\mathrm{cm}$, and the other electrons were spaced uniformly within this interval. All electrons were given an energy of $E = 30\,\mathrm{MeV}$ and initial pitch angle of $\theta_\mathrm{p} = 0.13\,\mathrm{rad}$.

Two types of curves can be identified in Fig. 4.7a. Near the center of the image, pairs of circles can be seen with one circle in each pair appearing to stand in front of the other. Further out we find oblong, closed bands of radiation, and here each band on the right side of the image arises together with a band on the left side of the image. Counting the curves we see that there are ten oblong bands and six circles of radiation, in other words twice as many curves as radii under consideration. It turns out, just as intuition leads us to believe, that each of the bands (or circles) of radiation can be shown to originate from electrons initiated at a single minor radius.

Electrons at large minor radii are seen for shorter periods of time while they're on the inner inboard and outer outboard sides of the tokamak – in between, the cone of radiation never intersects the camera and the electrons are invisible. As we move towards the magnetic axis the bands of synchrotron radiation on each side of the axis come together and transition into circular bands of radiation. Despite this transition where the synchrotron bands come together, there are always two distinct bands originating from the same minor radius, and in the transition from oblong bands to circles the bands change from originating from different sides of the poloidal plane (oblong bands), to originating from both sides of the poloidal plane, but two toroidal locations (circular bands).

A top view of the synchrotron spot, as shown in Fig. 4.7b, reveals the 3-D struc-

ture of the surface-of-visibility, and shows the extent of the synchrotron bands in the direction tangential to the camera viewing direction. As mentioned in Sec. 4.1, the surface-of-visibility appears to take on the shape of a bent cylinder. Figure 4.7b also reveals that the surface-of-visibility appears to be composed of two semi-symmetric parts, one made up of the oblong synchrotron bands on the inboard side as well as the "back" circular bands, while the other part is made up of the oblong synchrotron bands on the outboard side, as well as the "front" circular bands.

When a non-uniform radial distribution is used, Fig. 4.7a gives a strong hint about how the synchrotron spot will be affected. A peak in the radial distribution far from the magnetic axis would give rise to two bright bands in the synchrotron spot, extending from the top edge to the bottom edge on each side of the spot. A peak near the magnetic axis would instead result in a bright circle around the axis – the two distinct circles seen in Fig. 4.7 would likely be indistinguishable in experiment due to multiple effects, such as the radial distribution being of finite width and a spread in energy making the circles less sharp, among others.

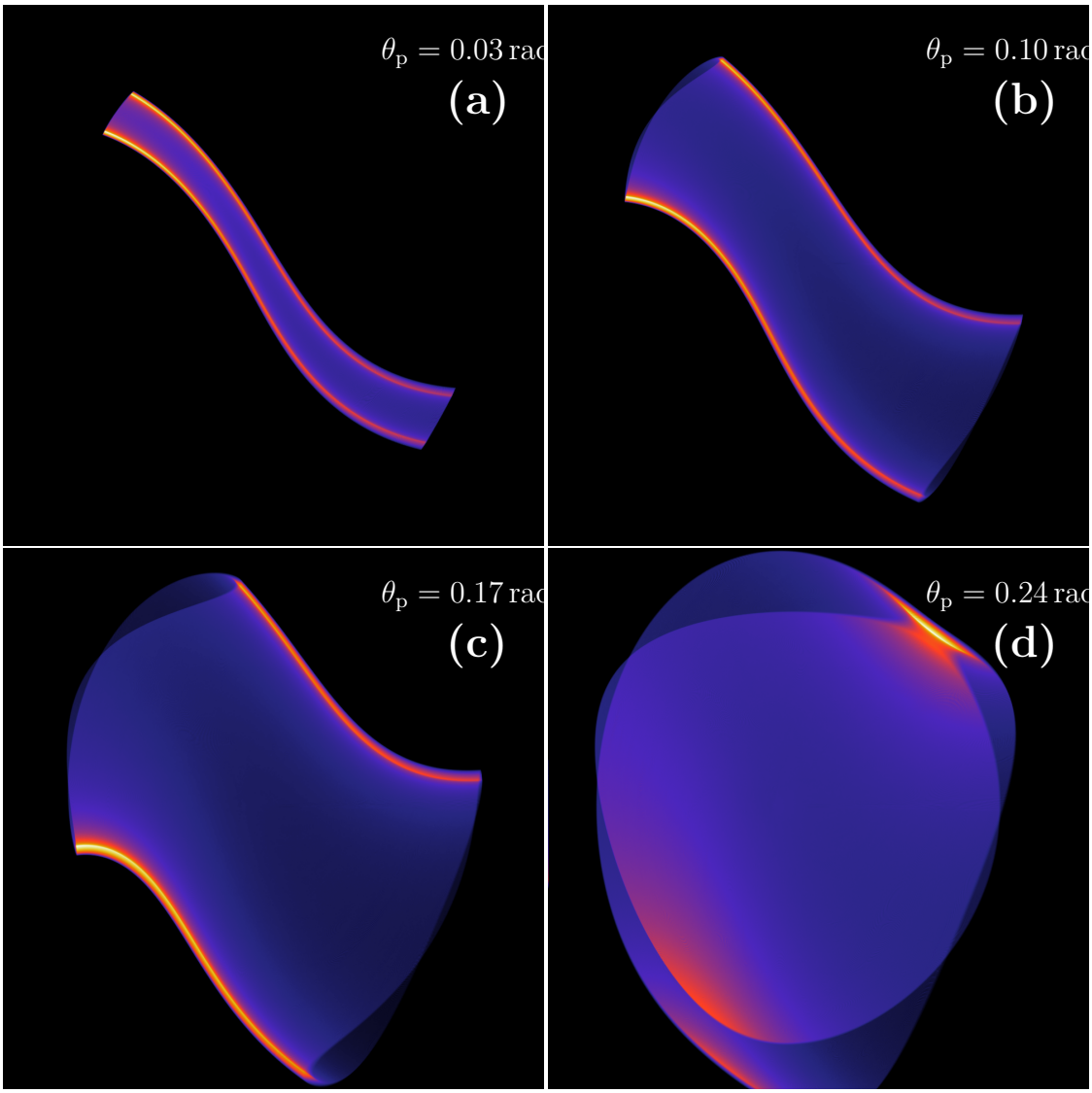

Figure 4.8: Variation of the pitch angle between (a) $\theta_p = 0.03\,\text{rad}$, (b) $\theta_p = 0.10\,\text{rad}$, (c) $\theta_p = 0.17\,\text{rad}$ and (d) $\theta_p = 0.24\,\text{rad}$.

4.3.2 Pitch angle

In Fig. 4.8 the value of the pitch angle of all the runaway electrons, defined as $\cos\theta_p = v_\parallel/v$, are varied between the different subfigures. In order from part (a) to part (d) the values of the pitch angles are $\theta_p = 0.03\,\text{rad}$, $\theta_p = 0.1\,\text{rad}$, $\theta_p = 0.17\,\text{rad}$ and $\theta_p = 0.24\,\text{rad}$. The pitch angles presented in Fig. 4.8 were selected based on what is predicted by kinetic theory to dominate the runaway distribution, and what pitch angles give the most distinct synchrotron spots. While larger pitch angles may be present in the runaway population, the synchrotron spot shape can be extrapolated from Fig. 4.8d and does not give rise to any radically new pattern.

The pitch angle determines the vertical size of the synchrotron spot, or – in terms of the surface-of-visibility – the radius of the cylinder-like surface that is the surface-of-visibility. As the pitch angle is increased its lower and upper edges opens up and splits into two distinct surfaces, one standing in front of the other.

The physics behind the synchrotron spot shape are due to the cone of synchrotron radiation emitted by the runaways. The opening angle of the cone is twice the pitch angle of the runaway electron, and thus the pitch angle directly influences in what regions of the tokamak radiation can be seen. By thinking of the radiation as an ellipse sweeping across the wall, with the pitch angle determining the semi-axes (the distance between the camera and the electron accounting for a minor part of the ellipse size), the increasing vertical extent of the synchrotron spot with increasing pitch angle can be intuitively understood. In the limit $\theta_\mathrm{p} \to 0$ the synchrotron cone tends towards a line emitted in the direction of guiding-center motion, and the electron can only be seen in a single point (assuming a point-camera).

As the pitch angle is increased, the ellipse will encircle a larger fraction of the wall, making it increasingly more likely for an electron to, at some point during its orbit, contribute to the camera image. The result is that electrons further away in altitude from the camera finally have an ellipse large enough to cover the camera, making them visible to the camera and causing the synchrotron spot to appear more extended in the vertical direction.

At larger pitch angles ($\theta_\mathrm{p} \gtrsim 0.2$ in Alcator C-Mod) the synchrotron spot transitions into two distinct, oval surfaces. The longer of the two surfaces, which can be identified as the "back" surface by looking at a top view map of the synchrotron image, tends to become even longer as the pitch angle is increased. The front surface on the other hand is moved closer and closer to the camera with increasing pitch angle, while the back surface slowly moves away from the camera. This can also be understood with the help of the cone model, since a particle with a large pitch angle will radiate almost at right angle with the magnetic field lines, and the two points along the electron orbit at which radiation hits the camera move further and further away from each other.

When the runaway population has a continuous distribution of pitch angles, the synchrotron image will be a weighted superposition of the images in Fig. 4.8. As shown in Sec. 2.3, the total synchrotron power emitted scales like $p_\perp^2$ and should therefore have a maximum for some non-zero pitch angle, which may be seen to dominate the synchrotron image. Pitch angles near the dominating one will however also contribute significantly to the image, and so the total image should have many familiar features of the single-pitch images in Fig. 4.8, but have broader, bright bands along the upper and lower edges. If the dominating pitch angle is sufficiently small the distribution of pitch angles would therefore give rise to bands of brightness tilted in one diagonal direction, while a radial distribution would give rise to vertical bands of radiation tilted in a perpendicular diagonal direction.

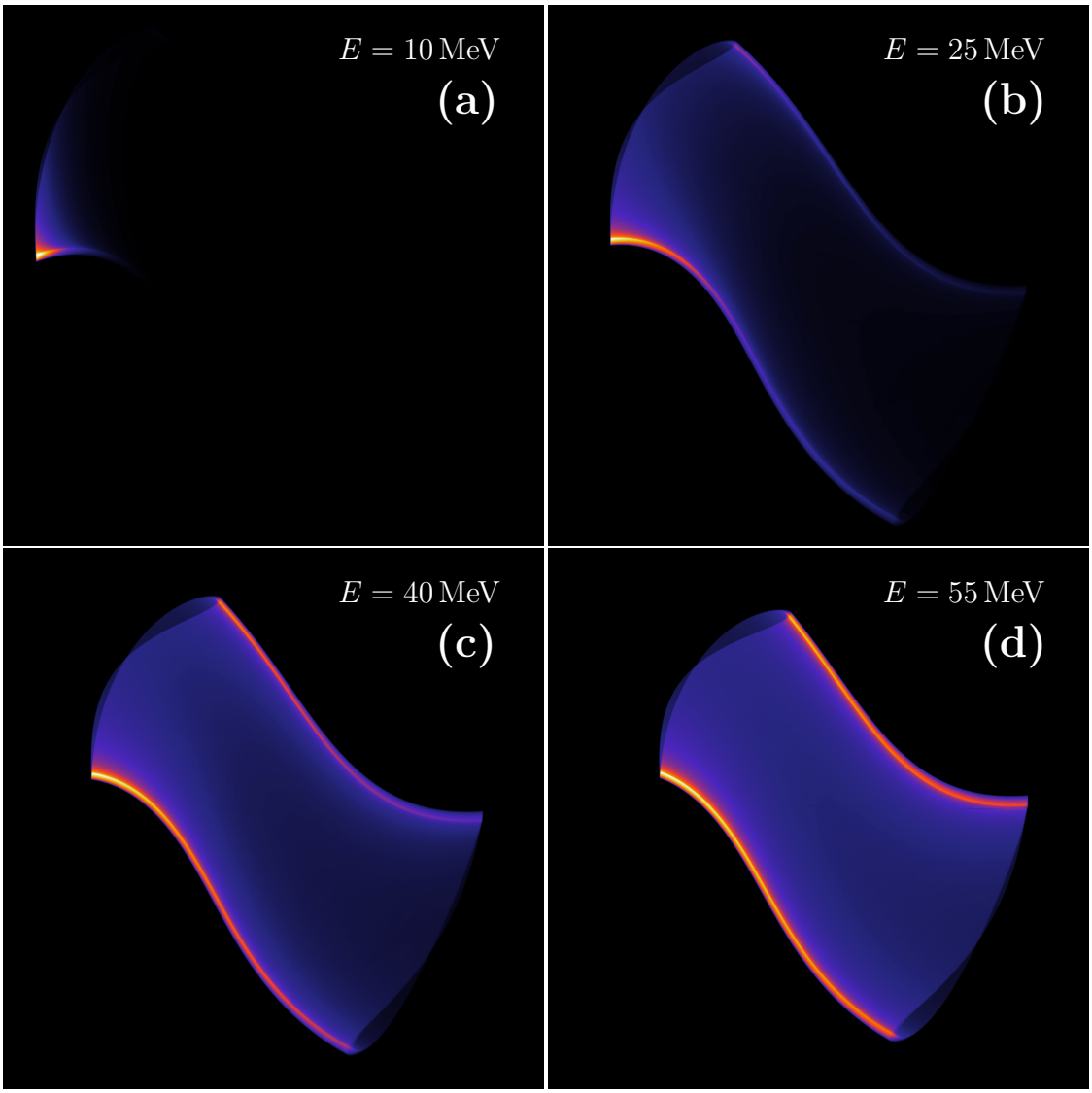

Figure 4.9: Synchrotron images for which the energy has been varied between the values (a) $E = 10\,\mathrm{MeV}$, (b) $E = 25\,\mathrm{MeV}$, (c) $E = 40\,\mathrm{MeV}$ and (d) $E = 55\,\mathrm{MeV}$.

4.3.3 Energy

In Fig. 4.9 the energy of all the runaway electrons has been varied between the four different subfigures. From part (a) to part (d) the energies shown are $E = 10\,\mathrm{MeV}$, $E = 25\,\mathrm{MeV}$, $E = 40\,\mathrm{MeV}$ and $E = 55\,\mathrm{MeV}$. Runaway electrons have been observed at many different energies in the Alcator C-Mod tokamak, but in the particular scenario considered in this text the runaways were estimated to reach energies of about 30 MeV.

The energy of the runaway population can be identified to have two distinct effects on the synchrotron spot. As is emphasized in the comparison of Fig. 4.9a with the others, the intensity peak gets shifted from the left of the image (the inboard side) towards the right of the image (the outboard side) as the electron energy is increased. As higher energies are reached we also begin to see a contraction of the synchrotron spot on the left side, in the horizontal direction, as is apparent by

comparing Figs. 4.9b-d. A third effect, that is not shown in Fig. 4.9 as intensities are normalized, is that the total intensity in the synchrotron spot increases with increasing energy.

The shifting of the intensity from the inboard towards the outboard side can be explained by comparing the synchrotron spectra corresponding to the images. In Fig. 4.10 the synchrotron spectra for the four different energies of Fig. 4.9 are shown, each normalized to its own peak power. At 10 MeV the peak is so far away from the camera's visual range that very little of the emitted radiation is seen by the detector. The only radiation that can be seen comes from the so called high-field side of the device, where the magnetic field is very strong. When $\omega \gg \omega_c$ we can use the asymptotic expansion of the angular and spectral distribution (2.59) to estimate how sensitive different parts the image will be to the varying parameters, and we see that

$$\frac{\mathrm{d}P}{\mathrm{d}\omega} \sim \exp\left(-\frac{1}{B\sin\theta_p}\right) \sim \exp\left(-R^{3/2}\right), \tag{4.2}$$

where the adiabatic invariance of $\mu = p_\perp^2/2mB$ was used to relate θ_p to B, and the magnetic field scales with major radius R approximately as $B \sim 1/R$. Thus, on the high-field side, the intensity seen by the detector will be boosted exponentially compared to the low-field side, which well accounts for the observed synchrotron spot in Fig. 4.9a. As the energy is increased, Fig. 4.9 shows how the peak of the synchrotron spectra gets pushed into the camera's visual range, and around $E = 40\,\mathrm{MeV}$ the spectrum peaks in the center of the visual range, making all of the synchrotron spot visible. At the highest energy, $E = 55\,\mathrm{MeV}$, the peak of the spectrum is in the ultraviolet range of wavelengths, and the asymptotic expansion of the spectrum (2.59) at small frequencies (large wavelengths) will scale as

$$\frac{\mathrm{d}P}{\mathrm{d}\omega} \sim \sqrt{R}. \tag{4.3}$$

In other words, at high energies the intensity distribution over the synchrotron spot is much less sensitive to the origin of the radiation than at low energies, which explains the nearly constant intensity observed in Figs. 4.9c & d.

At the higher energies the second effect, a contraction of the synchrotron spot on the left, becomes apparent. We can relate this effect to the radial location of electrons, and by comparison of this effect to Fig. 4.7 we see that electrons appear to not be present on the innermost radii at very high energies, while on the outboard side the horizontal extent is the same. This is due to drift orbit shifts [48], which perturbs the orbit in the way shown in Fig. 4.11. This effect also causes the synchrotron spot to move slightly towards the outboard side.

While the energy does not have a significant effect on the shape of the surface-of-visibility, it can have a strong effect on the observed synchrotron spot due to the energy dependence of the emitted spectrum, combined with the limited spectral range of the camera. The synchrotron spot shape can therefore be significantly altered by the energy of the runaway beam, if the electrons emit radiation at frequencies far from the camera's visual range. If the critical frequency ω_c is within the camera's visual range however, and if the camera's visual range is broad enough to see most of the radiation, the spectral dependence of the synchrotron spot can be ignored and the observed spot shape is only affected by energy through orbit drifts.

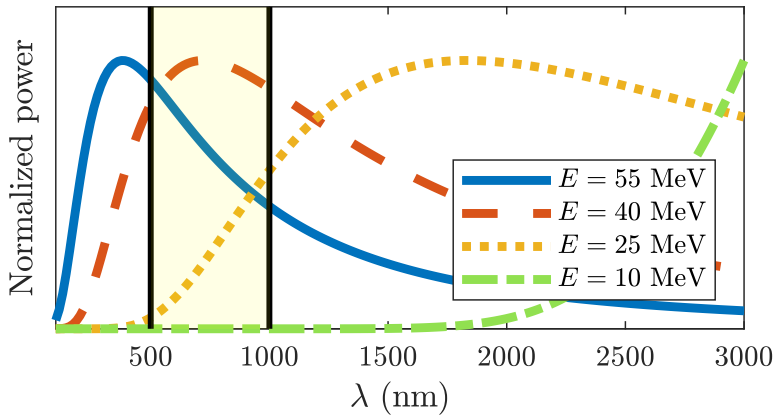

Figure 4.10: Synchrotron spectrum at four different energies, on the magnetic axis. The camera's spectral range has been marked with a shaded rectangle. To emphasize the locations of the spectrum peaks, all spectra have been normalized to their maximum values (within the interval $\lambda \in [100, 3000]$ nm).

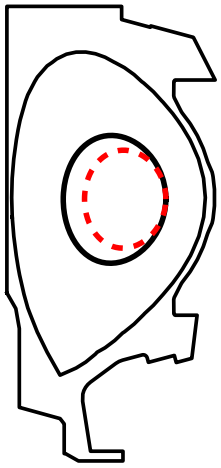

Figure 4.11: Example of how drifts affect the electron orbit in Alcator C-Mod. The black (solid) orbit is for an electron at $E = 10$ MeV, while the red (dashed) orbit is for an electron with $E = 55$ MeV. As can be seen, the drifts act by pushing the particle towards the outboard side of the device, and in this case where the electron is initiated in the outer midplane, the orbit appears to get compressed.

When the runaway population is distributed in energy, the effects of orbit drifts will be small and electron energies will not have a significant effect on the synchrotron spot, since the total emitted power also increases with energy, unless the spot is dominated by contributions from frequencies ω that are much different from the critical frequency. This means that the distribution of pitch angles among the electrons is more important in setting the spot shape, although the energy dependence may cause slightly stronger contributions to arise from parts of the synchrotron spot, such as from the inboard side when $\omega > \omega_c$. If ω is significantly different from ω_c, the effective pitch angle of the synchrotron spot will be strongly dependent on energy, and the same synchrotron spot, seen simultaneously through two cameras with different wavelength ranges, may look very different.

Orbit drifts are not expected to introduce any new dark or bright shapes on the synchrotron spot when the electron population has many different energies. The drift effects are significant only when the relative energy difference between two compared populations is large, something which is rarely the case for the electrons that are visible to the camera, and so the difference in the orbit shift between the highest and lowest visible energies will mostly be negligible. The drift orbits will however cause a contraction (or expansion, depending on the device parameters) of the overall shape of the synchrotron spot.

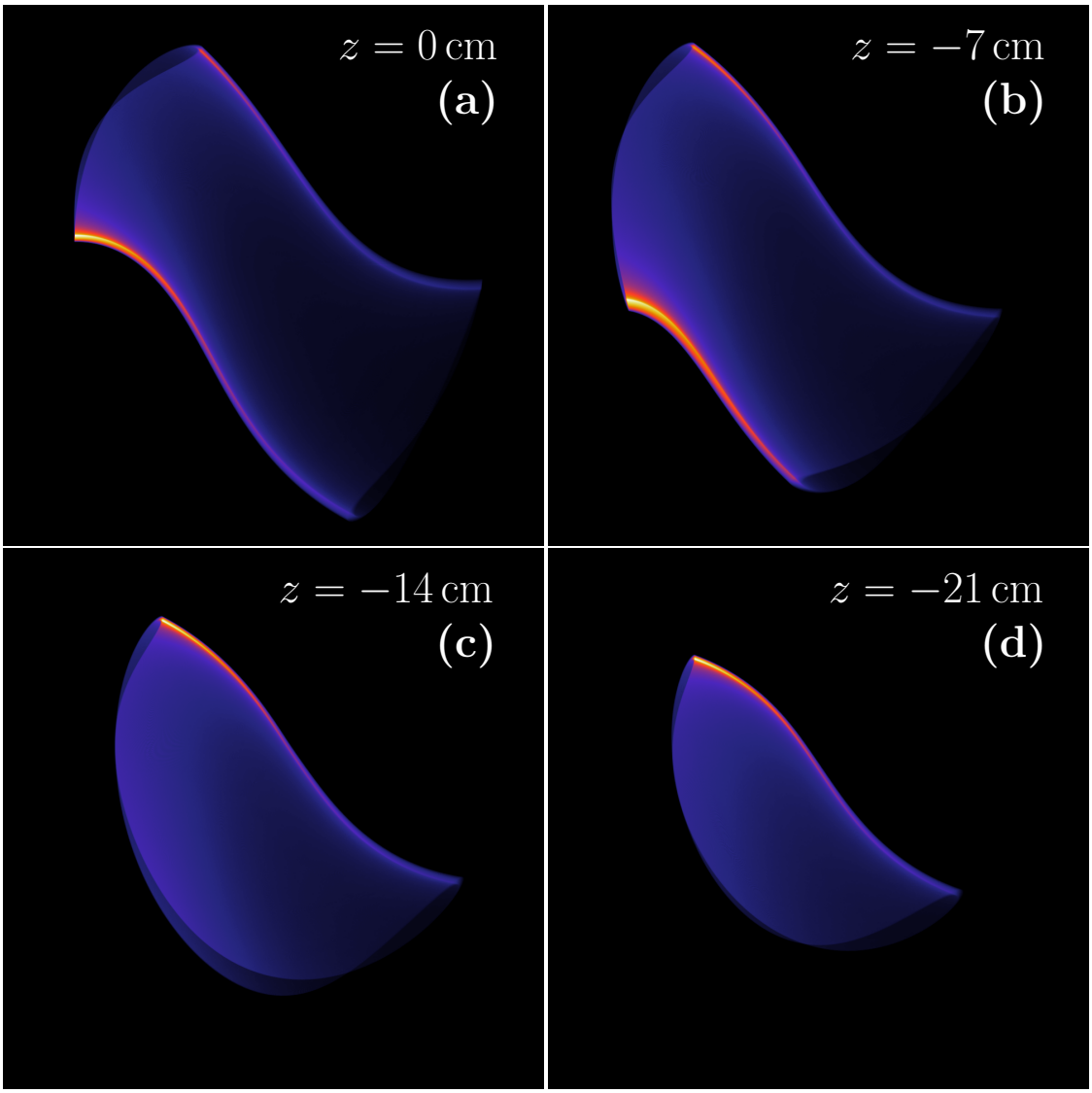

Figure 4.12: Images showing the effect of vertically moving the camera. The camera location is (a) $z = 0\,\mathrm{cm}$, (b) $z = -7\,\mathrm{cm}$, (c) $z = -14\,\mathrm{cm}$ and (d) $z = -21\,\mathrm{cm}$.

4.3.4 Vertical placement of camera

Figure 4.12 shows the effect of moving the camera vertically downwards from the midplane. In part (a) the camera is placed in the midplane ($z = 0$) with no tilting, in the other figures the camera is moved to (b) $z = -7\,\mathrm{cm}$, (c) $z = -14\,\mathrm{cm}$ and (d) $z = -21\,\mathrm{cm}$. The camera is also progressively tilted upwards as it is moved further down to maintain focus on the synchrotron spot. The lower limit on the camera placement in this example is motivated by the placement of one of the visible-light cameras in Alcator C-Mod, which is located at $z \approx -21\,\mathrm{cm}$.

When the camera is vertically aligned with the midplane, the synchrotron spot shows some symmetry between its upper-left and lower-right parts, and the surface-of-visibility is a twisted cylinder. As the camera is moved downwards, the lower edge of the spot contracts, and the surface-of-visibility appears to slowly open up along its lower edge. At $z = -14\,\mathrm{cm}$, the surface-of-visibility has completely opened

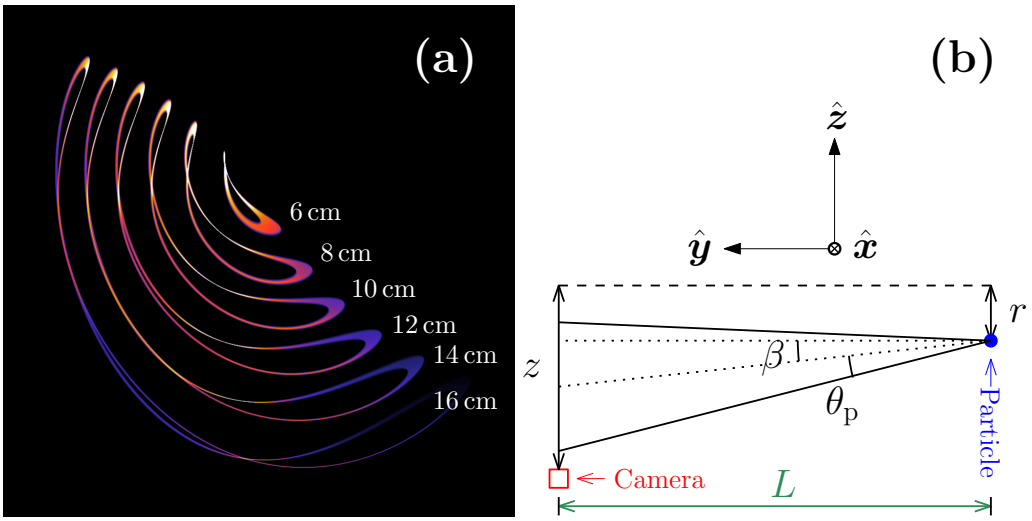

Figure 4.13: Part (a) shows contributions to the synchrotron image from different radii when the camera is located 21 cm below the midplane. Part (b) illustrates how the vertical displacement of the camera causes particles with small pitch angles to become invisible near the magnetic axis.

up at the lower edge and turned into a potato-chip form, and the bright lower edge of the spot, as could be seen at $z = 0$ and $z = -7\,\mathrm{cm}$, has now disappeared. When the camera finally reaches $z = -21\,\mathrm{cm}$, the spot has the same overall shape as at $z = -14\,\mathrm{cm}$, but has now become somewhat smaller than there.

We can get valuable insight into the shape of the synchrotron spot by looking at contributions to it from individual radii. Such an image is shown Fig. 4.13 with the radii from which each synchrotron band originates labeled. In Fig. 4.13, electrons were dropped every 2 cm from the magnetic axis, but we notice that the two innermost radii are invisible. We can make a crude estimate of the lower limit on the visible radii in this case with the help of Fig. 4.13b. With r denoting the minor radius at which the electron is located, R the major radius of the device, z the vertical displacement of the camera from the midplane, L the farthest distance between the camera and the electron, and β the angle between the poloidal and toroidal magnetic field components, related to q by $q = r\cot\beta/R$, we obtain

$$r \gtrsim \frac{z - L\tan\theta_\mathrm{p}}{1 + (L + z\tan\theta_\mathrm{p})/qR}. \tag{4.4}$$

With $z = 21\,\mathrm{cm}$, $\theta_\mathrm{p} = 0.13$, $L = 80\,\mathrm{cm}$, $R = 68\,\mathrm{cm}$ and $q = 1$, we get $r \gtrsim 4.8\,\mathrm{cm}$, which seems reasonable, since judging from Fig. 4.13 it should be between 4-6 cm.

For a population of runaway electrons with a distribution of pitch angles, this can have a significant impact on the observed synchrotron spot, since different parts of the image may be dominated by different pitch angles. While it can be misleading in a synchrotron image, it should not really prevent proper analysis of it. For a spectrometer however, which integrates away the spatial dependence of the synchrotron image, this effect can be of more importance as it would give an average spectrum which misses an unknown amount of radiation from small-pitch-angle particles.

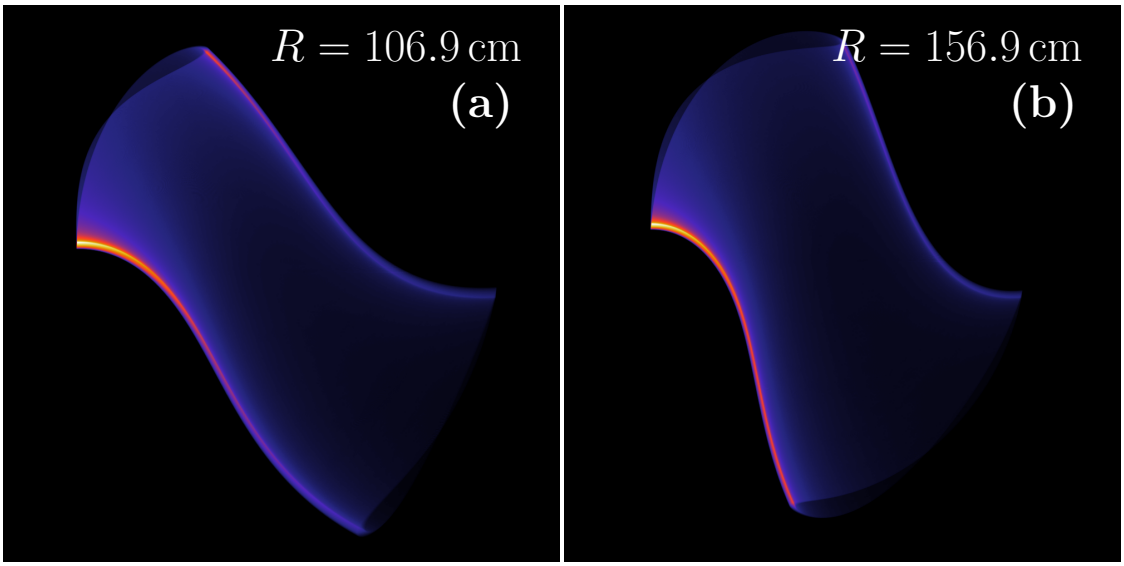

Figure 4.14: When the camera is moved away from the plasma along the viewing direction, the observed synchrotron spot appears to tilt and the width of the spot increases. The location of the camera in (a) is $R = 106.9\,\mathrm{cm}$ and in (b) $R \approx 151.8\,\mathrm{cm}$.

4.3.5 Proximity of camera to plasma

How close the camera is to the plasma makes a difference when studying synchrotron spots, and in Fig. 4.14 two different synchrotron images taken by cameras located at different distances from the plasma are shown. In part (a) the camera is located at the default position, $R = 106.9\,\mathrm{cm}$, while in part (b) it has been moved 50 cm backwards, along its viewing direction vector, corresponding to $R \approx 151.8\,\mathrm{cm}$.

While it is rare for a camera to be moved in this way in actual experiments, this simulation gives a hint about the difference of a synchrotron spot when similar runaway populations are observed in different machines. Of course, many other parameters come into play and will affect the synchrotron spot, but those parameters can often be comparable in devices of different size, while the actual device sizes differ by large factors. Since the proximity of the camera to the synchrotron spot will increase as the major radius of the device increases, this can be of greater importance when comparing synchrotron spots.

Two effects can be seen as the camera is moved away from the plasma in Fig. 4.14, both of which are related to the spot shape equation (4.1). The first effect is a tilting of the synchrotron spot, acting in a way so that the further away the camera gets, the more the synchrotron spot appears to be standing upright. The second effect observed is that the synchrotron spot appears to widen as the camera is moved further away. We can partly understand that the synchrotron spot shape changes with the help of Fig. 4.15 and by noting that as the camera is moved further away from the spot, its lines-of-sight will approach parallel lines, making new angles with the magnetic field in a given point.

More qualitative results can be obtained for the inclination, and this was done in Ref. [47]. By making a number of reasonable assumptions on the synchrotron spot, including an assumption of small pitch angle, the following relation between

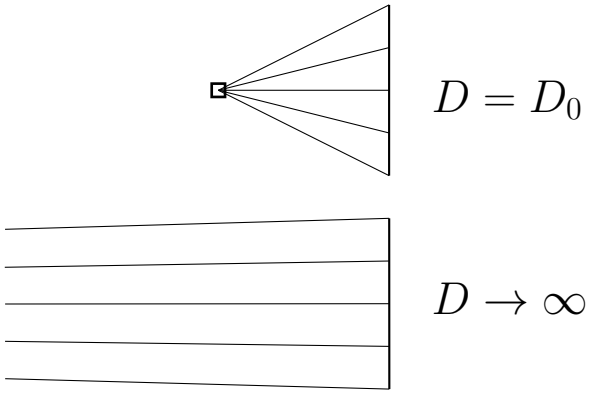

Figure 4.15: Illustration of how the camera's lines-of-sight behave when the camera is moved away from the plasma. Since the lines-of-sight become parallel as $D \to \infty$, the angle between $\hat{\boldsymbol{b}}$ and $\hat{\boldsymbol{r}}$ of Eq. (4.1) in a given point also change, altering the shape of the surface-of-visibility.

the inclination angle of the synchrotron spot β, and the distance to the camera D was found:

$$\tan \beta_{\text{inc}} \approx \frac{D}{q(r) R_m}. \tag{4.5}$$

Aside from a dependence on the proximity D of the camera, the synchrotron spot inclination is also found to depend on the safety factor $q(r)$, which typically varies with minor radius. The inclination of a synchrotron spot at the same "normalized distance" D/R_m from the plasma may therefore vary between different devices, depending on the particular magnetic field configuration of a device.

The second effect observed in Fig. 4.14 is a widening of the synchrotron spot, which appears similar to an increase of the pitch angle. This is quite reasonable, since by moving the camera backwards we also change at what locations in the tokamak the particle will be seen (effectively changing the LHS of the spot equation (4.1)), just as if we would instead have changed the pitch angle of the particle (by changing the RHS of Eq. (4.1)). This is of particular interest, since simple analytical models proposed for determining the pitch angle from the shape of the synchrotron spot (see for example [49] and [50]) should therefore at best be considered valid in the machines for which they were constructed.

4.4 Image due to momentum-space distribution

So far we have considered various forms of radially uniform mono-energetic distributions, or "one-particle" models, but the populations of runaway electrons found in actual tokamaks are widely distributed in phase-space and far from mono-energetic. Because of this, the resulting synchrotron images are rather complex and can contain many details we would not expect to see in one-particle models. While the study of one-particle models, as conducted in the previous sections, is rather straightforward with obvious parameters to vary and with clear results, a similar approach is more difficult to take with distributions of runaway electrons due to the large number of parameters that can be varied. Simple analytical models of the distribution function (see for example [51, 52]) may have only a few parameters to tamper with, but these models on the other hand neglect many effects that are important to runaway dynamics. More advanced models can be applied using numerical tools such as CODE [53, 54] or LUKE [55–57], but introduce many more parameters that make an ordered approach to analyzing the resulting synchrotron images rather difficult. In this section we will give two examples of analytical runaway electron distribution functions and their resulting synchrotron images, just to showcase how such images may look, and the reason for the images taking on the shapes they do in these particular cases.

In the subsequent simulations we will use an analytical runaway electron distribution function valid when avalanching is the dominant runaway generation mechanism, which takes the form [52]

$$f(p_\parallel, p_\perp) = \frac{mcn_r\hat{E}}{2\pi c_Z p_\parallel \ln\Lambda} \exp\left(-\frac{p_\parallel/mc}{c_Z \ln\Lambda} - \frac{p_\perp^2\hat{E}}{2mcp_\parallel}\right). \tag{4.6}$$

Here, n_r is the runaway number density, $c_z = \sqrt{3(Z_{\text{eff}}+5)/\pi}$, Z_{eff} is the effective charge of the plasma, $\ln\Lambda$ is the Coulomb logarithm and $\hat{E} = (E/E_{\text{c}} - 1)/(1 + Z_{\text{eff}})$, where E is the accelerating electric field and E_{c} is the critical electric field which must be overcome for runaway generation to occur. Note that the distribution of particles in energy is very similar in both cases, but that the distribution in pitch angle varies significantly.

Figures 4.19a and 4.20a show two example distributions, generated by setting $\ln\Lambda = 15$ as well as $Z_{\text{eff}} = 1$, $E/E_{\text{c}} = 20$ and $Z_{\text{eff}} = 4$, $E/E_{\text{c}} = 5$ respectively in Eq. (4.6). The first case, with low effective charge and strong electric field, generates a very slim distribution function in which most particles have $p_\parallel \gg p_\perp$. In the second case, the higher Z_{eff} in combination with the weaker electric field, allows particles to gain more perpendicular momentum, giving a wider distribution in the $p_\parallel$-$p_\perp$ plane.

When running SOFT with a distribution of runaway electrons, the region in momentum-space that should be integrated must be specified. To make this region as small as possible, without missing out on any essential contributions to the image, it is vital to know which parts of momentum space that contribute to the image, and this can be done by computing and plotting the quantity $W(\boldsymbol{p})f(\boldsymbol{p})$. The

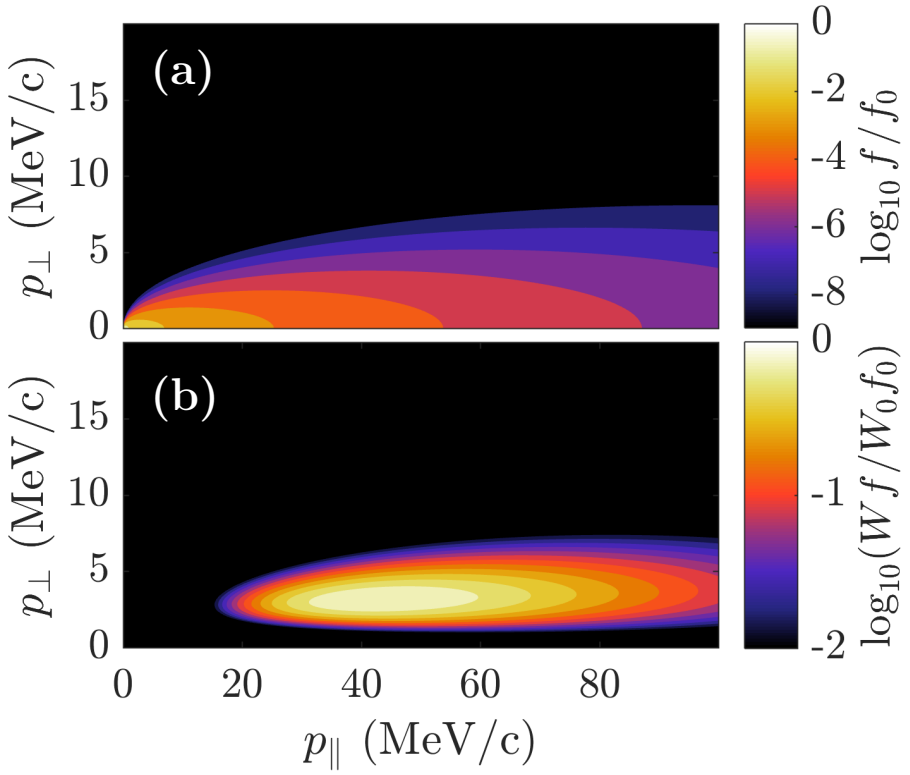

Figure 4.16: The first example distribution, generated with $Z_{\text{eff}} = 1$ and $E/E_{\text{c}} = 20$. Both plots have been normalized to their respective maximum values $f_0 = f(p = 0)$ and $W_0 f_0 = W(p = 0)f(p = 0)$. The strong electric field causes the electrons to almost only gain parallel momentum and produces a rather slim distribution.

function $W(\boldsymbol{p})$ is here the amount of radiation emitted[†] by particles with momentum $\boldsymbol{p}$, and is given by integrating the power-per-wavelength formula (2.57) over all wavelengths visible to the camera under consideration. Figures 4.16b and 4.17b show the result of plotting $W(\boldsymbol{p})f(\boldsymbol{p})$ in the $p_\parallel$-$p_\perp$ plane, and reveals the regions from which contributions within 1% of the maximum are expected. For case 1, the "thin" distribution of Fig. 4.16a, we can pick the region $p_\parallel \in [15, 100]\,\text{MeV/c}$, $p_\perp \in [1, 7]\,\text{MeV/c}$, while for case 2, the "fatter" distribution in Fig. 4.17 we could use $p_\parallel \in [6, 100]\,\text{MeV/c}$, $p_\perp \in [2, 19]\,\text{MeV/c}$.

Before proceeding to the actual simulation, we could try to make predictions about the resulting images based on what was learned in Sec. 4.3.1. In that section the dependence of the synchrotron image on the energy and pitch angle coordinates (among others) was studied, so plotting $W(\boldsymbol{p})f(\boldsymbol{p})$ as a function of p and θ_{p} instead of $p_\parallel$ and $p_\perp$ should help us more readily make predictions. This type of plot is shown in Fig. 4.18. In part (a) of Fig. 4.18 the total emission from distribution function 1 is shown, and it appears to peak around $p = 60\,\text{MeV/c}$, $\theta_{\text{p}} = 0.06\,\text{rad}$. A good guess would be that the synchrotron image resulting from distribution function

[†]To truly show the region of momentum-space contributing to the image we would have to multiply by the sum of the geometric Green's functions $\hat{I}_{ij}$, which are computed by SOFT. For simplicity, we assume that geometric effects will not have a large impact on which parts of momentum-space are in fact visible, and instead use the simpler synchrotron emission formulas.

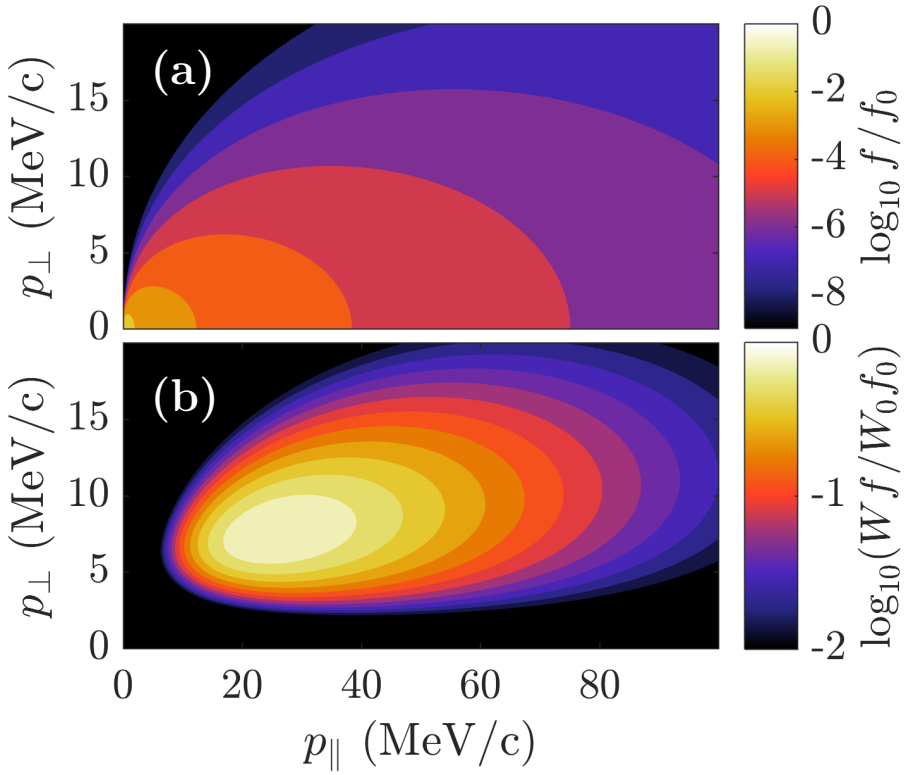

Figure 4.17: The second example distribution, generated with $Z_{\text{eff}} = 4$ and $E/E_c = 5$. Both plots have been normalized to their respective maximum values $f_0 = f(p = 0)$ and $W_0 f_0 = W(p = 0)f(p = 0)$. Compared to the first example distribution, in this case the electrons have gained more perpendicular momentum and are thus more spread out in momentum-space.

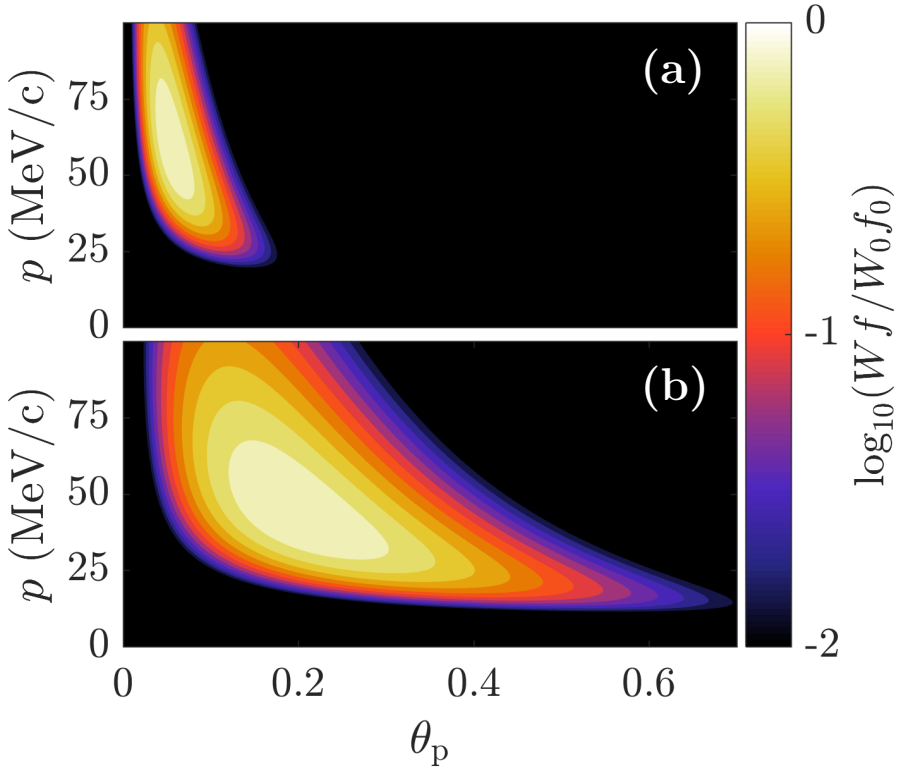

Figure 4.18: The two example distributions, once again weighted with the total synchrotron radiation emitted by particles, but now plotted in the p-θ_p plane to be more easily translated to features in the synchrotron image. Part (a) shows the emission from distribution 1, and part (b) shows the emission from distribution 2.

1 will be dominated by this particle, and thus show many of its characteristics. The synchrotron image should therefore look like something between Fig. 4.8a and 4.8b of Sec. 4.3.2, but appear more "filled" due to particles with slightly smaller and slightly larger pitch angles giving significant contributions. As we saw in Sec. 4.3.3, the dominant energy should not have too much of an effect, but we note that at $p = 60\,\mathrm{MeV/c}$ most of the radiation should be emitted well within the visible band of wavelengths. At these energies particle drifts should also act to significantly distort the synchrotron spot.

For example distribution 2, we see in Fig. 4.18b that the peak of $W(\boldsymbol{p})f(\boldsymbol{p})$ is located near $p = 45\,\mathrm{MeV/c}$ and $\theta_p = 0.20\,\mathrm{rad}$. Drawing from the knowledge gained in Sec. 4.3.1 we expect the resulting synchrotron spot to have a near-circular shape as in Fig. 4.8d. As for example distribution 1, the spectrum corresponding to the peak energy has its maximum well within the visible band of wavelengths and should not affect the spot shape too much. While the energy in this case is much lower than in distribution 1, particle drifts should still have a significant effect and distort the spot.

Figures 4.19 and 4.20 show the synchrotron images resulting from giving the distributions in Figs. 4.16 and 4.17 respectively to SOFT. Both images appear to obtain the shapes predicted by analysing the total emitted power, with the first example distribution giving a tube-shaped synchrotron spot and the second example

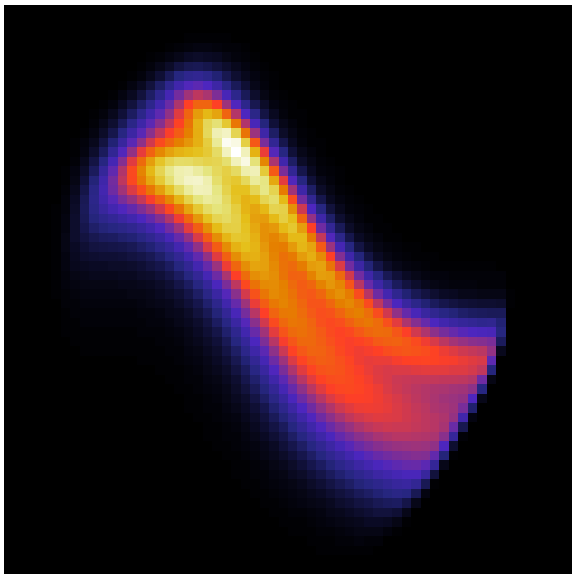

Figure 4.19: Synchrotron image due to the slim distribution of runaway electrons shown in Fig. 4.16. It shows somewhat of the same characteristics as a mono-energetic distribution of runaways with $\theta_{\mathrm{p}} = 0.06\,\mathrm{rad}$.

distribution giving a more circular spot shape. In both cases the synchrotron spots appear more "filled" than the mono-energetic distributions considered in Sec. 4.3.1, which generally only gave strong contributions along the edges of the synchrotron spot. A second peculiar feature observed in Figs. 4.19 and 4.20 is that the synchrotron spot seems to contain two slightly brighter parts, with a thin dark line separating them.

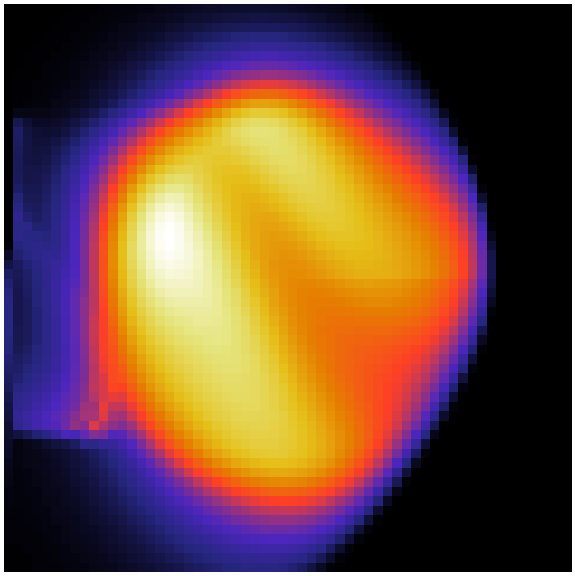

Figure 4.20: Synchrotron image due to the thick distribution of runaway electrons shown in Fig. 4.17. It shows somewhat of the same characteristics as a mono-energetic distribution of runaways with $\theta_{\mathrm{p}} = 0.20\,\mathrm{rad}$.

5
Conclusions

Solving the problem of runaway electrons is crucial for the success of future magnetic fusion devices, as the strong currents carried by them can cause severe damage to the device when control of the runaway beam is lost. Sophisticated theoretical models of runaway electron dynamics and interactions exist, but the complex sequence of events taking place in a fusion plasma makes diagnosing the runaway electrons and comparing experiment to theory quite difficult. While synchrotron radiation is a powerful tool for diagnosing runaway electrons, the analysis is complicated by many factors, such as the fact that real-world magnetic fields are inhomogeneous and that runaway electron populations are far from homogeneous in momentum-space, necessitating a coupling of the theory of synchrotron radiation with kinetic theory for runaway electrons. To properly account for these complications it is therefore necessary to use a synthetic synchrotron diagnostic code that simulates the actual camera used in experiment.

The motion of a charged particle in a tokamak (or any magnetic field for that matter) is determined by the Lorentz force acting on it, causing the particle to follow a helical path approximately around magnetic field lines. By considering the motion of the particle as a superposition of circular motion perpendicular to the magnetic field, and motion approximately parallel to it, one can introduce the concept of a guiding-center from which the circular gyro-motion perpendicular to the field is decoupled. This way of viewing the particle's motion is numerically much cheaper than following the full particle orbit, since in the guiding-center picture the rapid gyro-motion does not have to be resolved. Generally, in a synthetic synchrotron diagnostic one would need to study the particle motion, since it is particles that emit synchrotron radiation. It is however possible to reformulate the theory in terms of the particle's guiding-center, by making an average of the quantity of interest over one gyro-period. This is done for SOFT, and allows the guiding-center orbit to be traced, rather than the numerically more expensive particle orbit.

During a tokamak disruption event, the conductivity decreases as the temperature drops, inducing a strong electric field. If the electric field is strong enough, it can accelerate a significant fraction of the electron population to highly relativistic energies, generating so called "runaway electrons" due to the inability of the plasma to keep the electrons from reaching very high energies. There is however an upper limit to the energy that a runaway electron can attain, arising due to significant energy loss through emission of electromagnetic radiation and through losses of particles to the wall, due to the electrons' large drift orbits.

The radiation emitted by relativistic runaway electrons due to their rapid gyro-motion around magnetic field lines show characteristic angular and spectral depen-

dences, and is referred to as *synchrotron radiation*. As was shown in Section 2.3, the synchrotron radiation emitted by a runaway electron is confined to a narrow beam of opening angle γ^{-1} directed along the electron's velocity vector, where γ is the relativistic Lorentz factor of the electron. This fact, in combination with the shape of the runaway electron's path through the magnetic field, causes the observed radiation spot to take on very peculiar and counter-intuitive shapes.

Some understanding for why the synchrotron spot has a particular shape can be gained by introducing the simplified model known as the *cone model*. In this model the runaway electron energy is assumed large so that all synchrotron radiation is emitted essentially in a line along the particle's velocity vector. In the guiding-center picture, this corresponds to the guiding-center emitting radiation along a conical surface with opening angle equal to the pitch angle of the particle, around the guiding-center velocity vector. The guiding-center will in turn approximately follow magnetic field lines, so the condition for a particle to contribute to the camera image is that the angle between the magnetic field and the vector between the camera and guiding-center is equal to the pitch angle.

The synchrotron spot was shown to depend not just on the properties of the runaway electron population, but also on the placement of the synchrotron camera. This is due to the fact that a particular line-of-sight must make an angle equal to the particle pitch angle with the magnetic field, in the point where the guiding-center is located, for the particle to be seen. One of the more interesting results this has is that particles with small pitch angles, moving near the magnetic axis, will be invisible to the camera if the camera is placed too far from the midplane. While it may seem from this as though all synchrotron cameras should be placed in the midplane, it may actually be a good idea to distribute cameras both in, below and above the midplane, since this could put further constraints on the possible shape of the distribution function, which would be the unknown that must be determined.

A population of runaway electrons are predicted by kinetic theory to possess many different energies and pitch angles, and as such the synchrotron spot produced by them, and observed by a synchrotron camera, can be quite complex. The image is however linear in the sense that it can be considered a weighted superposition of images resulting from various mono-energetic and mono-pitch populations of runaways, with the distribution of runaways with a given energy and pitch angle acting as the weight function. This permits study of the effect of mono-energetic and mono-pitch distributions on the synchrotron spot, and conclusions from these studies to be applied to more complex cases involving runaways that are continuously distributed in momentum-space.

One complication arising when trying to draw conclusions about the runaway population by looking at the synchrotron image they give rise to, is that the brightness of each of the constituent images from mono-energy/mono-pitch populations depends on the energy and pitch angle of the specific population under consideration. This has the result that particles with a certain energy and pitch angle may appear to dominate the image, but in the distribution of runaways they only make up a tiny fraction of the total. While mono-energetic and mono-pitch images to some extent can match observed synchrotron images, they should not be taken as literal descriptions of the runaway distribution function. In short, the runaway dis-

tribution function of a realistic runaway population does not consist of only one energy and one pitch angle.

The great versatility of SOFT makes it possible to apply it to model experimental scenarios and Section 4.4 gives an example of how this can be done through forward modelling. Two different analytical avalanche distribution functions were considered and shown to give significantly different synchrotron images, showcasing how it should be possible to estimate runaway population parameters from the synchrotron image. To model actual experiments it will however be necessary to consider more effects than those accounted for by the analytical avalanche model used in this thesis, since for example synchrotron and bremsstrahlung losses are expected to limit the attainable energy of the runaways, which are not accounted for in the analytical model. This can be done with the use of a numerical kinetic-equation solver such as CODE [53, 54] or LUKE [55–57], which allow for experimental parameters such as density, temperature and electric field to be given as input. The forward modelling approach would also allow verification of kinetic theory for runaway electrons in a very direct way.

Coupling SOFT with a numerical kinetic-equation solver to test whether any observed synchrotron images can be reproduced from measured quantities (that are of importance to runaway generation), is a relatively computationally cheap and useful way to model experiments. However, it would be of great benefit if the inverse problem could be solved through backward modelling. In backward modelling, the distribution function is considered as the unknown quantity and the goal is to reproduce it from the observed synchrotron data. If this can be carried out it will allow the distribution function to be measured indirectly in experiments, something which would give much insight into what is going on with the runaway electrons and how they evolve in time. The inverse problem is likely ill-conditioned however, making uncertainties in the fitting large, and making it impossible to solve through the inversion of a matrix. Instead, an optimization approach might be taken, where the global optimum of a fitness function determining the agreement between simulation and experiment is sought, which is common when optimizing complicated functions [58]. While this approach would require significant computational power, it should be able to converge to a candidate distribution function.

In many experimental studies of runaways, the synchrotron spectrum has been measured and gives interesting insight into the emitted radiation. In difference to synchrotron images, synchrotron spectra can be highly sensitive to the energy of the runaway population and therefore put additional constraints on the unknown distribution function. Synchrotron images and spectra should thus be seen as complements to each other that provide different kinds of information, and ultimately reveal different aspects of the same runaway population. Currently, while SOFT is able to produce synchrotron spectra, their behaviour is much less investigated than the behaviour of synchrotron images. There are reasons to believe though, that a SOFT simulation of the spectrum could be quite valuable and differ significantly from previous studies of the synchrotron spectrum of runaway electrons [37] due to the fact that the magnetic geometry and relative camera position are taken into account. Since the magnetic field strength changes over the course of a particle orbit, which also causes the pitch angle to change (increases with increasing magnetic

field), the synchrotron spectrum obtained from a distribution of runaway electrons specified in the outer midplane will be a poloidal average of the radiation reaching the spectrometer. A spectrum calculated with SOFT should therefore differ from a spectrum calculated directly from the synchrotron emission formulas, as done in previous studies [37], since the evolution of the distribution function due to the magnetic field geometry is then not considered. Thus, in order to take geometric effects of the magnetic equilibrium on the spectrum into account, a tool such as SOFT must be used.

Bibliography

[1] IPCC. *Climate change 2013: the physical science basis: Working Group I contribution to the Fifth assessment report of the Intergovernmental Panel on Climate Change*. Cambridge University Press, 2014.

[2] M. I. Hoffert et al. "Advanced technology paths to global climate stability: energy for a greenhouse planet". In: *Science* 298.5595 (2002), pp. 981–987.

[3] D. J. Ward et al. "The economic viability of fusion power". In: *Fusion engineering and design* 75 (2005), pp. 1221–1227.

[4] J. P. Freidberg. *Plasma physics and fusion energy*. Cambridge: Cambridge University Press, 2007. ISBN: 978-052-173317-5.

[5] M. Kikuchi, K. Lackner, and M. Q. Tran. *Fusion physics*. Tech. rep. IAEA, 2012.

[6] R. J Goldston and P. H. Rutherford. *Introduction to plasma physics*. CRC Press, 1995.

[7] J. Milnor. "Analytic proofs of the" hairy ball theorem" and the Brouwer fixed point theorem". In: *The American Mathematical Monthly* 85.7 (1978), pp. 521–524.

[8] J. Wesson and D. J. Campbell. *Tokamaks*. 3rd ed. Vol. 118. Oxford: Clarendon Press, 2004. ISBN: 9780198509226.

[9] P.C. de Vries et al. "Survey of disruption causes at JET". In: *Nuclear Fusion* 51.5 (2011), p. 053018.

[10] H. Dreicer. "Electron and ion runaway in a fully ionized gas I". In: *Physical Review* 115.2 (1959), p. 238.

[11] H. Dreicer. "Electron and ion runaway in a fully ionized gas. II". In: *Physical review* 117.2 (1960), p. 329.

[12] H. P. Furth and P. H. Rutherford. "Ion runaway in tokamak discharges". In: *Physical Review Letters* 28.9 (1972), p. 545.

[13] P. Helander and D. J. Ward. "Positron creation and annihilation in tokamak plasmas with runaway electrons". In: *Physical review letters* 90.13 (2003), p. 135004.

[14] T. Fülöp and G. Papp. "Runaway positrons in fusion plasmas". In: *Physical review letters* 108.22 (2012), p. 225003.

[15] O. Embréus et al. “Numerical calculation of ion runaway distributions”. In: *Physics of Plasmas* 22.5 (2015), p. 052122.

[16] ITER Physics basis. In: *Nuclear Fusion* 39.12 (1999), p. 2137.

[17] ITER organization. URL: `http://www.iter.org/`.

[18] M. N. Rosenbluth and S. V. Putvinski. “Theory for avalanche of runaway electrons in tokamaks”. In: *Nuclear Fusion* 37.10 (1997), pp. 1355–1362.

[19] K. H. Finken et al. “Observation of infrared synchrotron radiation from tokamak runaway electrons in TEXTOR”. In: *Nuclear Fusion* 30.5 (1990), pp. 859–870.

[20] L. D. Landau and E. M. Lifshitz. *The Classical Theory of Fields*. Fourth Revised English Edition. Vol. 2. Course of Theoretical Physics. Butterworth Heinemann, 1980. ISBN: 978-0-7506-2768-9.

[21] J. D. Jackson. *Classical Electrodynamics*. 3rd ed. John Wiley & Sons, Inc., 1999. ISBN: 978-047-130932-1.

[22] O. Embréus, A. Stahl, and T. Fülöp. “Effect of bremsstrahlung radiation emission on fast electrons in plasmas”. In: *New Journal of Physics* 18.9 (2016), p. 093023.

[23] H. Bethe and W. Heitler. “On the stopping of fast particles and on the creation of positive electrons”. In: *Proceedings of the Royal Society of London A: Mathematical, Physical and Engineering Sciences*. Vol. 146. 856. The Royal Society. 1934, pp. 83–112.

[24] D. K. Cheng. *Field and Wave Electromagnetics*. Pearson New International Edition. Pearson Higher Ed, 2014.

[25] T. G. Northrop. “The guiding center approximation to charged particle motion”. In: *Annals of Physics* 15.1 (1961), pp. 79–101.

[26] X. Tao, A. A. Chan, and A. J. Brizard. “Hamiltonian theory of adiabatic motion of relativistic charged particles”. In: *Physics of Plasmas* 14.9 (2007), p. 092107.

[27] M. Greenwald et al. “Overview of the Alcator C-Mod program”. In: *Nuclear fusion* 45.10 (2005), S109.

[28] P. Helander and D. J. Sigmar. *Collisional Transport in Magnetized Plasmas*. Vol. 4. Cambridge: Cambridge Univ. Press, 2002. ISBN: 978-052-180798-2.

[29] A. Stahl. “Synchrotron radiation from runaway electrons in plasmas”. Licentiate thesis. Göteborg, Sweden: Department of Applied Physics, Chalmers University of Technology, 2015.

[30] F. Andersson, P. Helander, and L.-G. Eriksson. “Damping of relativistic electron beams by synchrotron radiation”. English. In: *Physics of Plasmas* 8.12 (2001), pp. 5221–5229. DOI: `0.1063/1.1418242`.

[31] E. Hirvijoki et al. “Guiding-center transformation of the Abraham-Lorentz-Dirac radiation reaction force”. In: *arXiv preprint arXiv:1412.1966* (2014).

[32] G. R. Blumenthal and R. J. Gould. “Bremsstrahlung, Synchrotron Radiation, and Compton Scattering of High-Energy Electrons Traversing Dilute Gases”. In: *Reviews of Modern Physics* 42.2 (1970), pp. 237–270.

[33] V. L. Ginzburg, V. N. Sazonov, and S. I. Syrovatskii. “Synchrotron radiation and its reabsorption”. In: *Soviet Physics Uspekhi* 11.1 (1968), p. 34.

[34] J. Schwinger. “On the Classical Radiation of Accelerated Electrons”. In: *Physical Review* 75.12 (1949), pp. 1912–1925.

[35] R. A. Tinguely et al. “Analysis of Runaway Electron Synchrotron Radiation in Alcator C-Mod”. In: *Bulletin of the American Physical Society*. Vol. 60. American Physical Society, 2015.

[36] G. Bekefi. *Radiation processes in plasmas*. English. New York, 1966. ISBN: 978-990-063710-3.

[37] A. Stahl et al. “Synchrotron radiation from a runaway electron distribution in tokamaks”. In: *Physics of Plasmas* 20.9 (2013), p. 093302.

[38] R. J. Zhou et al. “Investigation of ring-like runaway electron beams in the EAST tokamak”. In: *Plasma Physics and Controlled Fusion* 55.5 (2013), p. 055006.

[39] I. M. Pankratov. “Analysis of the synchrotron radiation spectra of runaway electrons”. In: *Plasma Physics Reports* 25.145 (1999).

[40] M. Hoppe. *SOFT GitHub repository*. URL: `https://github.com/hoppe93/SOFT`.

[41] L. D. Landau and E. M. Lifshitz. *Mechanics*. Third Edition. Vol. 1. Course of Theoretical Physics. Butterworth Heinemann, 1976. ISBN: 978-0-7506-2896-9.

[42] A. H. Boozer. “Guiding center drift equations”. In: *The Physics of Fluids* 23.5 (1980), pp. 904–908.

[43] W. H. Press et al. *Numerical recipes*. Third edition. Cambridge University Press, 2007.

[44] A. S. Ackleh et al. *Classical and modern numerical analysis: Theory, methods and practice*. CRC Press, 2009.

[45] T. E. Stringer. “Effect of the magnetic field ripple on diffusion in tokamaks”. In: *Nuclear Fusion* 12.6 (1972), p. 689.

[46] E. M. Hollmann et al. “Control and dissipation of runaway electron beams created during rapid shutdown experiments in DIII-D”. In: *Nuclear Fusion* 53.8 (2013), p. 083004.

[47] R. J. Zhou et al. “Synchrotron radiation spectra and synchrotron radiation spot shape of runaway electrons in Experimental Advanced Superconducting Tokamak”. In: *Physics of Plasmas* 21 (6 2014).

[48] G. Papp et al. “Runaway electron drift orbits in magnetostatic perturbed fields”. In: *Nuclear Fusion* 51.4 (2011), p. 043004.

[49] R. Jaspers et al. “A synchrotron radiation diagnostic to observe relativistic runaway electrons in a tokamak plasma”. In: *Review of Scientific Instruments* 72.1 (2001), pp. 466–470.

[50] J. H. Yu et al. “Visible imaging and spectroscopy of disruption runaway electrons in DIII-D”. In: *Physics of Plasmas* 20.4 (2013), p. 042113.

[51] J. W. Connor and R. J. Hastie. “Relativistic limitations on runaway electrons”. In: *Nuclear fusion* 15.3 (1975), p. 415.

[52] T. Fülöp et al. “Destabilization of magnetosonic-whistler waves by a relativistic runaway beam”. In: *Physics of Plasmas* 13.6 (2006), p. 062506.

[53] M. Landreman, A. Stahl, and T. Fülöp. “Numerical calculation of the runaway electron distribution function and associated synchrotron emission”. In: *Computer Physics Communications* 185 (3 2014), pp. 847–855. ISSN: 0010-4655. DOI: http://dx.doi.org/10.1016/j.cpc.2013.12.004.

[54] A. Stahl et al. “Kinetic modelling of runaway electrons in dynamic scenarios”. In: *Nuclear Fusion* 56.11 (2016), p. 112009.

[55] Y. Peysson et al. “Advanced 3-D Electron Fokker-Planck Transport Calculations”. In: *AIP Conference Proceedings*. Vol. 694. 1. AIP. 2003, pp. 495–498.

[56] J. Decker and Y. Peysson. *DKE: a fast numerical solver for the 3D drift kinetic equation Euratom-CEA Report*. Tech. rep. No EUR-CEA-FC-1736, 2004.

[57] E. Nilsson et al. “Kinetic modelling of runaway electron avalanches in tokamak plasmas”. In: *Plasma Physics and Controlled Fusion* 57.9 (2015), p. 095006.

[58] M. Wahde. *Biologically inspired optimization methods: an introduction*. WIT press, 2008.